Computational Study of Hub Corner Stall in an Axial Compressor Rotor

by John A. Gailliot

Thesis submitted to the Faculty of the
Virginia Polytechnic Institute and State University
in partial fulfillment of the requirements for the degree of
MASTERS OF SCIENCE
IN
MECHANICAL ENGINEERING

APPROVED:

John Moore
J. Moore, Chairman

Clint Dancey
C. L. Dancey

W. F. Ng

August 1995

Blacksburg, Virginia

Key words: CFD, Compressor, Rotor, Corner Stall, Streaklines

Computational Study of Hub Corner Stall in an Axial Compressor Rotor

by John A. Gailliot
J. Moore, Chairman
Mechanical Engineering

(ABSTRACT)

The Deverson rotor, a single stage axial compressor designed to simulate a multistage axial compressor, was studied computationally using a 3-D Navier-Stokes solver, the Moore Elliptic Flow Program. A one equation, q-L, transitional turbulence model was used with MEFP for closure of the transport equations. The calculation was used to study the physics and flow mechanisms affecting hub corner stall. Preprocessing and postprocessing programs were written to aid this study, a grid generation program and a streakline visualization program, respectively.

First, computational 2-D cascade studies were performed to study the effects of free stream turbulence level and incidence angle on suction surface boundary layer development. The results showed the correct trends in boundary layer transition and separation, loss production, and deviation angles.

Velocity measurements taken at the exit of the Deverson rotor were made available by Rolls-Royce for comparison with the 3-D calculation results. The q-L turbulence model predicted the existence of the hub corner stall, but under predicted the size of the corner stall. It failed to predict the radial migration of the associated loss core. However, the calculation did reveal details of the flow that affect corner stall. These included boundary layer transition and separation on the suction surface, hub and suction surface secondary flows, and radial relief. Streaklines were useful in visualizing and understanding these flow details.

A preliminary 3-D calculation was performed with a two-equation, q-ω, turbulence model. This turbulence model more accurately predicted the corner stall including radial migration of the loss core.

Acknowledgments

I would like to extend my appreciation to Dr. John Moore for his guidance and support for this work. My appreciation is also extended to Mrs. Joan Moore for her help in all stages of this work.

The support of this work, from Rolls-Royce plc., under a cooperative agreement with Virginia Tech, and the Mechanical Engineering Department of Virginia Tech, is gratefully acknowledged.

I would like to thank my parents for the support given over the years that has allowed me to reach this point.

Special thanks is due to my wife, Angel, and my daughter, Taylor. With their patience, understanding, and encouragement, all things are possible.

Table of Contents

List of Figures

List of Tables

Nomenclature

A	1-D parameter, $\simeq z / c_{ax}$
c	Rotor Chord
c_{ax}	Blade Axial Chord
c_D	Section Drag Coefficient
C	Fraction of Blade Height
Cp_t	Total Pressure Loss Coefficient
D_ω	Dissipation Rate of ω
D_q	Dissipation Rate of q
F_{tu}	Intermittency Function (q-L Turbulence Model)
i, j, k	Grid Indices
L	Prandtl Mixing Length
m	Pressure Gradient Parameter (Thwaites Method)
P_q	Production Rate of q
p	Static Pressure
P	Normalized Static Pressure, Eq. 6.19
p*	Rotory Stagnation Pressure
P*	Normalized Rotory Stagnation Pressure Loss, Eq. 7.3
q	Square Root of Turbulence Kinetic Energy
Q	Normalized Square Root of Turbulence Kinetic Energy
r, θ, z	Cylindrical Coordinates
Re	Reynolds Number
Re_θ	Reynolds Number based on Momentum Thickness
R_{tu}	Reynolds Number of Turbulence
Tu	Turbulence Intensity

u, v, w	Fluctuating Components of Velocity
U	Blade Velocity
V	Absolute Velocity
W	Relative Velocity
x, y, z	Cartesian Coordinates
β_1	Inlet Flow Angle
β_2	Exit Flow Angle
δ	Deviation Angle
δ_1	Boundary Layer Displacement Thickness
μ_l	Laminar Viscosity
μ_t	Turbulent Viscosity
μ_{eff}	Effective Viscosity
ν	Kinematic Viscosity
ρ	Density
ω	Specific Dissipation Rate of Turbulence Kinetic Energy
Ω_s	Streamwise Component of Vorticity
Ω	Blade Angular Velocity
θ	Momentum Thickness or Flow Turning Angle

Subscripts

$_{fre}$	Free Stream
$_t$	Total
$_0$	Inlet Total
$_i$	Inlet

1.0 Introduction

As the development costs of jet engines increases each year, it is becoming increasingly important to understand the complex three-dimensional flows in them. Multistage axial compressors are an important part of these engines. They can experience high losses from the interaction of blade and endwall secondary flows. The development of these three-dimensional flows in the suction surface/hub corner area can lead to hub corner stall and high losses.

The designers of axial flow compressors are increasingly using Computational Fluid Dynamics software as a design tool. CFD codes aim to predict three-dimensional viscous flows through compressors accurately. These codes allow the designer to study the three-dimensional flows that will exist with a given geometry before it is actually built. This insight allows the redesign of compressor blading to reduce losses and maximize the efficiency.

Phenomena governing compressor performance are reviewed in the literature review and include: boundary layer transition and separation, surface secondary flows, hub corner stall, and radial relief of leading edge loading on compressor blading.

MEFP, the Moore Elliptic Flow Program, is a Computational Fluid Dynamics program written to predict flows through turbomachines. In this thesis it is used for two and three-dimensional compressor flow studies. The flows were predicted using a one-equation q-L transitional turbulence model.

To do these studies, a grid generation program was developed which would create a calculation grid that satisfied the requirements of the q-L turbulence model including uniform near-wall spacing.

2-D cascade studies were performed that examined the flow on the suction surface of the rotor blade to study aspects of boundary layer development. These studies were on the effects of free stream turbulence intensity and incidence angle on boundary layer transition and separation.

A three-dimensional calculation was made to simulate the flow through the rotor of the Deverson compressor, a single stage axial flow compressor designed to simulate a multistage compressor. Calculation results were compared with experimental data from the exit of the compressor's rotor provided by Rolls-Royce. The calculation was used to gain a physical understanding of the factors involved in the development of hub corner stall in multistage axial flow compressors. The accuracy of the q-L turbulence model in predicting hub corner stall was also assessed.

Flow visualization of results is important for analyzing the flow and comparing it with actual flows. A particularly potent visualization tool is streakline analysis; it gives an understanding of specific and global flow phenomena. A streakline visualization program was developed to aid in understanding the predicted two and three-dimensional flow details.

An additional calculation was run for the Deverson rotor using a q-ω turbulence model currently being developed. The results of this calculation were then compared with the results from the q-L turbulence model and the experimental data.

2.0 Literature Review

Over the past several decades in multi-stage axial flow compressor design, there has been a steady trend to increase the speed, the pressure rise per stage, and to decrease the aspect ratio. These trends tend to increase the importance of end wall boundary layers and the high loss/separated flow regions associated with them as shown in Figure 2.1.

Howard et al. (1993) has estimated that three-dimensional endwall effects leave only 25% of the flow unaffected and account for half of all stage losses in the third stage of a four stage compressor. Of particular interest in the present study is the separated flow in the suction surface/hub corner region. This phenomenon is generally referred to as corner stall. There are many factors that influence the flow to separate and generate the high losses associated with it.

2.1 Factors Effecting Flow Separation and Loss Production

2.1.1 Incidence

At the design flow coefficient, ϕ, when the flow enters the blade row at the design incidence, $i = \beta_1 - \beta_1'$ as illustrated in Figure 2.2, the size of the separated region is typically small or does not exist. But as the flow rate is reduced, the incidence increases, and the hub corner stall appears or increases in size. The hub region of the rotor blade experiences high incidence angles due to the boundary layer skew depicted in Figure 2.3. (Dong et al., 1986, Lakshminarayana et al., 1985) With a change to the relative frame of reference as the boundary layer fluid passes into the rotating region of the hub, the fluid gains a significant circumferential velocity component resulting in the high incidence angle.

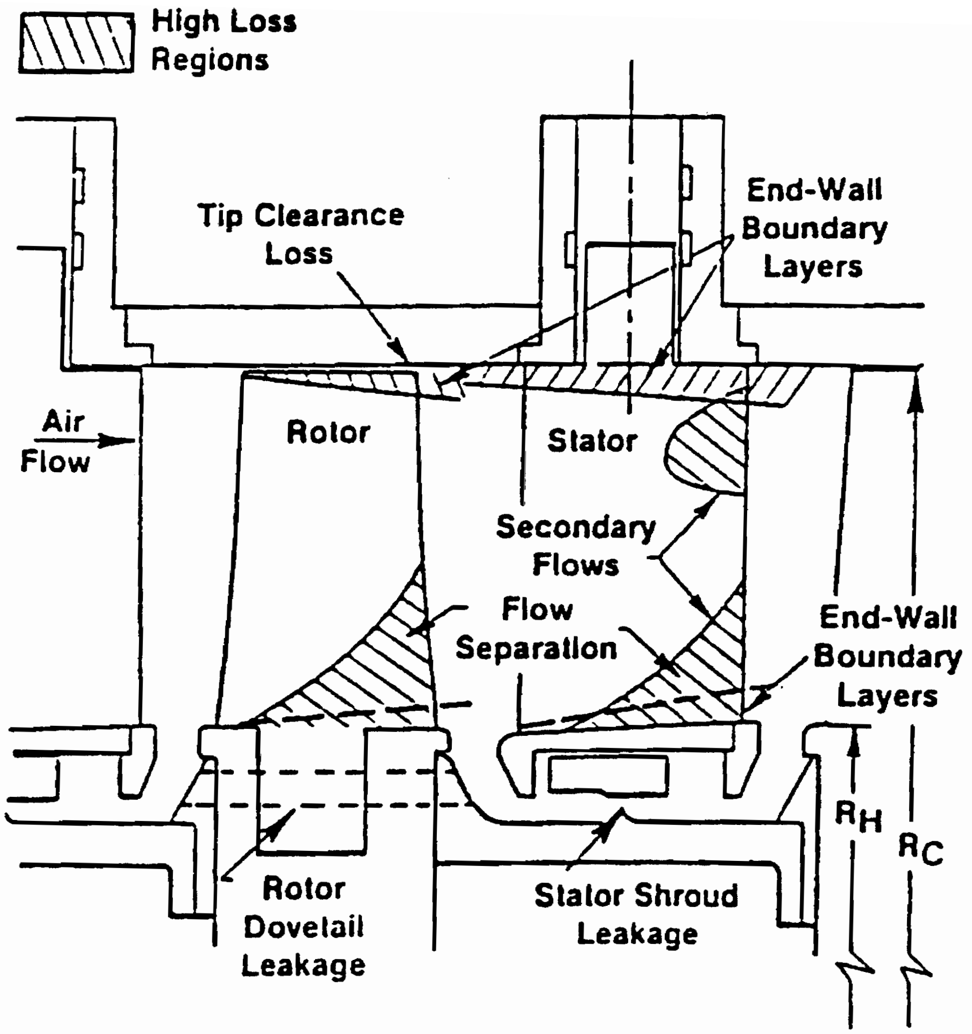

Figure 2.1 High-Loss Regions in Multi-Stage Core Compressors (Wisler, 1987)

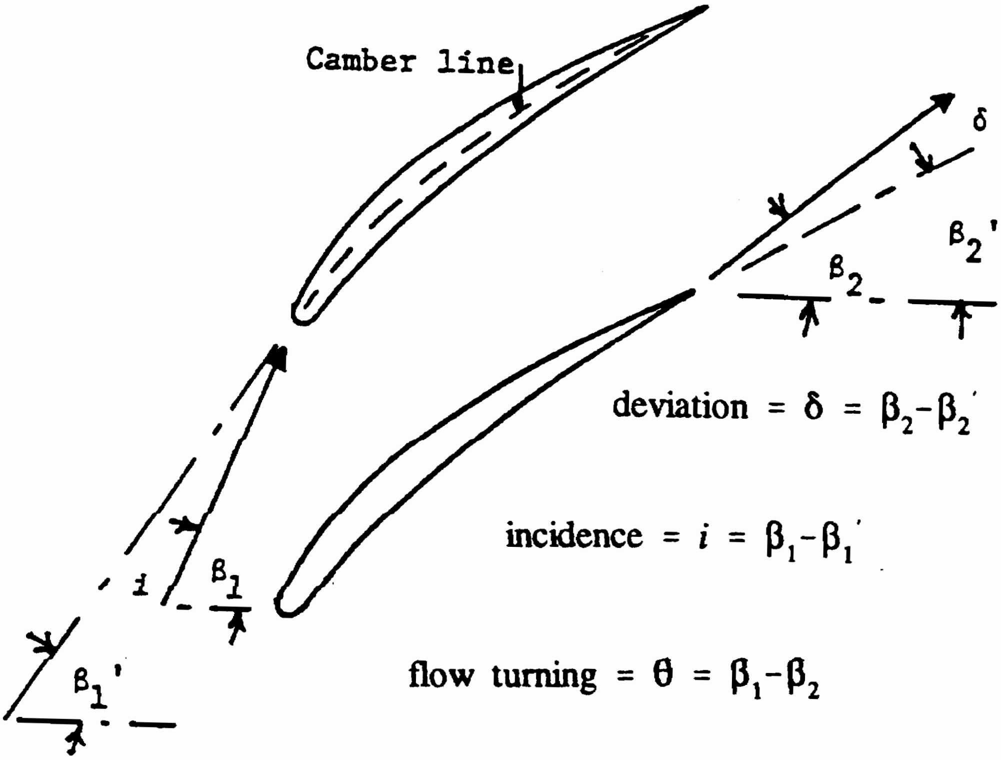

deviation = $\delta = \beta_2 - \beta_2'$

incidence = $i = \beta_1 - \beta_1'$

flow turning = $\theta = \beta_1 - \beta_2$

Figure 2.2 Illustration of Deviation, Incidence, and Flow Turning Angles

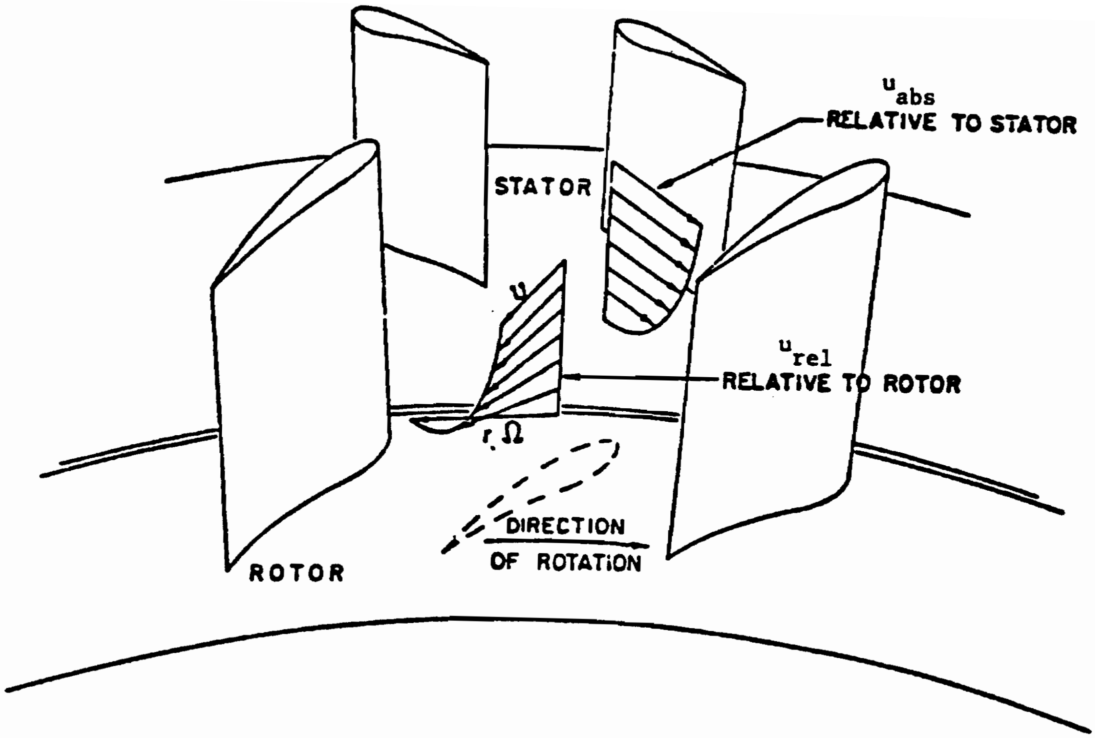

Figure 2.3 Skew at the Inlet to a Rotor (Moore, 1957)

2.1.1.1 Radial Relief

Two-dimensional cascade analyses on blade sections near the end walls show that the high incidence angles cause high leading edge loadings that decrease overall performance. However, experimental data suggests that in three-dimensional flows, the leading edge loading is not as high as the two-dimensional analyses suggest. The reason for the difference between the two is generally accepted to be from secondary flow effects. In particular, these three-dimensional effects can be attributed to radial adjustment of the flow distribution along the leading edge. The mechanism generating the secondary flows along the leading edge is a static pressure gradient.

For the case of a stator, which was studied by Wadia and Beacher (1989), the high incidence angles from the casing inlet skew cause a minimum static pressure near the suction surface in the stator/casing region. The associated radial static pressure gradient causes radial outward flows along the suction surface which then rapidly decelerate as they approach the casing/stator corner thereby increasing the pressure. A similar argument can be made for the hub/suction surface corner at the leading edge. The difference being that the static pressure gradient now causes a radially inward flow along the leading edge.

2.1.2 Secondary Flows

2.1.2.1 Horseshoe Vortex

As the flow approaches the leading edge of the rotor, the interaction of the hub boundary layer with the leading edge produces a horseshoe vortex. Figure 2.4 shows a simplified mechanism for the production of a horseshoe vortex. The vorticity present within the boundary layer due to the positive radial velocity gradient, $\partial u/\partial r$, is convected around the leading edge forming a suction side leg and a pressure side leg (Moore, 1994). The suction side leg tends to migrate up the blade surface above the corner stall as it progresses downstream and then dissipates or mixes out. The pressure side leg is usually pulled toward the suction surface of the next blade by the secondary flows that develop along the hub from the pressure surface to the suction surface and may then be caught up in the corner stall.

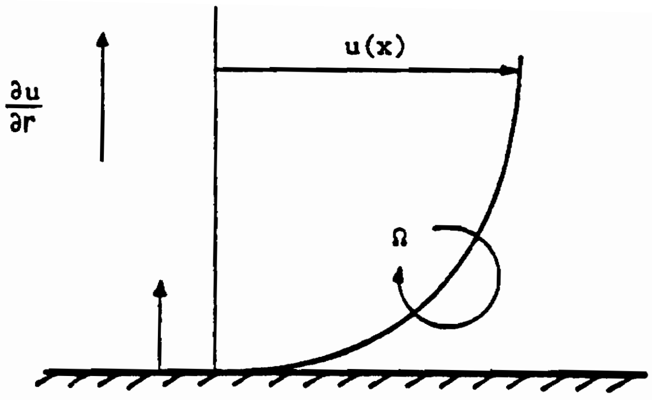

Vorticity Within Boundary Layer

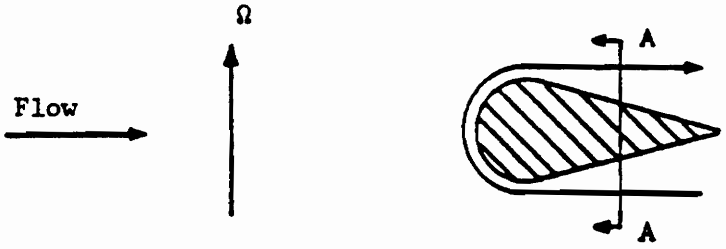

Convection of Vortex Line

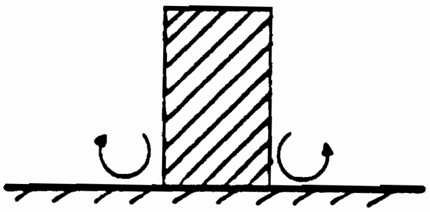

Cross Section AA: Streamwise Vorticity

Figure 2.4 Mechanism for the Formation of a Horseshoe Vortex (Moore, 1994)

2.1.2.2 Hub Secondary Flow

Several experimental studies show the development of secondary flow along the hub from the pressure side to the suction side and interacting with the separated flow region (Cyrus, 1986, Lakshminaranayana et al, 1985). Figure 2.5 depicts this secondary flow and corner stall. The secondary flow causes the high loss fluid from the boundary layer to accumulate in the suction surface/hub corner region, adding to the losses generated by the separated flow or even inducing the corner stall.

A simplified explanation for the development of the hub secondary flow can be based upon an equation from Hawthorne (1974) for the generation of a streamwise component of vorticity, Ω_S, in steady, inviscid, and incompressible flow.

$$\frac{\partial}{\partial s}\left(\frac{\Omega_s}{W}\right) = \frac{2}{\rho W^2}\left(\frac{1}{R_n}\frac{\partial p^*}{\partial b} + \frac{\omega}{W}\frac{\partial p^*}{\partial z}\right) \qquad \textbf{(Eq. 1.1)}$$

The first term with the principal radius of curvature of the relative streamline, R_n, and the gradient of rotary stagnation pressure, p^*, is what generates the hub secondary flow. Having both streamline curvature and a radial gradient of rotary stagnation pressure is necessary to develop a strong enough secondary flow to overcome the inlet skew. A simplified view of how a negative component of vorticity is generated in the outer part of the hub boundary layer can be seen in View AA in Figure 2.6. The negative gradient of rotary stagnation pressure in the binormal direction multiplied by a positive rotation yields a negative vorticity which creates the secondary flows from the pressure surface to the suction surface.

Another source of high loss fluid in the separated region is the pressure surface boundary layer (Hirsch and Kang, 1993). Because there is reversed flow in the separated region, some fluid is convected around the trailing edge and entrained in the backflow.

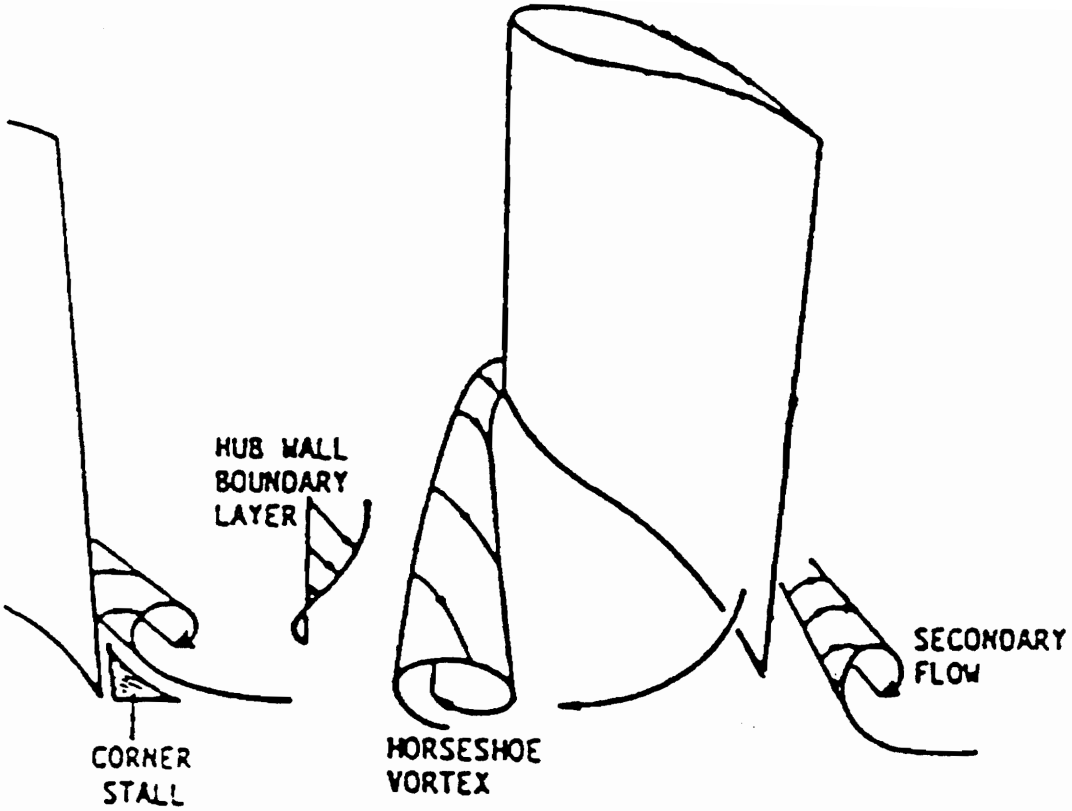

Figure 2.5 Secondary Flow Patterns, after Hirsch and Kang (1993)

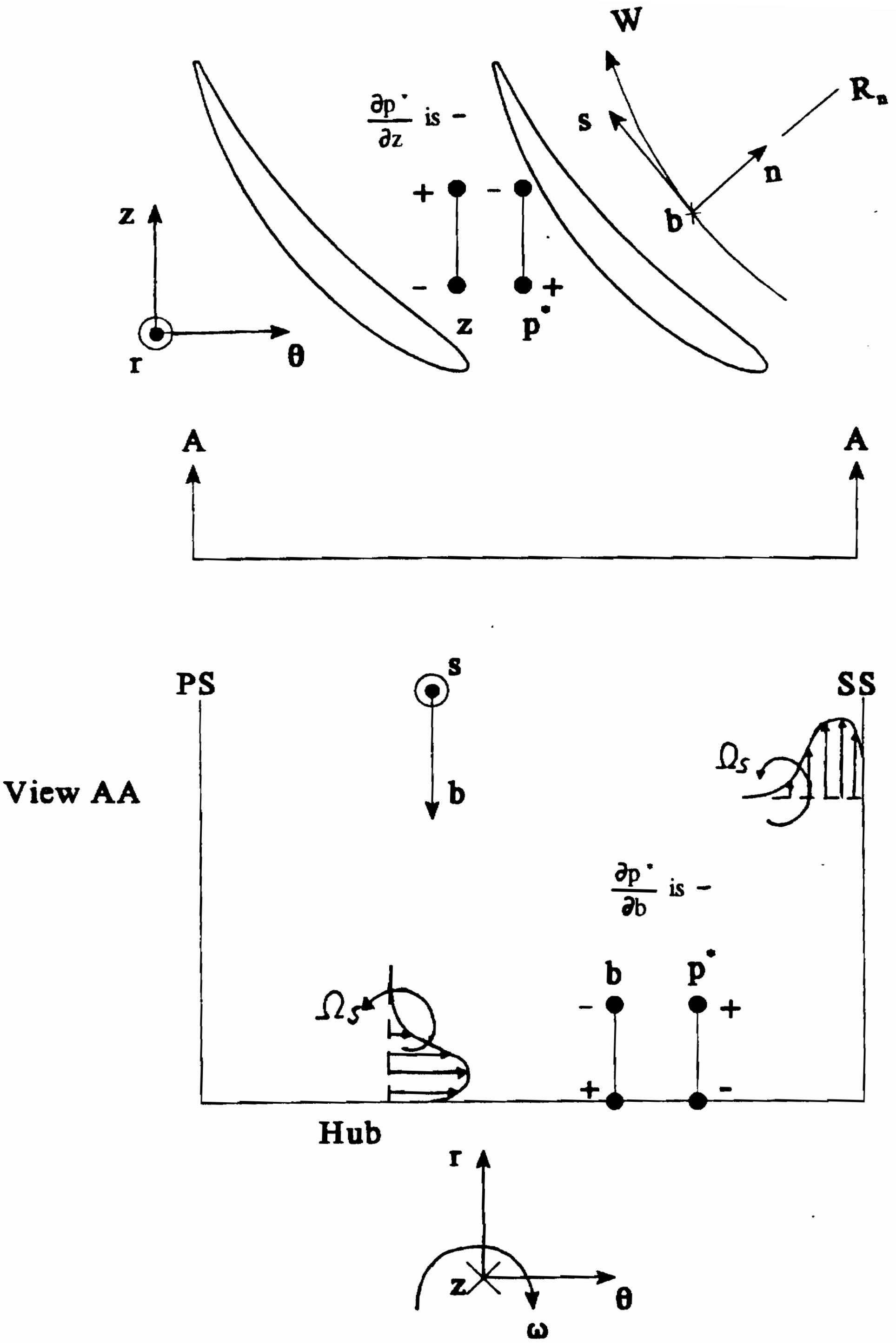

Figure 2.6 Development of Hub and Suction Surface Secondary Flows

2.1.2.3 Radial Migration of Loss Core

Another secondary flow phenomenon associated with the separated flow region is the radial migration of the high loss core away from the hub. Figure 2.7a shows that in the third stage of a four-stage compressor, the loss core has moved from the hub to between 15 and 20% of blade height (Howard et al., 1993). Part of the explanation for this migration up the suction surface comes from the centrifugal effects induced by the rotation. The centrifugal force created acts in a direction normal to the hub surface causing the radially outward flow of the high loss fluid in the corner stall area. Or in other words, the fluid is centrifuged outward.

Another way of visualizing this is to look at the simplified streamwise vorticity generation equation, Eq. 2.1. The second term deals with the angular velocity, ω, about the axis of rotation z. There is a negative gradient of rotary stagnation pressure near the suction surface creating a negative component of Ω_s which produces a radially outward component of velocity in the outer part of the boundary layer. This is illustrated in Figure 2.6.

2.2 Underturning/Overturning

With an understanding of the mechanisms behind corner stall, explaining the characteristic problem of the flow under/overturning in the hub region as seen in Figure 2.7b is easier (Howard et al., 1993). Nearest the hub, the flow is seen to be overturned because of the strong secondary flow pushing fluid toward the suction surface. Where the blade is in the way, the flow is rolled up into the corner stall but downstream of the blade, it is relatively unhindered, resulting in the overturning. The flow then reaches a local maximum of underturning around 20% of span which coincides with the location of the core of high loss fluid. Because the flow convects over the region of backflow, it is forced outward away from the suction surface resulting in underturning.

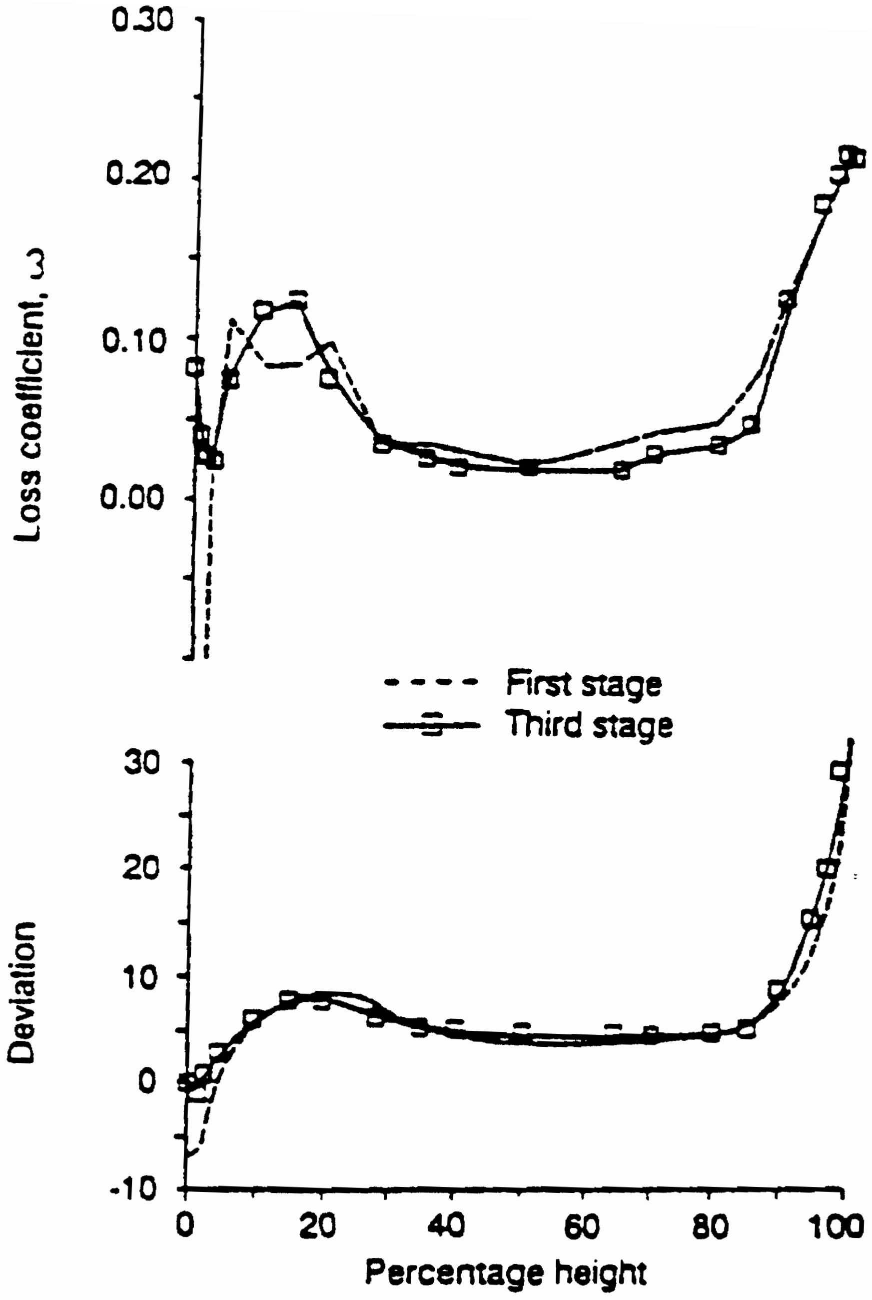

Figure 2.7 Deviation and Loss Coefficient vs. Radius (Howard et al., 1993)

2.3 Transition

The transition of the suction surface boundary layer from laminar to turbulent plays an important role in where the flow separates. Figure 2.8 shows the possible boundary layer states on a blade surface ranging from laminar to a laminar separation bubble, then transitioning to turbulent and then undergoing turbulent separation. The main determining factor for which states the boundary layer will experience is the Reynolds Number. For a Reynolds number greater than 10^6, the boundary layer is generally turbulent from the start. It is for Reynolds numbers in the 10^5 regime that the other states occur. For these lower Reynolds number flows, the freestream turbulence level becomes an important factor in the evolution of the boundary layer.

2.3.1 Freestream Turbulence Level

H. Schlichting and A. Das (1970) performed a cascade study to determine the effect that turbulence level has on the suction surface boundary layer for NACA blade shapes. The top plot in Figure 2.9 shows how transition is affected by turbulence levels for a NACA 65-608 blade shape at a Reynolds number of $Re = 1.6 \times 10^5$. For turbulence levels below 2.5%, the boundary layer starts laminar and then has a laminar separation bubble. The boundary layer then reattaches as turbulent. For turbulence levels above the critical value of 2.5%, transition to a turbulent boundary layer occurs immediately at the leading edge of the blade, with the implication that turbulent separation can occur earlier on the blade surface. The early transition at higher turbulence levels coincides well with flow behavior in the hub region of compressors where turbulence levels are higher than in the free stream region.

The middle plot of Figure 2.9 shows the influence of the turbulence level on the flow turning angle, $\theta = \Delta\beta = \beta_1 - \beta_2$. The flow turning angle is illustrated in Figure 2.2. As the turbulence level is increased, the turning increases from a minimum value of approximately 10.5 degrees till the critical turbulence level of 2.5% is reached. After this point, the turning angle is unaffected by an increase in the turbulence level.

The bottom plot of Figure 2.9 shows the relationship between the flow loss and the turbulence level. The loss starts at a high value for low turbulence levels and then decreases to a minimum value at the critical turbulence level. The loss then increases to about the same value as for low turbulence levels at 8% where it then levels off to a constant value as the turbulence level is increased further.

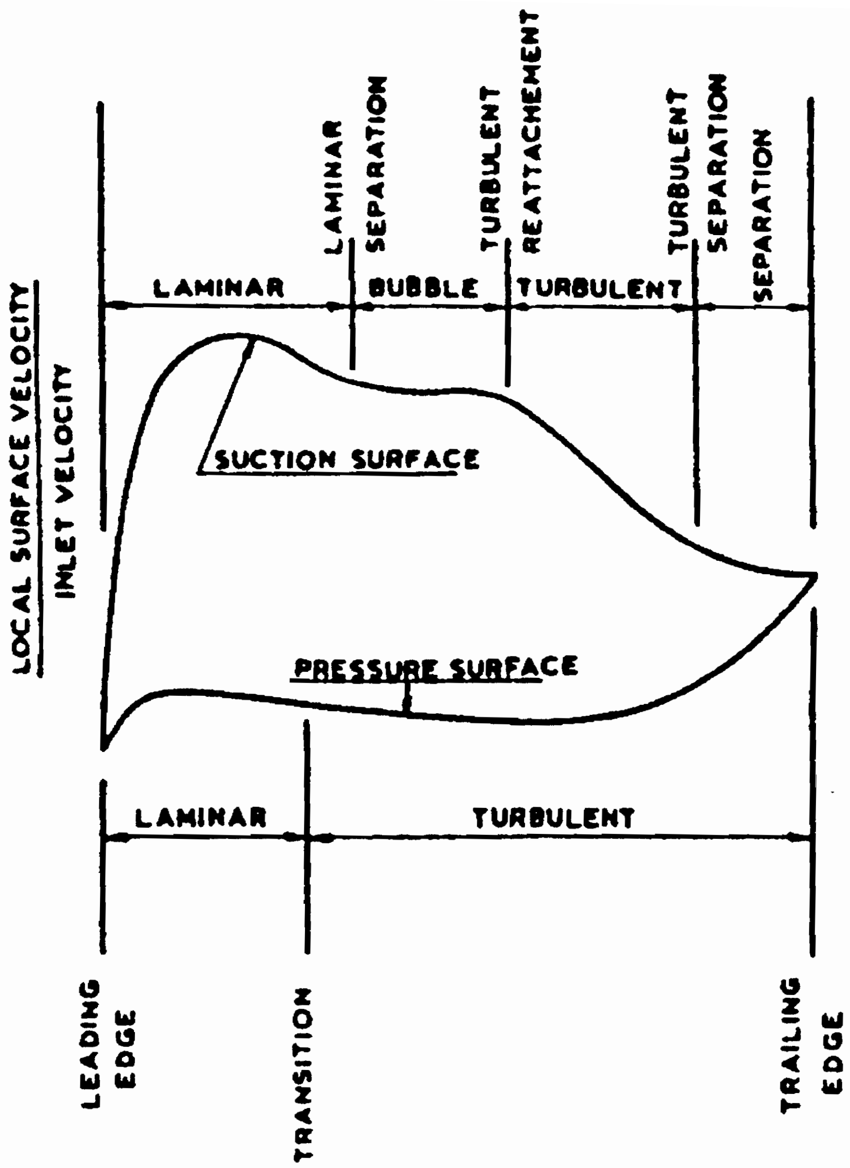

Figure 2.8 Possible Boundary Layer States on a Blade Surface (Seyb, 1972)

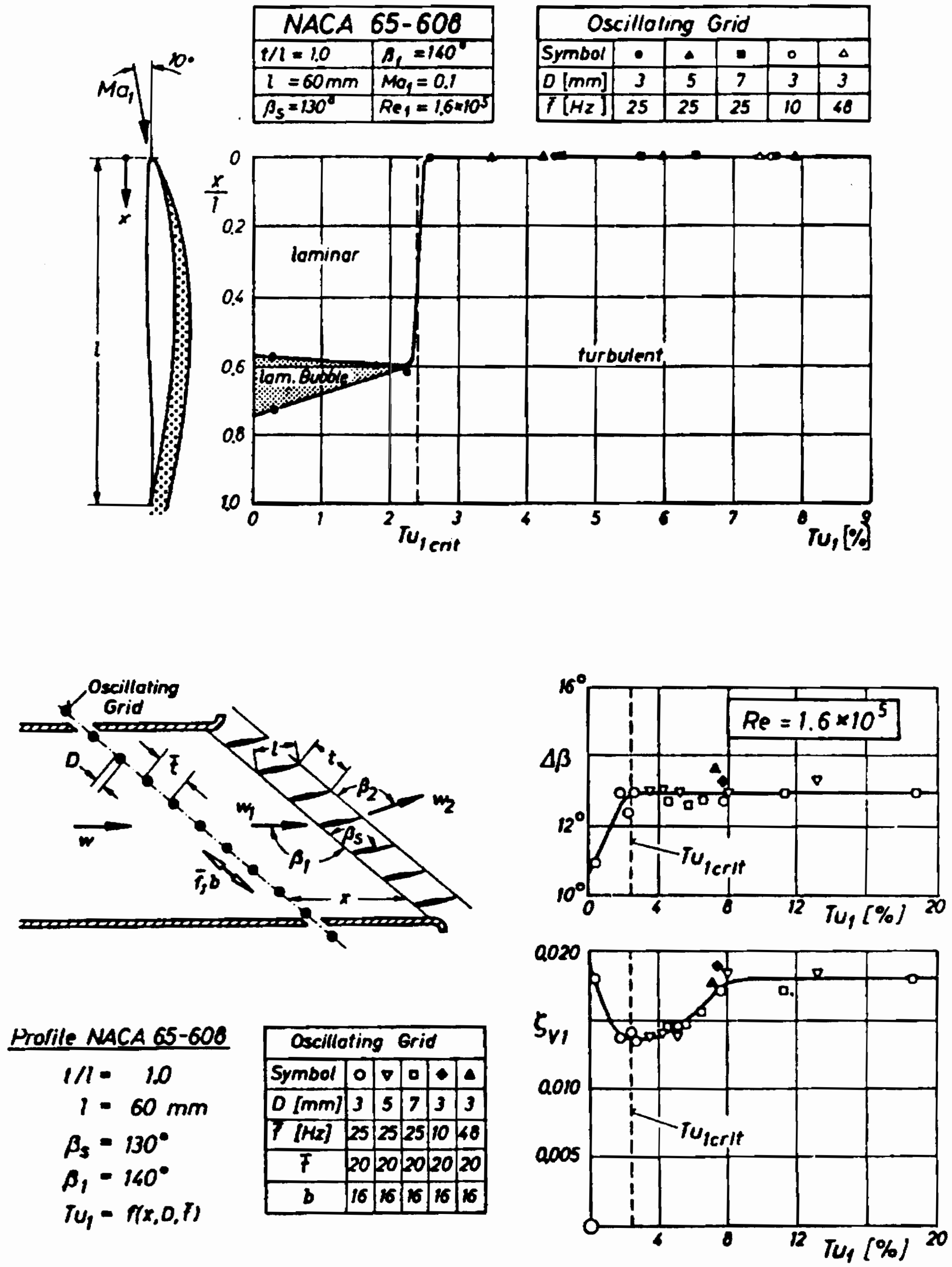

Figure 2.9 Transition Location as a Function of Freestream Turbulence Level (Schlichting and Das, 1970)

2.3.2 Incidence Angle Effects on Transition

The relationship between the boundary layer state and incidence angle was studied by N. J. Seyb (1971). The results from his cascade study are shown in Figure 2.10. The top plot shows how the losses are affected by varying the incidence angle. As the flow inlet angle is varied from the blade angle, the losses increase. The highest losses occur for large positive incidences which are what compressor blades experience in the hub region. These higher losses are due to the earlier transition location and turbulent separation as seen in the second plot.

The second plot depicts the transition location for the different incidence angles. In addition to the experimental results, Seyb also examined methods for predicting the location of transition on the blade surface. For negative incidence angles, the boundary layer begins as laminar with transition occurring after a laminar separation bubble, which is similar to the behavior for low turbulence levels. As the incidence goes positive, the transition location moves closer to the leading edge, with turbulent separation occurring after the incidence reaches +7.5°. The method used to predict transition was based upon a method by B. Thwaites (1949). The method uses the momentum thickness Reynolds number and a pressure gradient parameter in conjunction with correlations to approximate the laminar boundary layer. Details of this method will be given in section 6.2.2.1.

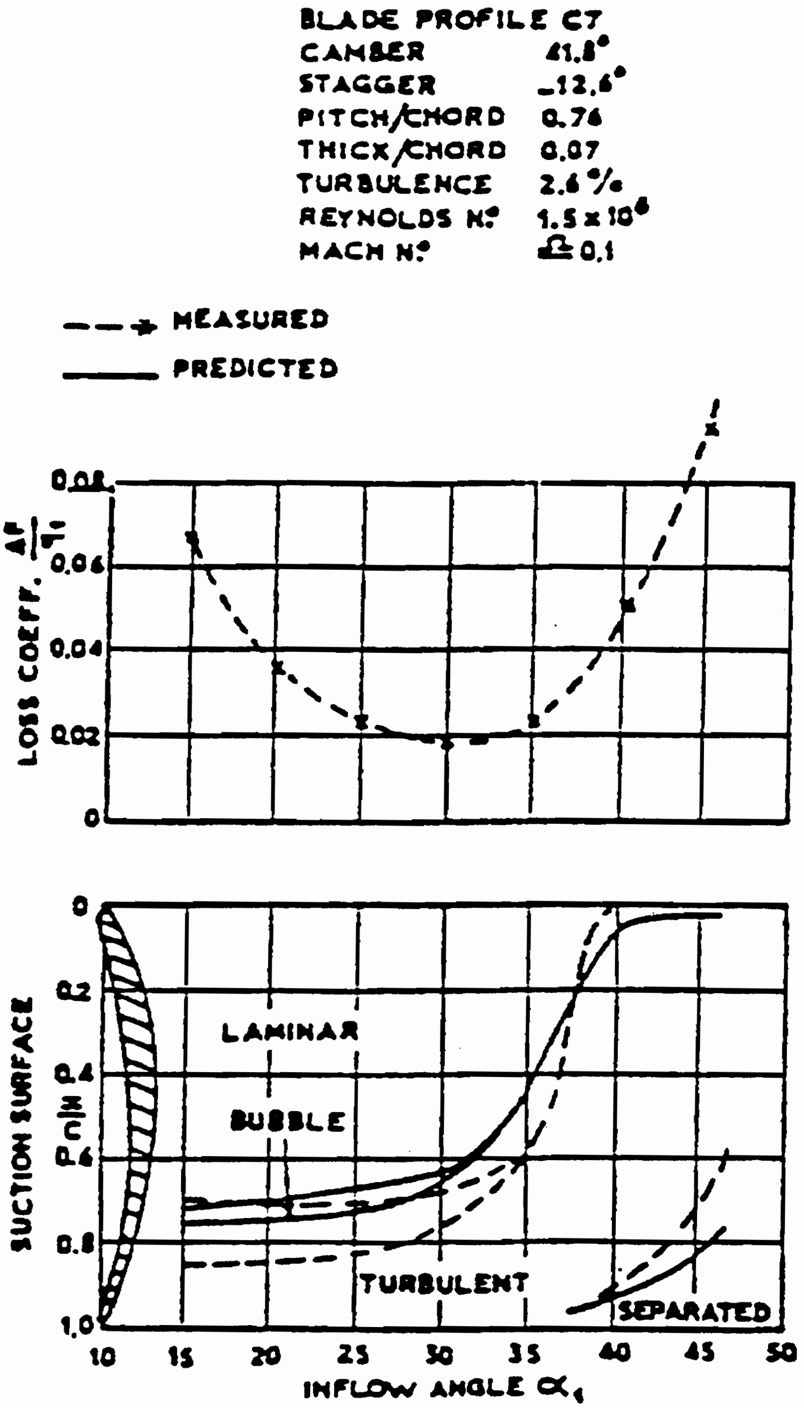

Figure 2.10 Transition Location as a Function of Incidence Angle (Seyb, 1972)

2.4 Deverson Rig

Multi-stage compressors are complex machines that make it difficult to obtain experimental data. Therefore, single stage compressors designed to simulate multi-stage machines are often used to obtain experimental evidence. The purpose of the present study is to predict the flowfield computationally, in particular the separated region, and compare the calculations with experimental data obtained from the Deverson Rig (Place, 1993), a low speed research compressor.

The Deverson Rig is housed at the Whittle Laboratory in Cambridge, England. It is a single stage compressor with C4 free vortex designed blades. There are 51 rotor blades that have 2% of rotor axial chord tip clearance and 36 stator blades. To simulate a multi-stage environment, the machine is fitted with a turbulence grid 5.4 rotor midheight chords upstream of the rotors. The screen produces higher turbulence levels produced normally by upstream stages. A schematic of the Deverson Rig can be seen in Figure 2.11. The discussion of the data from the rig will be restricted to the hub region, on which the present study is focused.

The data presented here was taken downstream of the rotor at Plane G, for a flow coefficient of $\phi = 0.51$. This gives a Reynolds number based on axial chord of 300,000. Figure 2.12 shows the axial velocity contours normalized by the midheight blade speed, $V_z/U_{midheightt}$. This velocity visualization shows the blade wake, the hub and casing boundary layers, and the corner stall. The corner stall is indicated by the core of nearly stagnated fluid at a radius of 630 mm that causes a bulge in the blade wake. That the core of fluid has moved away from the hub indicates the presence of the radial migration discussed earlier. It is this low speed/high loss fluid in the suction surface/hub corner region that causes the characteristic underturning (discussed in section 2.2) which will be shown in a later figure. A second exit axial velocity visualization can be seen in Figure 2.13 which shows the exit axial velocity contours as a circumferentially averaged profile. A local peak velocity of approximately 0.5 seen at 7.5% of the blade height corresponds to the contours that protrude under the high loss core seen in Figure 2.12. This fluid is the hub secondary flow that causes the characteristic overturning in the hub region.

The rotor wake velocity profiles at 23 and 50% span are shown in Figure 2.14. The velocities within the rotor wake at 23% illustrate the dominance of secondary flows within boundary layers along the blade and the corner stall region over the primary or axial velocity. The radial velocity increases significantly and reaches a peak of about 0.08. This is due to the strong radial outward secondary flows along the suction surface. The tangential velocity also increases significantly in the blade wake. The axial velocity slows significantly due to the boundary layers on the blade but also because of the backflow within the separated region of flow in the suction surface/hub corner region.

The rotor wake velocities at 50% span follow the same pattern seen at 23% span. But here the influence of the corner stall is no longer present and the effects are not as large. The radially outward velocity is still present but this secondary flow is not as large at this height. The tangential velocity is relatively unchanged. The axial velocity does not slow nearly as much without the effects of corner stall. A significant difference is the width of the wake has decreased. This is again due to the fact that the effects of the corner stall do not reach this height.

The deviation angles, $\delta = \beta_2 - \beta_2'$ as defined in Figure 2.2, are shown in Figure 2.15. The characteristic hub over/underturning is evident in the figure. The deviation angle is at a local minimum at approximately 5% blade height due to the secondary flow undercutting the core of high loss fluid. This is the overturning. The deviation angle then increases to a local maximum at 15% blade height and decreases to the value found at 5% at 30% blade height. The blockage due to the corner stall is what causes this underturning in the flow.

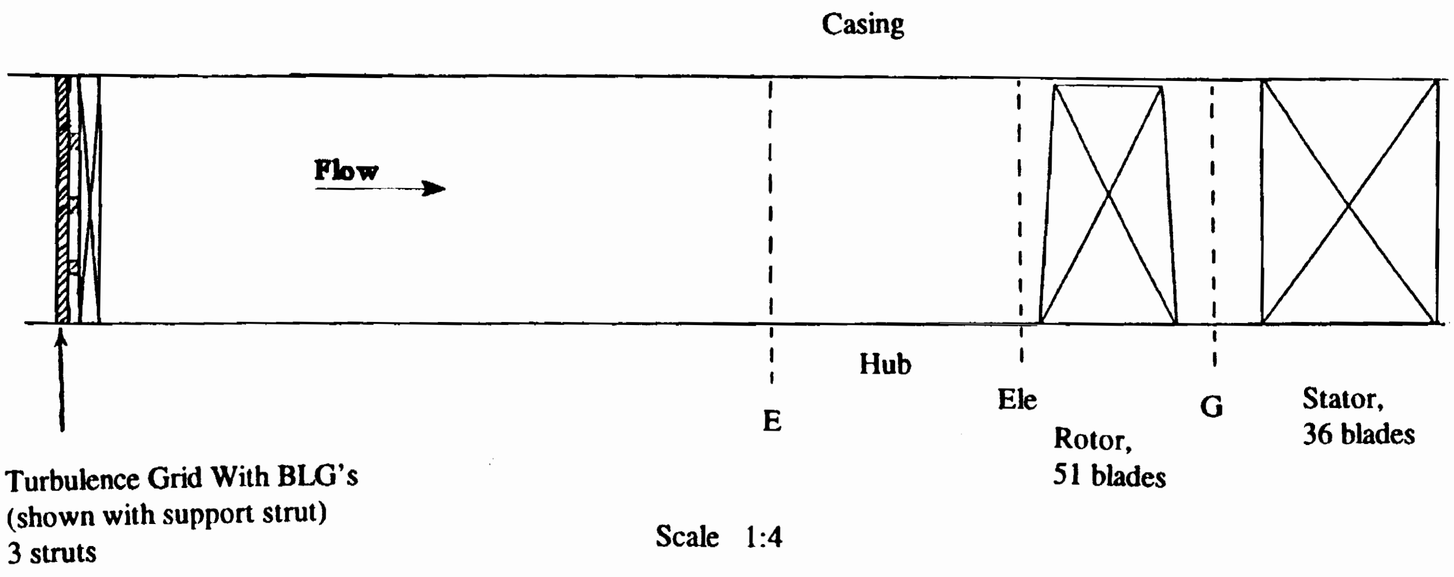

Figure 2.11 Schematic of the Deverson Rig (Place, 1993)

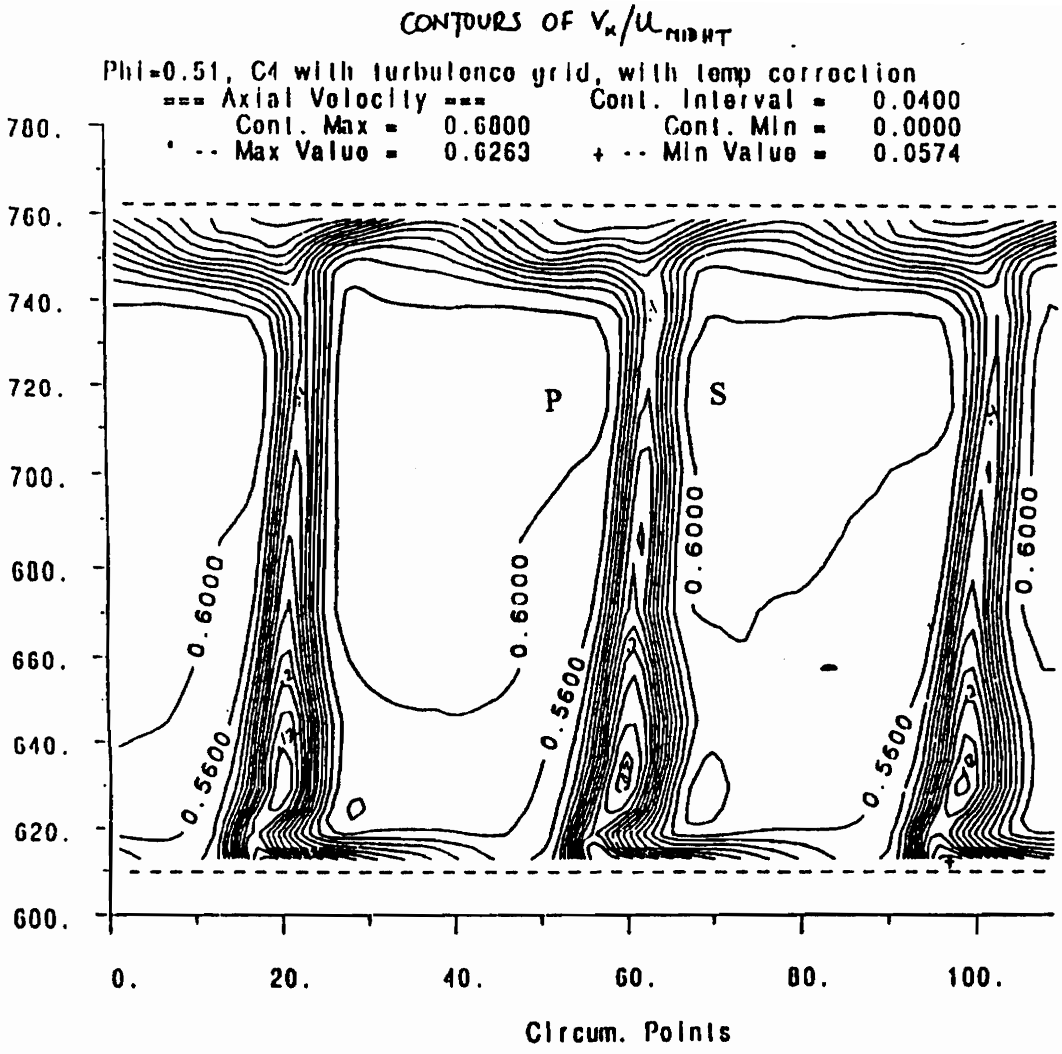

Figure 2.12 Exit Axial Velocity Contours $V_z/U_{\text{midheight}}$ for the Deverson Rig (Place, 1993)

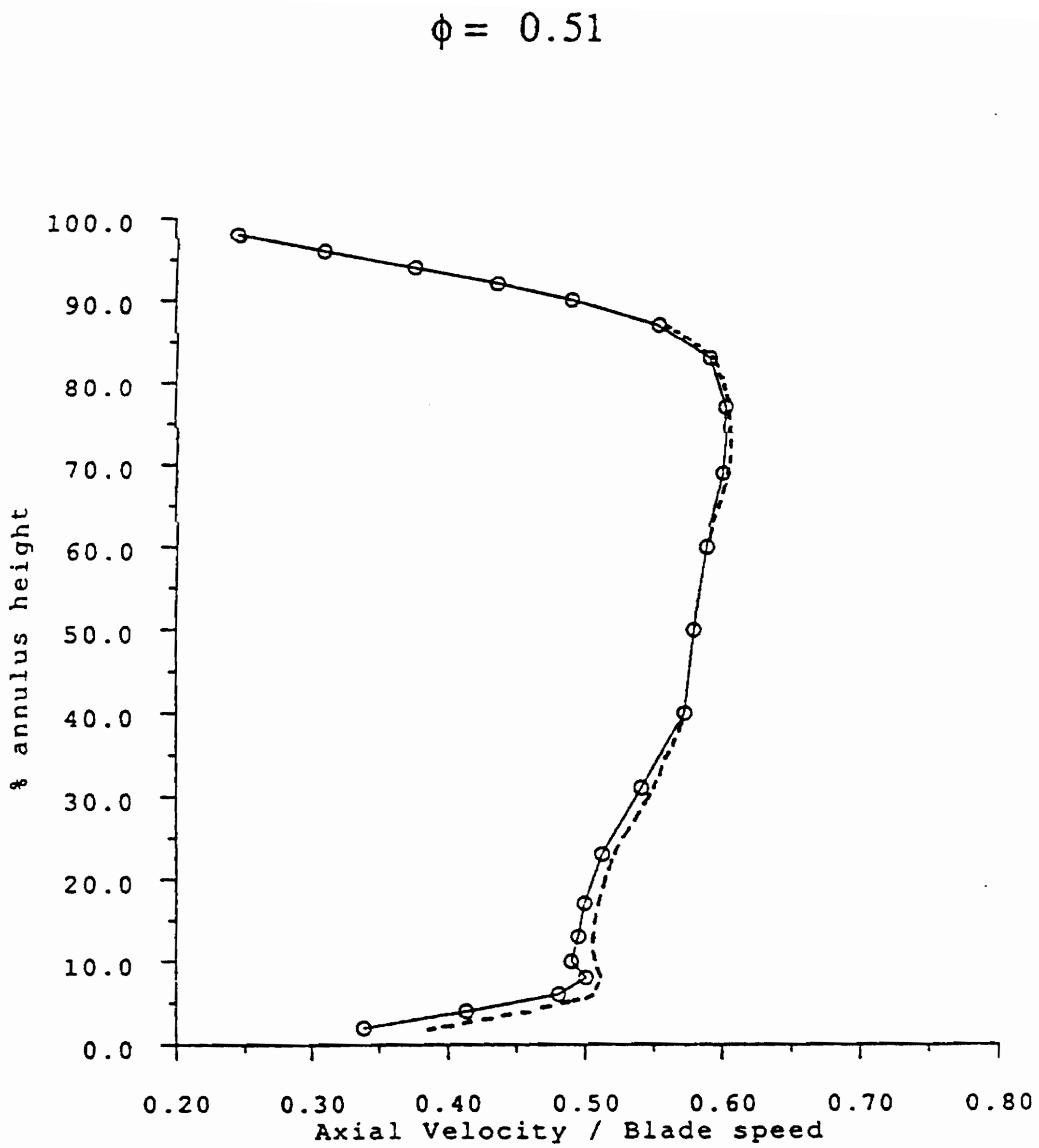

Figure 2.13 Exit Axial Velocity Profiles for the Deverson Rig (Place, 1993)

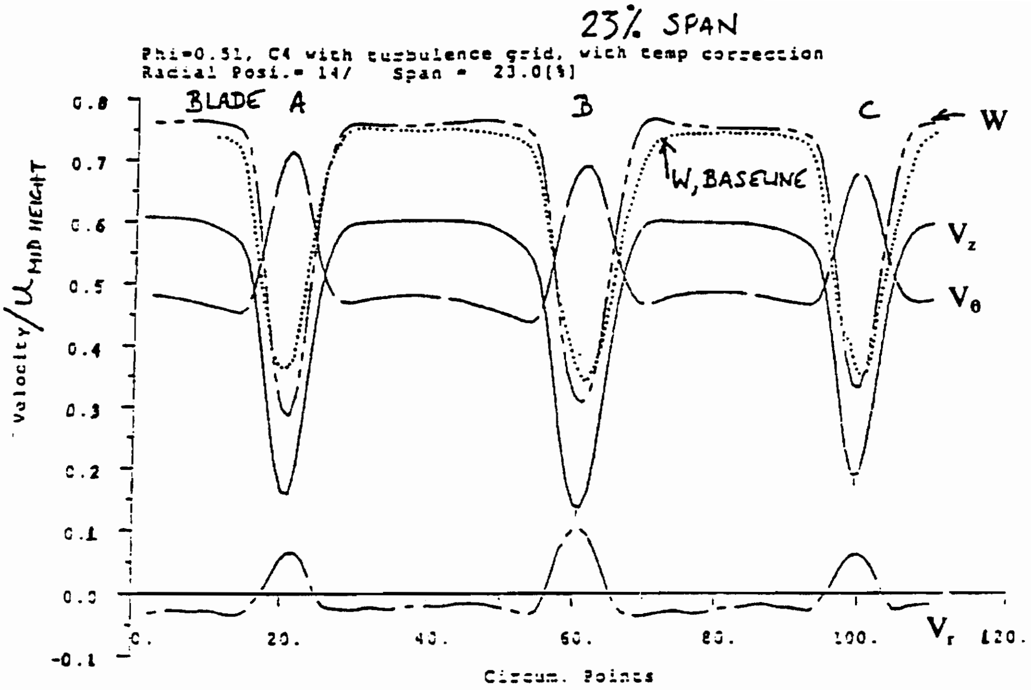

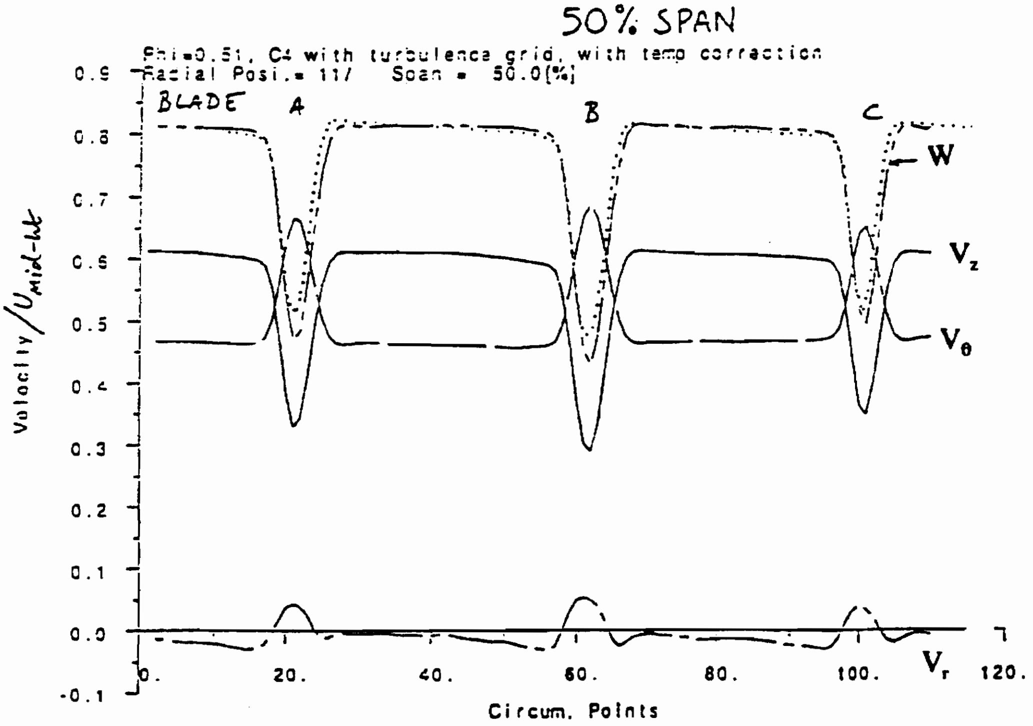

Figure 2.14 Rotor Wake Velocity Profiles for the Deverson Rig (Place, 1993)

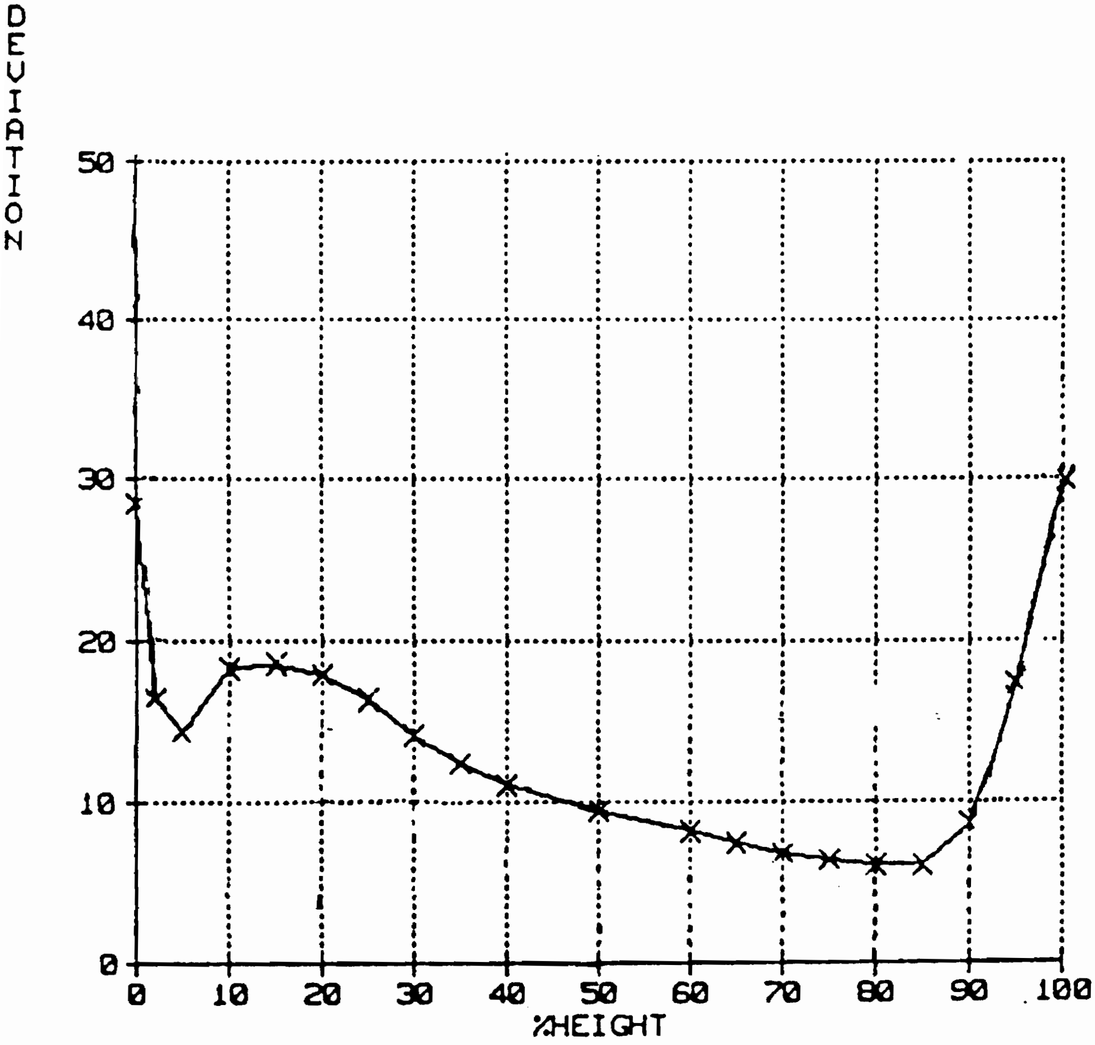

Figure 2.15 Deviation Angles for the Deverson Rig (Place, 1993)

2.5 Modeling

The previously mentioned experimental studies have shown the importance of corner stall and the mechanisms involved in its formation. The next section looks at how the flows can be predicted numerically. The most commonly used CFD codes use the Reynolds averaged Navier-Stokes equations to simulate steady, 3-D, subsonic/sonic, viscous, compressible, turbulent flows.

2.5.1 CFD Codes

Leylek and Wisler in a 1990 computational study calculated the flow through a multi-stage compressor, in particular looking at the flow through the third stator of a four-stage machine. The code they used is based on the Reynolds averaged Navier-Stokes equations using a pressure correction scheme. A two-equation k-ε turbulence model was used to obtain closure for the transport equations. According to Leylek and Wisler, two equation turbulence models are needed to account for mainstream turbulence intensity and length scales when simulating turbulent flows. Zero and one equation turbulence models cannot capture these effects (Leylek and Wisler, 1990). They found good agreement between their computed flow and the experimental flow data for the modeled compressor. The code could predict the suction surface/hub corner separation and the strong secondary flows along the hub.

In another computational study by Kang and Hirsch (1993), the CFD code utilized uses the time-dependent Reynolds averaged Navier-Stokes equations. The zero equation algebraic turbulence model of Baldwin-Lomax was used for closure. This combination of a solver and turbulence model was also able to attain close agreement with the experimental data for flow in a compressor cascade. The calculation predicted the suction surface/hub corner separation including the radial migration of the loss core as seen in Figure 2.16, and the secondary flow along the hub.

Kang and Hirsch also pointed out the importance of modeling the transition of laminar to turbulent flow. It is likely that their calculation over predicts the size of the separated region because the separation will occur earlier on the suction surface due to the assumption that the boundary layer is fully turbulent from the beginning. Both studies also pointed out the influence on the size of the separated region of not modeling effects such as the downstream stators and hub leakage.

Rolls-Royce undertook a computational study of the flow in the Deverson rig using the Moore Elliptic Flow Program, MEFP (Rolls-Royce, 1994). MEFP is described in Chapter 3. It is based on the Reynolds averaged Navier-Stokes equations using a pressure correction scheme. The turbulence model used by Rolls-Royce for closure was a zero equation algebraic mixing length model. The calculation could predict the corner stall detected in the Deverson rig, as illustrated in Figure 2.17. Figure 2.17 shows the axial velocity contours, $V_z/U_{midheight}$, which are meant as a direct comparison with Figure 2.12. The calculation under predicted the size of the separated flow region by a factor of two and failed to capture the radial migration of the loss core.

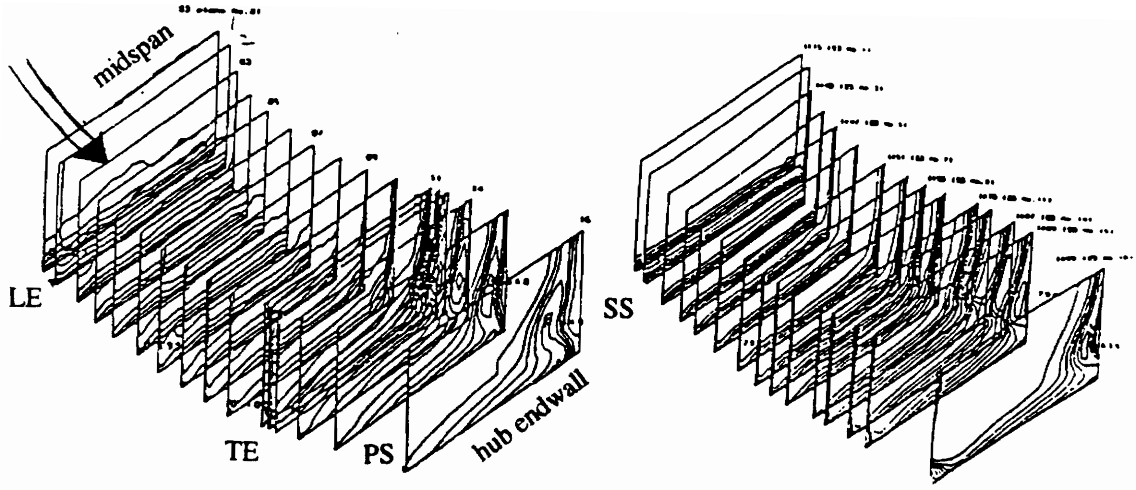

b)

a)

Figure 2.16 Contours of Total Pressure Loss on Traverse Planes at Off-Design Condition for a Compressor Cascade, a) experimental and b) predicted (Hirsch and Kang, 1993)

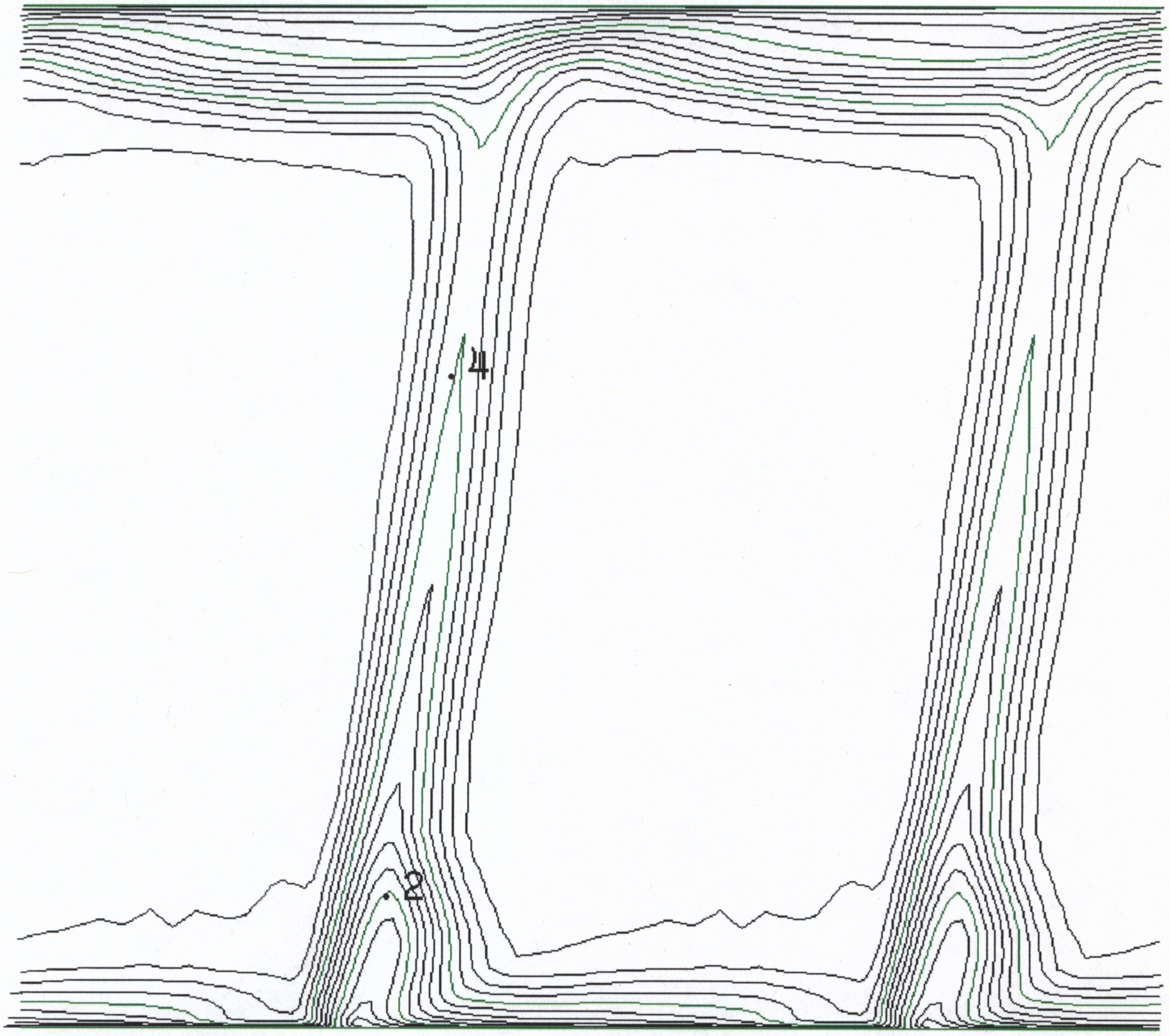

Figure 2.17 Predicted Exit Axial Velocity Contours, $V_z/U_{midheight}$, for the Deverson rig (Rolls-Royce, 1994)

2.5.2 Advantages of CFD Calculations

The main goal of CFD calculations is to predict the flow through a turbomachine accurately. While codes are not yet capable of achieving this, they continue to improve as computer technology steadily improves. The main justification of using CFD calculations is that they cost less than experiments and are much cheaper than actual compressor testing. With a CFD calculation, the ability to look at small scale flow features is possible by increasing the resolution of the grid. This means that we can look closely at the underlying physics of the flow, increasing our understanding of the flow through turbomachines and enabling the design of more efficient and powerful machines.

For every grid point, there are available all of the variables relevant to analysis. One advantage to this is the ability to calculate secondary flow fields plane by plane, giving the ability to track the evolution of vortices and evaluate their impact on the overall performance. In addition, the convection of low energy boundary layer fluid to the suction surface/hub corner can be computed and visualized aiding in a better physical understanding of the secondary flows.

Another advantage is the ability to calculate streaklines and separation lines over the entire flow quickly and inexpensively. This allows an understanding of how the end wall effects and separated flow regions affect the overall flow characteristics. Figure 2.18 (Leylek and Wisler, 1990) shows the streaklines on the suction and hub surfaces. The streaklines on the suction surface for the flow design point are shown in plot a with the streaklines for the case of increased loading shown in plot b. These two plots clearly shown how the presence of the corner stall can significantly affect the flow through the rotor, with the flow being affected for the first 40% of blade height. The third and fourth plots, c and d in Figure 2.18 depict the computed streaklines along the hub surface. Again, it is obvious the impact that corner stall has on the flowfield.

Figure 2.19 shows the how streaklines can help in visualizing the flow in three dimensions. The figure illustrates both the secondary flow along the hub, corner stall, and the interaction between the two.

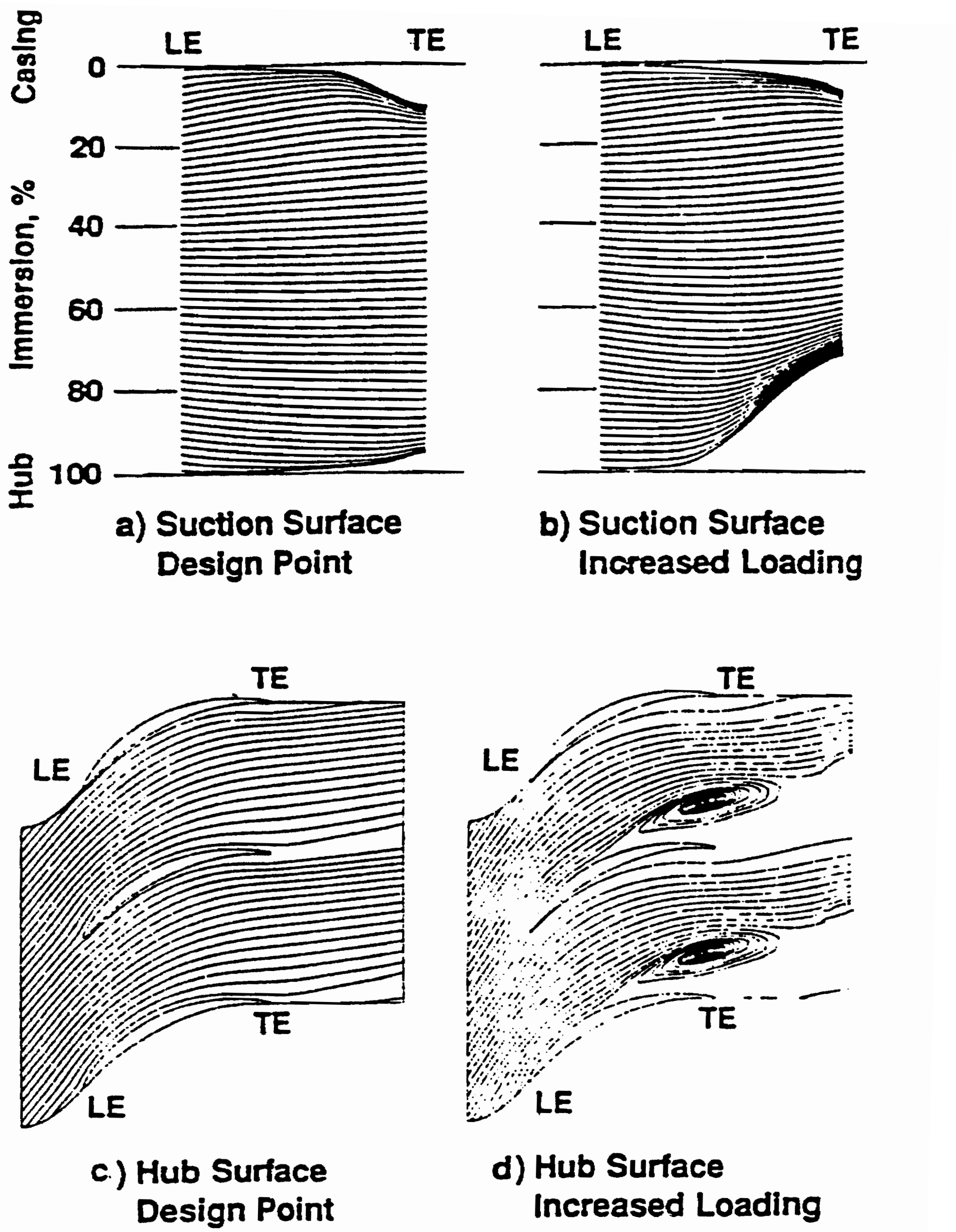

Figure 2.18 Streaklines Showing Corner Stall on the Suction and Hub Surfaces (Leylek and Wisler, 1990)

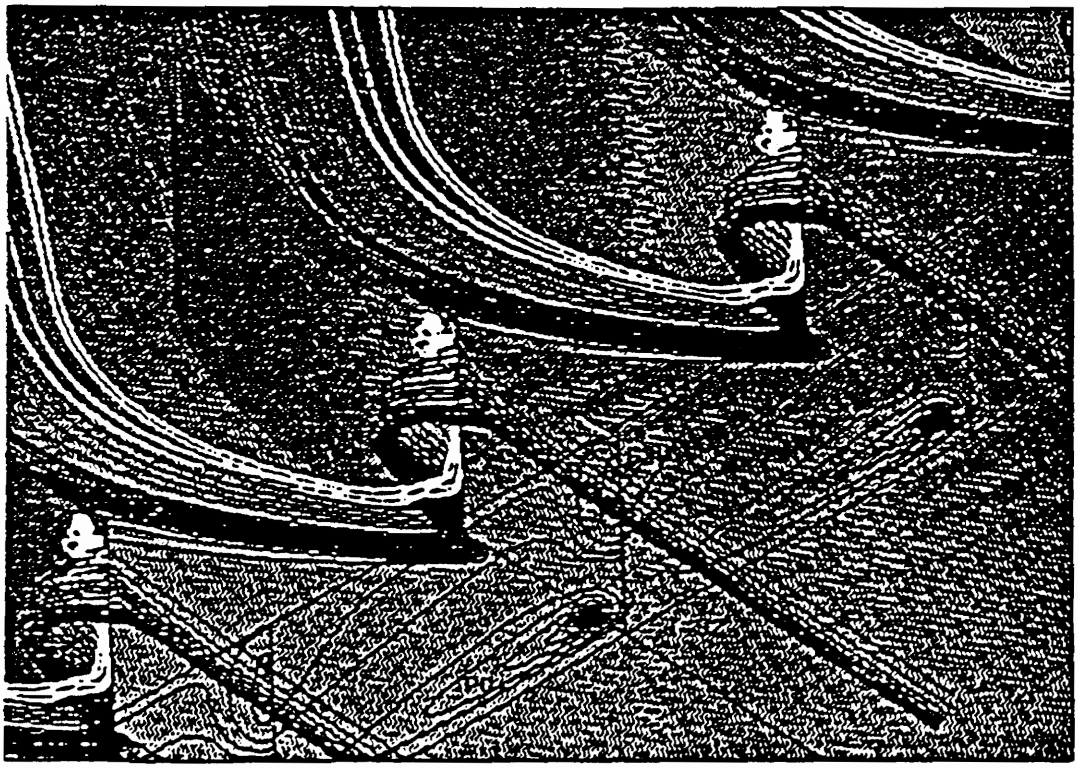

Figure 2.19 Three-Dimensional Streaklines Showing Flow in the Corner Stall Region (Hirsch and Kang, 1993)

2.6 Plan of Study

The purpose of the present study is computationally to predict the flowfield in the Deverson rig using MEFP's one equation q-L transitional turbulence model. The size and location of the hub corner stall region are of particular interest.

A grid was generated which satisfied known requirements of the q-L turbulence model. 2-D sections were taken from this for use in cascade flow studies. The accuracy of the q-L model was tested by a 2-D calculation that was quantitatively compared with an experimental NACA 2-D cascade study.

To aid in the understanding of how MEFP predicts some relevant flow phenomena, two computational studies were undertaken. In particular, the 2-D calculations investigated the influence of turbulence intensity and incidence angle on boundary layer transition and separation.

As seen in the literature, the analysis of hub corner stall is facilitated by the use of streakline tracking. Therefore, a streakline program was added to the existing flow visualization tools for MEFP flowfields.

The two-dimensional studies completed, a three-dimensional calculation of the flow in the Deverson rig was undertaken using the q-L transitional turbulence model. A detailed analysis of the transition and separation on the suction surface followed. The secondary flows affecting the corner stall were also investigated via streakline analysis. In addition to this calculation, a preliminary calculation was performed using a q-ω

turbulence model that is currently under development.

3.0 The Moore Elliptic Flow Program

3.1 Governing Equations

The MEFP (Moore, 1994b) solves three-dimensional, viscous, compressible, steady flows through turbomachinerary blade rows using the Reynolds averaged Navier-Stokes equations. The governing equations for steady flow in the rotating reference frame are as follows:

1. Conservation of mass

$$\nabla \cdot \rho \underline{u} = 0 \qquad \textbf{(Eq. 3.1)}$$

2. Conservation of momentum

$$\rho \underline{u} \cdot \nabla \underline{u} - \nabla \cdot \mu_{eff} \nabla \underline{u} = \nabla \cdot \mu_{eff} \overline{\nabla \underline{u}}^{T} - \nabla p - 2\rho \underline{\Omega} \times \underline{u} - \rho \underline{\Omega} \times (\underline{\Omega} \times \underline{r}) \qquad \textbf{(Eq. 3.2)}$$

3. Conservation of energy

$$\rho \underline{u} \cdot \nabla H - \nabla \cdot \mu_{eff} \nabla H = 0 \qquad \textbf{(Eq. 3.3)}$$

4. Equation of state

$$p = \rho R T \qquad \textbf{(Eq. 3.4)}$$

$$H = C_p T + 0.5(\underline{u} \cdot \underline{u}) - 0.5(\underline{\Omega} \times \underline{r} \cdot \underline{\Omega} \times \underline{r}) \qquad \textbf{(Eq. 3.5)}$$

where u̲ is the relative velocity vector and H is the rothalpy.

3.2 Turbulence Models

MEFP has two mixing length turbulence models, a zero equation algebraic Prandtl mixing length model, and a one equation q-L model that calculates either fully turbulent or transitional flows. Both models calculate the mixing length, L, from: 0.41 times the distance to the nearest wall, "y", 0.08 times the boundary or shear layer thickness, δ, or a free stream value. For both models the effective viscosity is the sum of the laminar and turbulent viscosities

$$\mu_{eff} = \mu_l + \mu_t \qquad \textbf{(Eq. 3.6)}$$

except for near-wall points where a logarithmic averaging is used to reduce sensitivity to near-wall grid spacing. Here the effective viscosity is

$$\mu_{eff} = \mu_l \sqrt{\frac{\mu_l + \mu_t}{\mu_l}} \qquad \textbf{(Eq. 3.7)}$$

3.2.1 Prandtl Mixing Length Model

The Prandtl mixing length model calculates the turbulent viscosity from

$$\mu_t = \rho L^2 \frac{\text{"du"}}{\text{dy}} F_{vd}$$ **(Eq. 3.8)**

where "du/dy" is the effective velocity gradient. The van Driest factor in 0.41"y" regions is found by

$$F_{vd} = \left(1 - \exp\left(\frac{-\text{"y"}\sqrt{\rho\mu_{eff}\frac{\text{"du"}}{\text{dy}}}}{26\mu_\ell} \right) \right)^2$$ **(Eq. 3.9)**

and outside the 0.41"y" regions $F_{vd}=1$. There are two choices for the value of "du/dy", the first is the magnitude of the absolute vorticity vector,

$$\frac{\text{"du"}}{\text{dy}} = |\nabla \times \mathbf{u}_{abs}|$$ **(Eq. 3.10)**

and the second is the deformation tensor calculated by

$$\frac{\text{"du"}}{\text{dy}} = \left(\left(\frac{\partial u_i}{\partial x_j} + \frac{\partial u_j}{\partial x_i} \right) \frac{\partial u_i}{\partial x_j} \right)^{1/2} .$$ **(Eq. 3.11)**

In the present study, Eq. 3.10 is used to find the effective velocity gradient.

3.2.2 Transitional q-L Turbulence Model (Moore, 1990)

The one equation q-L turbulence model calculates the turbulent viscosity by

$$\mu_t = C_\mu \rho q L F_{vd} F_{tu,\mu} \qquad \textbf{(Eq. 3.12)}$$

The turbulence parameter, q, which is the square root of the turbulence kinetic energy,

$$q = \sqrt{k} = \sqrt{\frac{u'^2 + v'^2 + w'^2}{2}} \qquad \textbf{(Eq. 3.13)}$$

and is solved from the differential equation

$$\rho \underline{u} \cdot \nabla q - \nabla \mu_{eff} \nabla q = P_q - D_q \qquad \textbf{(Eq. 3.14)}$$

The terms on the right side of the equation represent the production and dissipation rates of q which balance the convection and diffusion terms on the left side. Turbulence kinetic energy production and dissipation are modelled by:

$$P_q = 0.5 C_\mu \rho L F_{vd} F_{tu,p} \left(\frac{\text{"du"}}{dy} \right)^2 = \frac{1}{2} \frac{\mu_t}{q} \left(\frac{\text{"du"}}{dy} \right)^2 \qquad \textbf{(Eq. 3.15)}$$

$$D_q = 0.5 C_\mu^3 \rho F_{vd}^{0.5} F_{tu,d} \frac{q^2}{L} \qquad \textbf{(Eq. 3.16)}$$

The van Driest correction is found by

$$F_{vd} = 1 - e^{\left(\frac{-A_\mu K y \rho q}{\mu_l}\right)} \qquad \textbf{(Eq. 3.17)}$$

The constants for the equations are: $K = 0.41$, $A_\mu = 0.0295$, $C_\mu = 0.548$

In the boundary (or shear) layers, the mixing length, L, is

$$L = \text{smaller of } K_y \text{ and } A_d \qquad \textbf{(Eq. 3.18)}$$

Outside of the boundary layers the mixing length is taken as a constant,

$$L = L_{fre} \qquad \textbf{(Eq. 3.19)}$$

To obtain a smooth and continuous mixing length at the edge of boundary layers, the mixing length is modified outside the layer so that the slope is less than K.

$$\left|\frac{\partial L}{\partial y}\right| \leq K \qquad \textbf{(Eq. 3.20)}$$

The modification factor found in the viscosity, production, and dissipation terms, $F_{tu,n}$, is what allows fully turbulent or transitional calculations. For fully turbulent flows, F_{tu} is set to 1. For transitional flows, F_{tu} is a function of R_{tu}

$$F_{tu,n} = f(R_{tu}) \qquad \textbf{(Eq. 3.21)}$$

R_{tu} is determined by integrating across the boundary layer

$$R_{tu} = A_d C_\mu \int_0^\delta \left(\frac{\rho q}{\mu_l} \right) dy \qquad \textbf{(Eq. 3.22)}$$

and then F_{tu} is applied in the boundary layer. In the free stream regions $F_{tu} = 1$. To avoid a jump in F_{tu} at the edge of the boundary layers, F_{tu} is limited where necessary by

$$\frac{\partial (L F_{tu})}{\partial y} \leq K \qquad \textbf{(Eq. 3.23)}$$

4.0 Grid Generation

The C4 blade geometry for the Deverson rotor was provided by Rolls-Royce in the form of a 3-D grid containing five radial planes. From this a skeleton grid was extracted as shown in Figure 4.1 which contains the inlet and exit planes, the repeating boundaries, and the blade profile. The grid is in MEFP format where the blade is a box in grid space. The leading and trailing edges are each defined by 9 points and the pressure and suction surfaces each have 32 points.

4.1 Grid Characteristics

The MEFP requires several grid characteristics to perform correctly. Figure 4.2 shows the main characteristics. The ratio of the spacing of consecutive points should be ≤ 2 as shown in Figure 4.2a. The aspect ratio of cells in the free stream shown in Figure 4.2b needs to be ≤ 10. The last characteristic is change in the grid line direction, which should be as smooth as possible as seen in Figure 4.2c (Moore, 1994b). The angle formed between the line segments connecting consecutive grid points should be as close to 180 degrees as possible to acquire grid smoothness.

In addition, the q-L turbulence model needs to have uniform near-wall spacing. Developing a new procedure to set a uniform near-wall spacing for the first several lines surrounding the blade with a spacing factor of two as shown in Figure 4.2a was necessary. The free stream aspect ratio and grid smoothness can be optimized within the existing grid optimization program GOPTW.

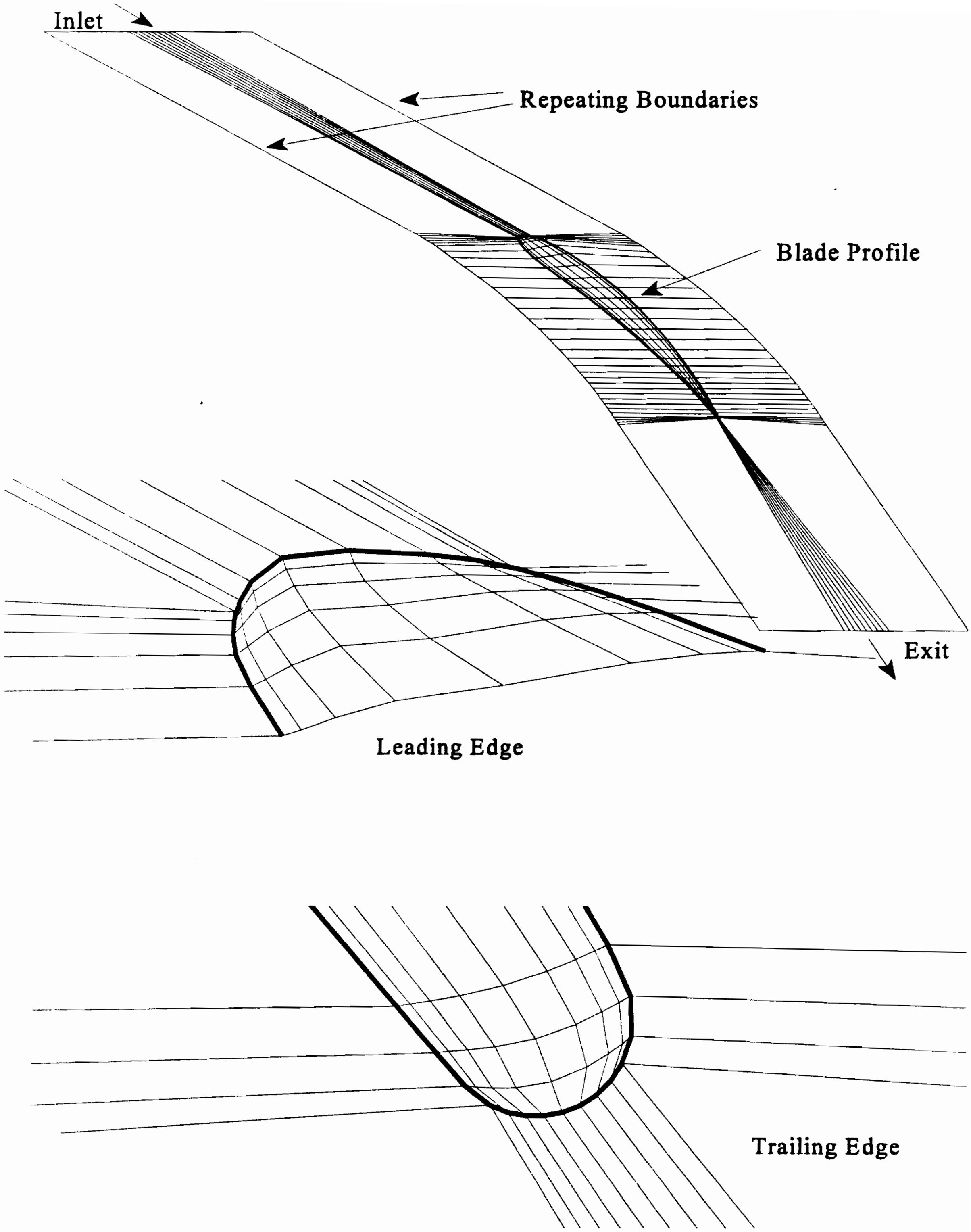

Figure 4.1 Skeleton Grid of Rotor Geometry at Midheight(Rolls-Royce, 1994)

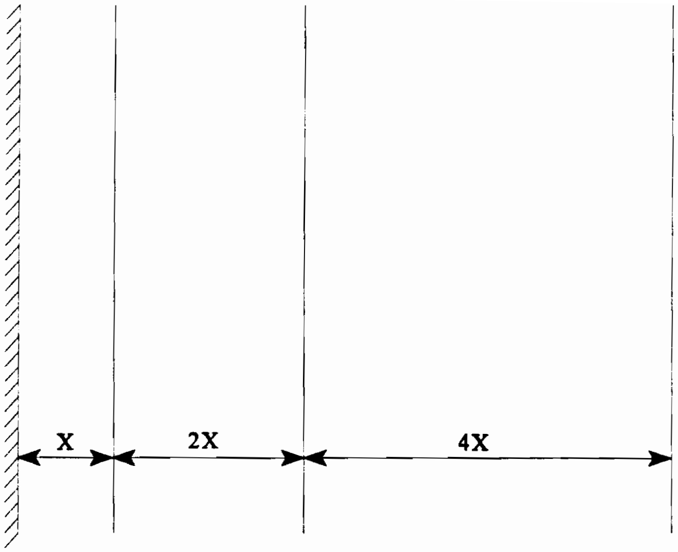

Figure 4.2a Grid line spacing factor = 2

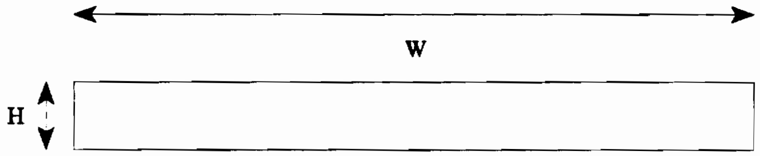

Figure 4.2b Free stream W/H <= 10

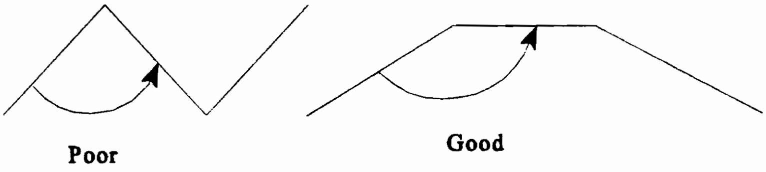

Figure 4.2c Grid Smoothness

Figure 4.2 Grid Characteristics

4.2 Steps in Grid Generation

4.2.1 Corner Point Selection

All of the steps taken to generate the grid were done on each of the five radial planes. The first step was to choose the corner points on the leading and trailing edges to satisfy the following criteria. The upstream grid line directions, Gj1 and Gj2 in Figure 4.3, and the downstream grid line directions were chosen, and the corner points, C1 and C2, were selected to maximize the smoothness of the grid. A second factor in corner selection was to make the two angles formed by the grid lines where they intersect the blade corner point as similar as possible. The sets of angles are: $\alpha_{Gi1,C1}$, $\alpha_{Gj1,C1}$, and $\alpha_{Gi2,C2}$ and $\alpha_{Gj2,C2}$. Figure 4.3a shows the leading-edge corner point locations for the skeleton grid. The pressure surface leading-edge corner point, C1, was moved and the upstream grid line direction, Gj1 was adjusted to allow the optimization program to satisfy these factors. The new leading-edge corner points, C1 and C2, and the grid line directions, Gj1 and Gj2, can be seen in Figure 4.3b.

4.2.2 Specifying the Near-Wall Spacing

Selecting a small enough near-wall distance to guard against the possibility of the boundary layer being lost in the linear interpolation from the wall to the near-wall point is important (Moore, 1994b). An approximate value for the near-wall distance is found by modeling the leading-edge flow as a laminar boundary layer growing on a cylinder and then estimating the boundary layer displacement thickness, δ_1, at $\Phi = 90$ degrees.

From Schlichting (1979),

$$\frac{\delta_1}{R}\left(\frac{\rho W_1 R}{\mu}\right)^{\frac{1}{2}} \sim 0.9 \qquad \textbf{(Eq. 4.1)}$$

where R is the radius of the leading edge, and W_1 is the inlet relative velocity. For the Deverson Rig: $R = 0.00133$ m, $\rho = 1.2$ kg/m^3, $\mu = 2.0 \times 10^{-5}$ kg/ms, and $W_1 = 41.11$ m/s. This gives a value of 2.1×10^{-5} m for δ_1. A factor affecting the final choice of the near-wall distance is the value of y+ calculated by

$$y^+ \equiv y\,\frac{\sqrt{\rho\tau}}{\mu_1} \qquad \textbf{(Eq. 4.2)}$$

$$\tau \sim \mu_{\mathrm{eff}}\,\frac{|W_{\mathrm{near-wall}}|}{D_{\mathrm{norm}}} \qquad \textbf{(Eq. 4.3)}$$

$$\therefore\; y^+ = \sqrt{\rho\,\mu_{\mathrm{eff}}\,\frac{|W_{\mathrm{near-wall}}|}{D_{\mathrm{norm}}}}\;\frac{D_{\mathrm{norm}}}{\mu_1} \qquad \textbf{(Eq. 4.4)}$$

Here, D_{norm} is the normal distance between a point on the blade surface and the adjacent near-wall point. Previous validation studies of the q-L model (Janikiraman, 1993) have shown that for y^+ values of around 10, the model does well. A near-wall distance of 0.0001 m was selected. An initial estimate of y^+ using the free stream velocity and laminar viscosity as approximations of the near-wall velocity and effective viscosity gives a y^+ value of 14. Verification of acceptable y^+ values will be done after the first 2-D calculation.

4.2.3 Near-Wall Grid Lines

The selection process for a generic grid point is shown in Figure 4.4a. The near-wall grid points were added along the grid line direction, $\underline{P}$, at a uniform near-wall distance, D_{norm}, from the adjacent line segments. The smaller angle, $\measuredangle$ P23, created by the grid line direction and the adjacent blade line segments, 1-2-3, was chosen for the calculation of the grid point location, P. The process for creating the corner points was to construct a parallelogram as shown in Figure 4.4b. The next layer of grid lines was created in the same manner as if the previous line was the blade. The process was repeated until four sets of grid lines surrounded the blade. Figure 4.5 shows the leading and trailing edge regions for this case. Due to curvature effects for this blade geometry around the leading and trailing edges, this method is not valid for distances greater than 0.002 m, or 2% of chord, from the wall.

4.2.4 Remaining Grid Lines

The repeating boundaries and rotating boundaries were set next. The inlet plane was placed 66% of chord upstream of the leading edge and the exit plane was set 43% of chord downstream of the trailing edge. Additional grid lines were added with spacing factors of two or less out to a free stream grid with uniform spacing. This gave a 60 x 29 x 5 grid seen in Figure 4.6 at the midheight radial plane. The grid was then optimized using GOPTW. The optimization process did not affect the near wall spacing but could move the points parallel to the blade surface to optimize for grid smoothness and cell aspect ratios. The resulting grid at midheight is shown in Figure 4.7.

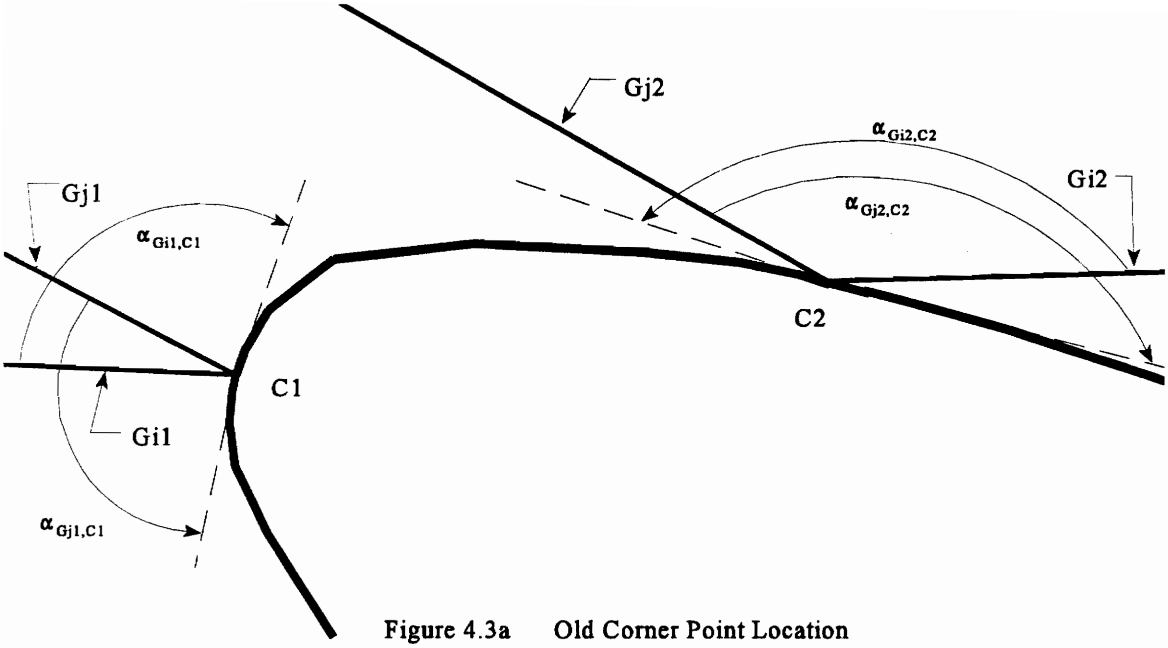

Figure 4.3a Old Corner Point Location

Figure 4.3b New Corner Point Location

Figure 4.3 Blade Corner Point Selection

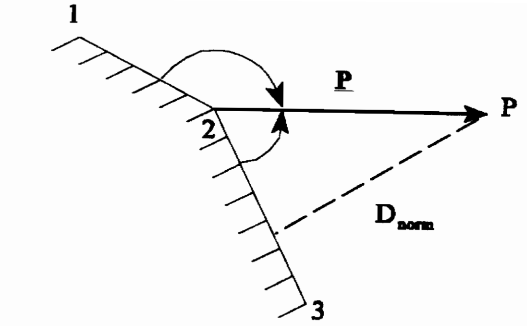

Figure 4.4a Generic Grid Point Selection

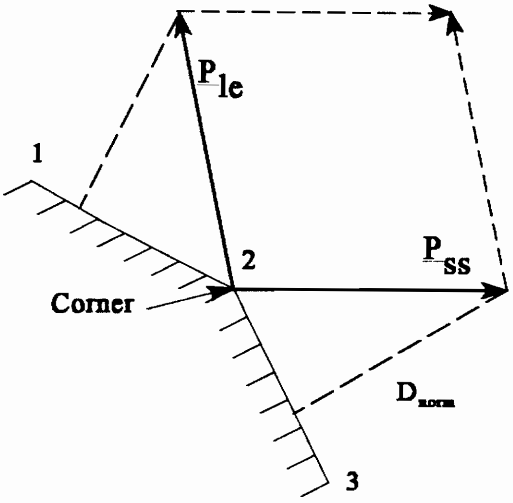

Figure 4.4b Corner Control Volume formed by Parallelogram

Figure 4.4 Method for Finding Grid Points

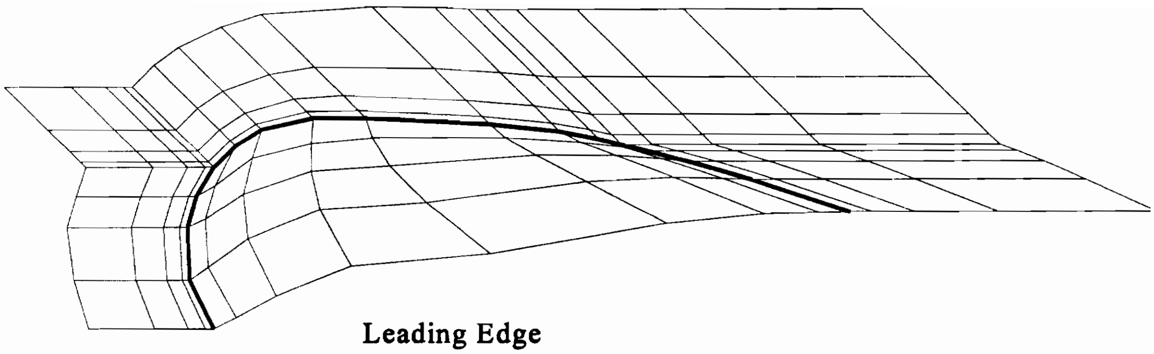

Leading Edge

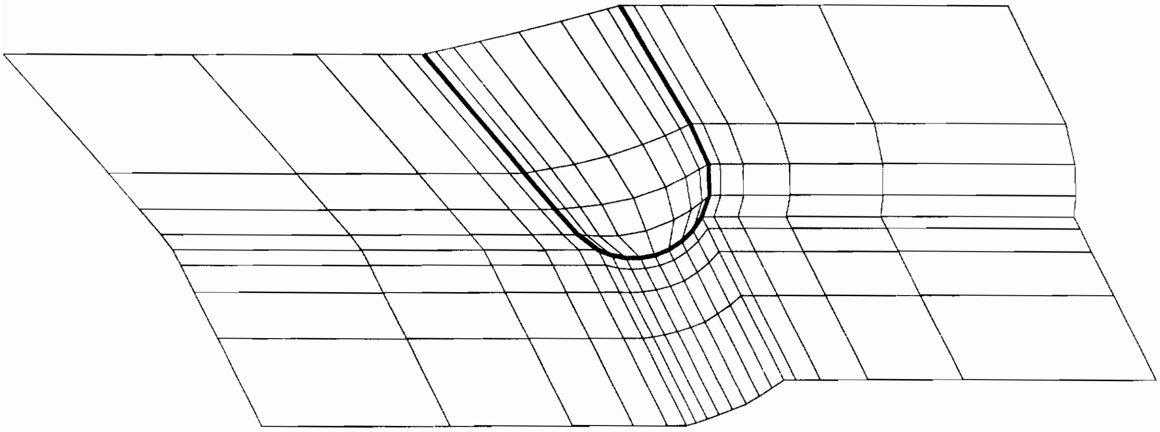

Trailing Edge

Figure 4.5 Uniformly Spaced Grid Lines

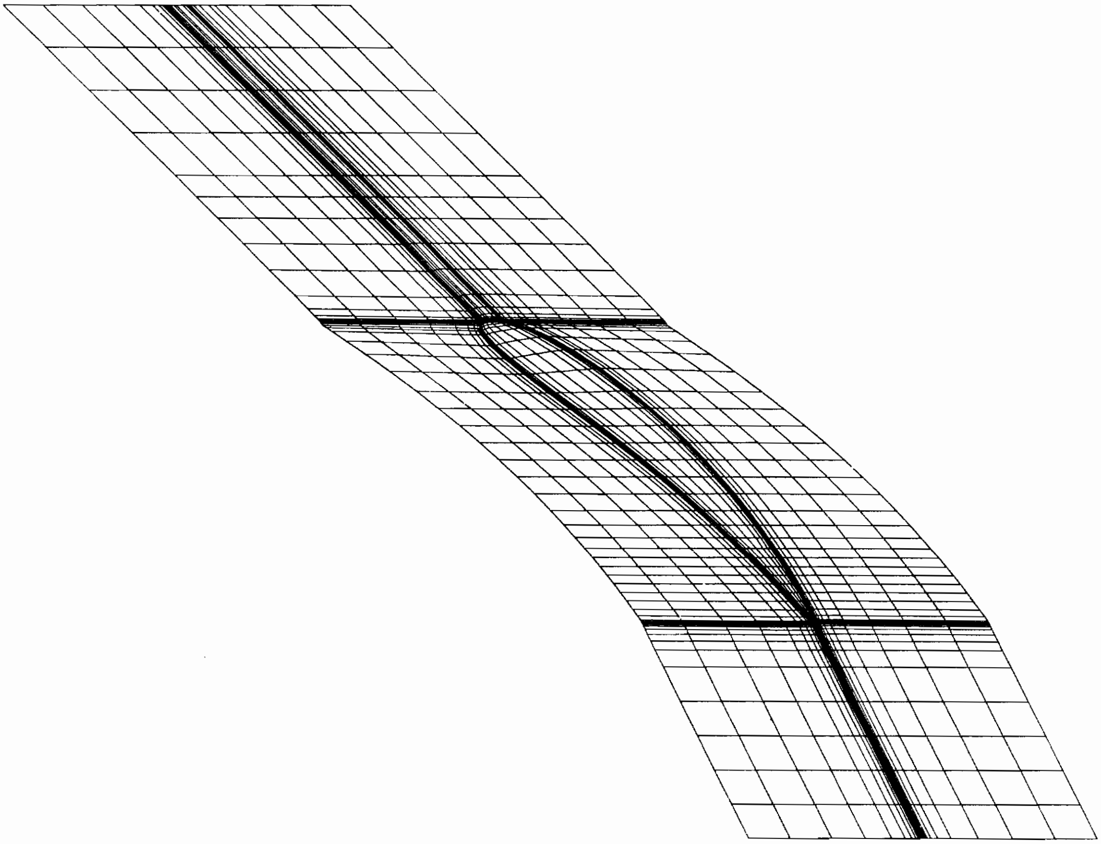

Figure 4.6 60 x 29 x 5 Unoptimized Grid at Midheight

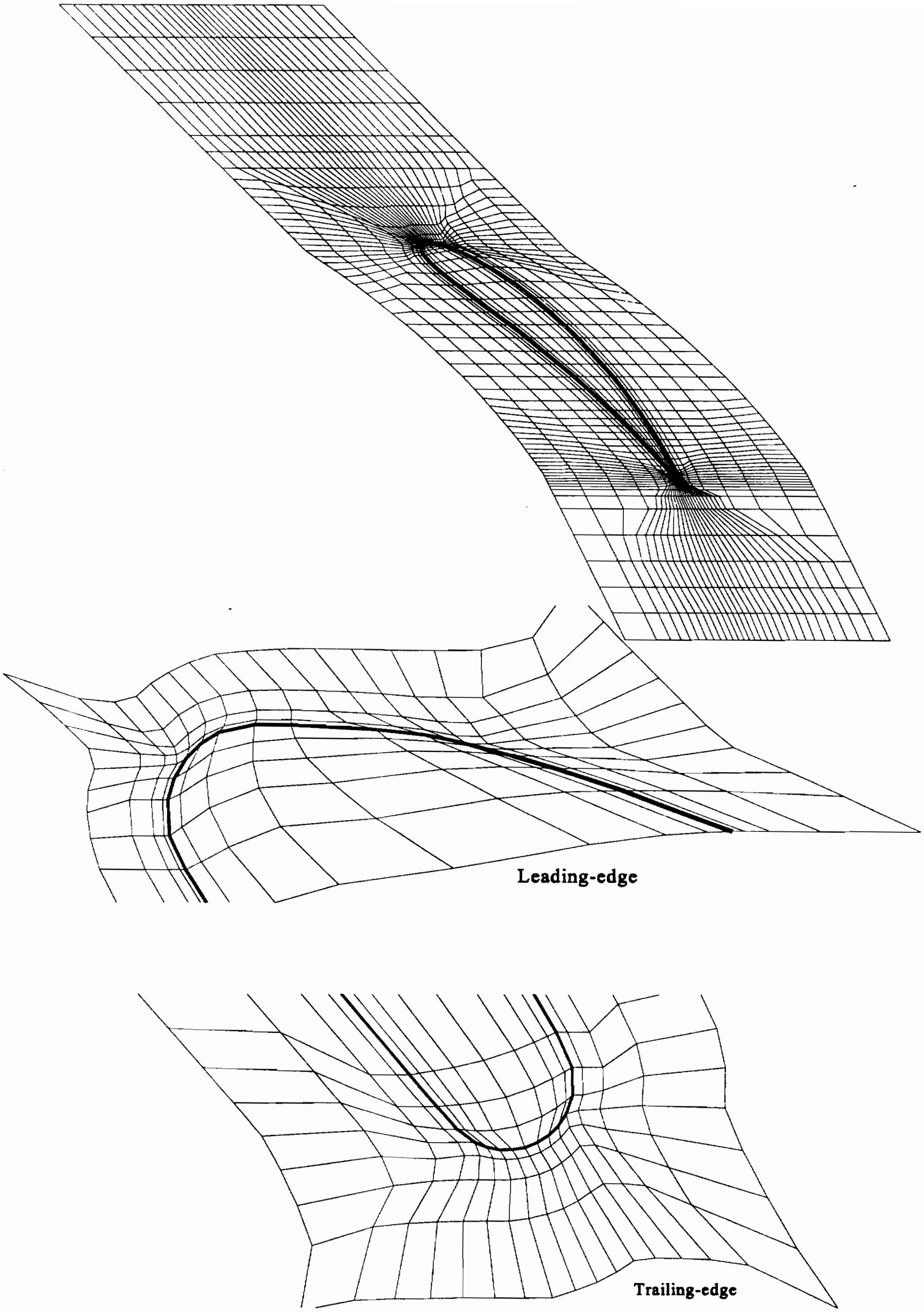

Figure 4.7 60 x 29 x 5 Optimized Grid at Midheight

4.3 2-D Grid Sections for Cascade Studies

To make a comparison with a NACA cascade study of C4 blading (Felix and Emery, 1959), a grid section was needed with $\beta_1' \approx 60°$ and $\beta_2' \approx 30°$. In the free vortex design of the Deverson rig blading, this section existed. So the Rolls-Royce geometry/grid could be used to set up a grid corresponding to the blades used in the NACA study. A 2-D section was created from the 3-D grid at a radius of 0.6604 m. The grid section has an inlet camber-line angle of 60.22 degrees and exit camber-line angle of 30.14 degrees. The solidity, chord over spacing, of this section had to be modified to a value of one for an accurate comparison to be made. The resulting grid can be seen in Figure 4.8.

The unmodified 2-D section which will be used in the cascade studies for incidence angle and turbulence intensity effects on boundary layer separation can be seen in Figure 4.9.

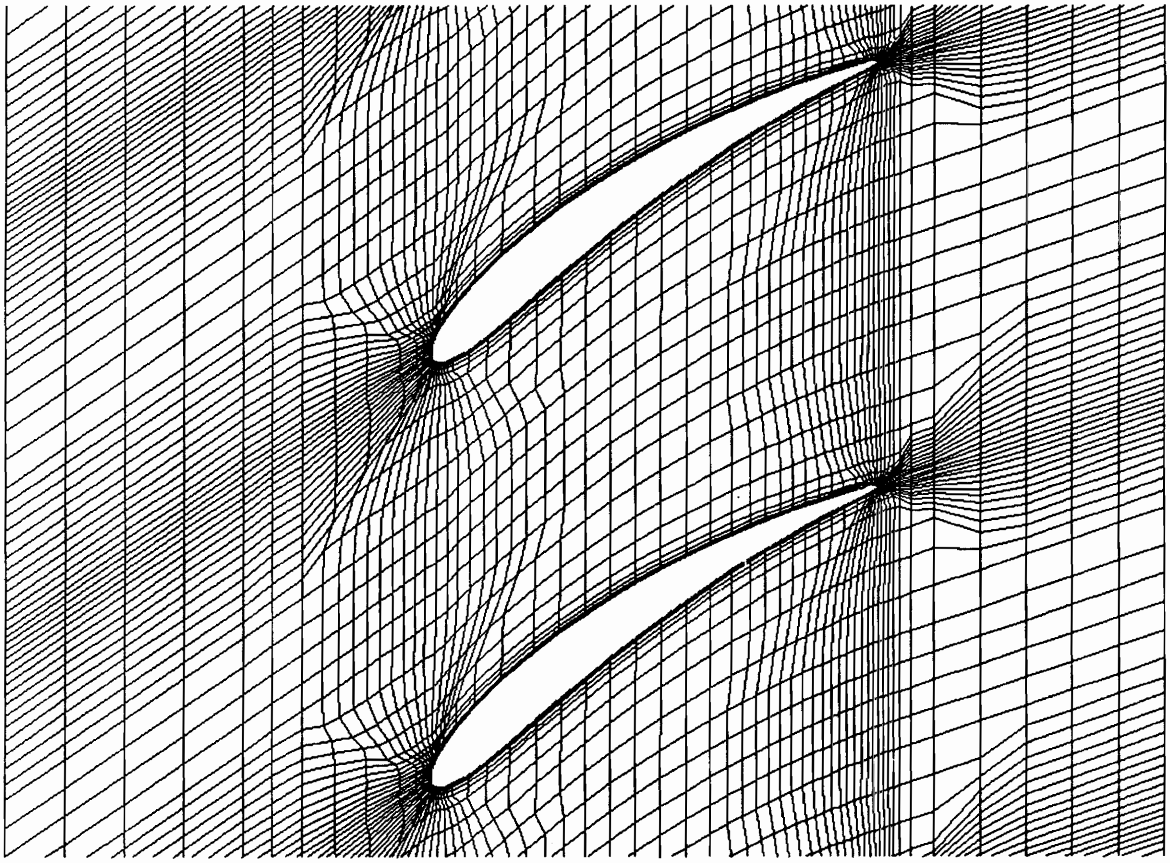

Figure 4.8 2-D Grid Section with a Solidity of One for NACA Comparison

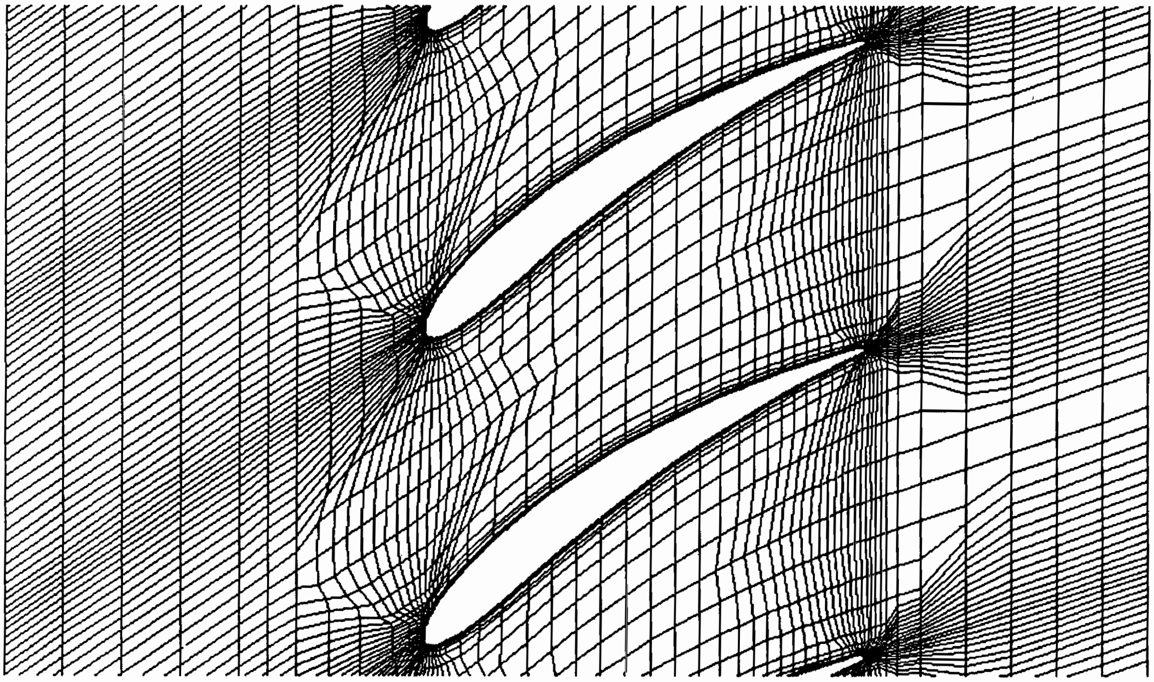

Figure 4.9 Unmodified 2-D Grid Section for Turbulence and Incidence Studies

4.4 3-D Radial Planes

The 3-D grid was completed by the addition of radial planes. The near-hub and near-shroud distance is the same as the near-wall distance. Again a grid line spacing factor of two was used, decreasing to one in the free stream region. The tip gap is 2% of the midheight chord of 0.111 m. This corresponds to a grid space C value of 0.9854 with 0 being the hub and 1 being the shroud. The C values are listed in Table 4.1. The resulting grid in r-z coordinates can be seen in Figure 4.10. Figure 4.11a is a closeup of the hub/leading edge region and Figure 4.11b is a closeup of the hub/trailing edge region.

Table 4.1 C Values for 3-D Calculation Grid

Plane	C Value	Plane	C Value	Plane	C Value
1	0.0	10	0.25	19	0.975884
2	0.000656	11	0.35	20	0.9854
3	0.001968	12	0.45	21	0.990158
4	0.004593	13	0.55	22	0.9954069
5	0.009842	14	0.65	23	0.9980319
6	0.020341	15	0.75	24	0.9993438
7	0.041339	16	0.84266	25	1.0
8	0.083334	17	0.918788		
9	0.167324	18	0956852		

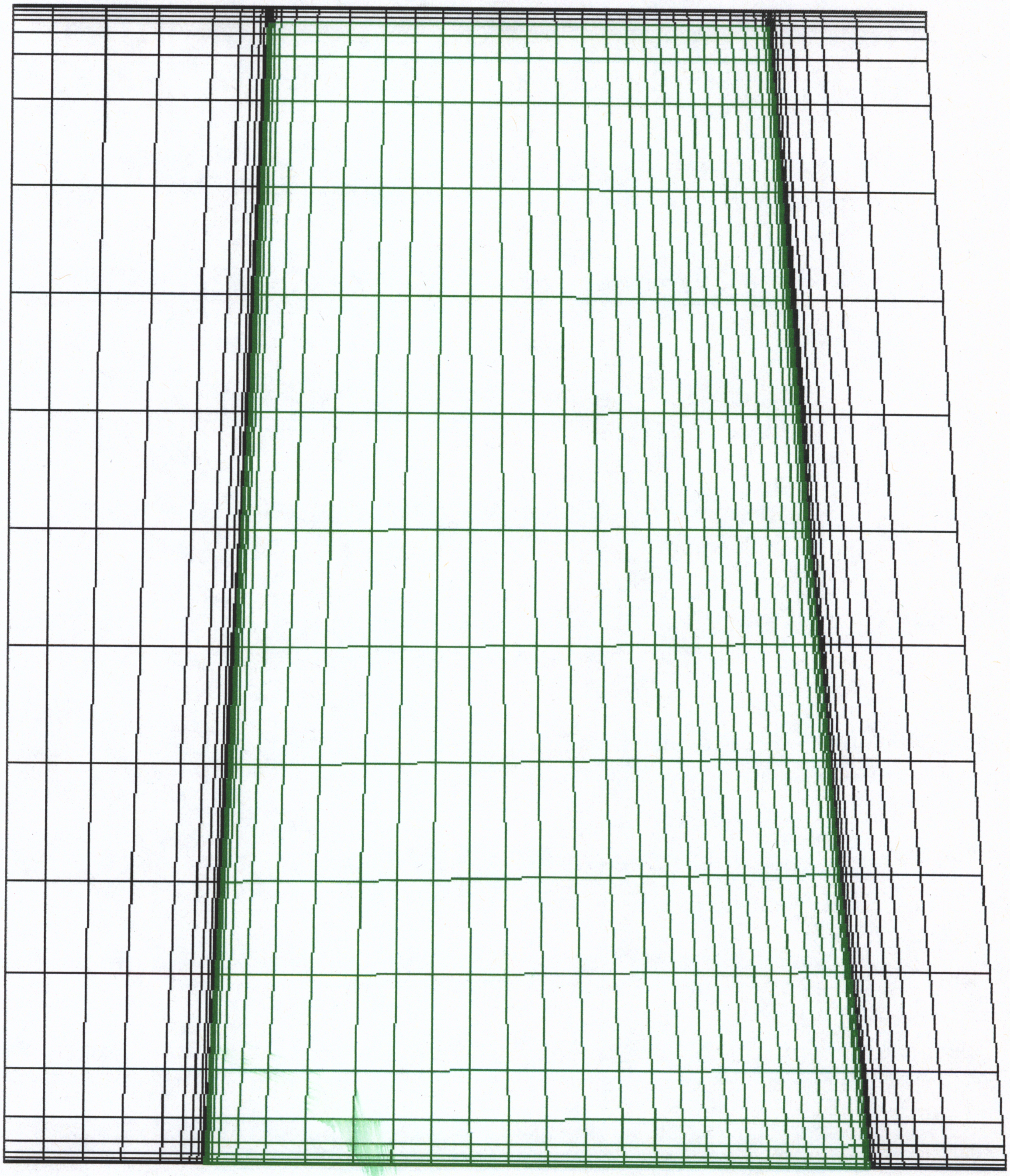

Figure 4.10 Final 3-D Grid Showing Spacing of Radial Planes

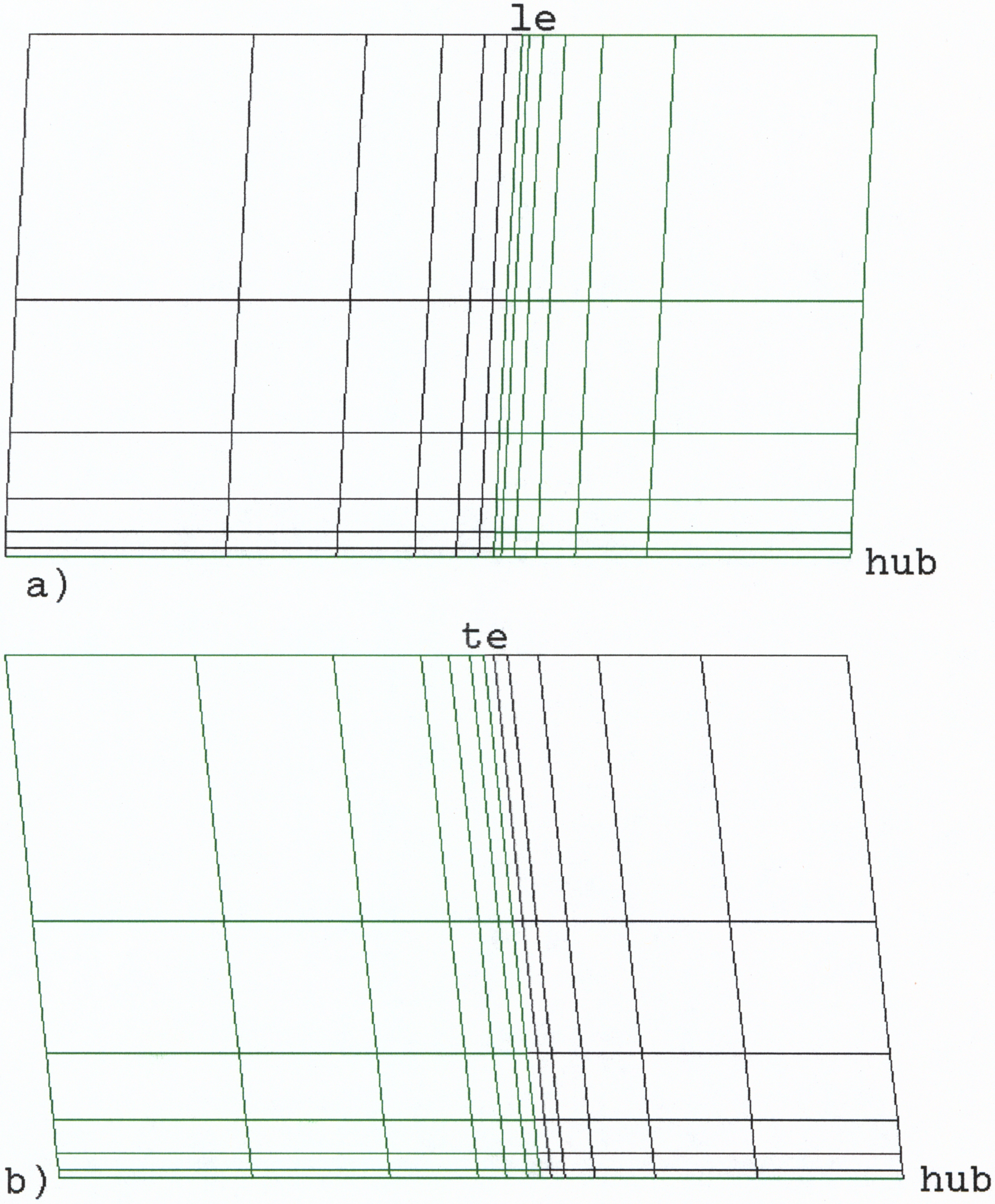

Figure 4.11 Blowups of a: Hub/Leading Edge and b: Hub/Trailing Edge Regions

5.0 Streaklines

A streakline is defined as the locus of particles which have earlier passed through a prescribed point (White, 1986). For steady flow, a streakline can be thought of as a line which is everywhere tangent to the velocity vector. A new option was created for the existing flow visualization program, PICTW, to display streaklines for flowfields calculated by MEFP.

5.1 Method for Finding Streaklines

5.1.1 Overview

The basic procedure for calculating streaklines is to start with a point in grid space. The velocity vector at this point is found by linearly interpolating the velocity vectors from the eight corners of the surrounding control volume to the point. Then the velocity vector is converted into the direction to travel in grid space coordinates, i, j, and k. The change in position vector is then incremented a calculated length through the control volume along the direction of travel. The process is repeated and the series of calculated points are connected by lines to form the streakline. The process will be described mathematically in three dimensions, but figures will be two dimensional for simplicity.

5.1.2 Determining the Direction of Travel

Consider a point, P, in x, y, and z coordinates as shown in Figure 5.1. The velocity at this point, $\mathbf{W}_P = (W_x, W_y, W_z)$, is calculated by linearly interpolating the velocity from each corner of the volume by,

$$\mathbf{W_P} = \begin{array}{l} \mathbf{W}_{i,j,k}(1-f_i)(1-f_j)(1-f_k) + \mathbf{W}_{i+1,j,k}(f_i)(1-f_j)(1-f_k) \\ + \mathbf{W}_{i+1,j+1,k}(f_i)(f_j)(1-f_k) + \mathbf{W}_{i+1,j+1,k+1}(f_i)(f_j)(f_k) \\ + \mathbf{W}_{i+1,j,k+1}(f_i)(1-f_j)(f_k) + \mathbf{W}_{i,j+1,k+1}(1-f_i)(f_j)(f_k) \\ + \mathbf{W}_{i,j+1,k}(1-f_i)(f_j)(1-f_k) + \mathbf{W}_{i,j,k+1}(1-f_i)(1-f_j)(f_k) \end{array} \qquad \textbf{(Eq. 5.1)}$$

The next step is to convert the velocity, $\mathbf{W}_P$, from x, y, z coordinates into a change in position vector using a small increment of time, δt.

$$\mathbf{W_P}\,\delta t = (\delta_x, \delta_y, \delta_z) \qquad \textbf{(Eq. 5.2)}$$

This vector then needs to be converted into a direction vector in grid space that can be seen in Figure 5.2.

$$\mathbf{D_P} = (\delta_i, \delta_j, \delta_k) \qquad \textbf{(Eq. 5.3)}$$

By the chain rule, δ_x, δ_y, and δ_z are expanded.

$$\begin{aligned} \delta_x &= \frac{\partial x}{\partial i}\delta_i + \frac{\partial x}{\partial j}\delta_j + \frac{\partial x}{\partial k}\delta_k \\ \delta_y &= \frac{\partial y}{\partial i}\delta_i + \frac{\partial y}{\partial j}\delta_j + \frac{\partial y}{\partial_k}\delta_k \\ \delta_z &= \frac{\partial z}{\partial i}\delta_i + \frac{\partial z}{\partial j}\delta_j + \frac{\partial z}{\partial k}\delta_k \end{aligned} \qquad \textbf{(Eq. 5.4)}$$

Equations 5.2, 5.3 and 5.4 can then be combined yielding

$$\mathbf{W_P}\,\delta t = \begin{bmatrix} \frac{\partial x}{\partial i} & \frac{\partial x}{\partial j} & \frac{\partial x}{\partial k} \\ \frac{\partial y}{\partial i} & \frac{\partial y}{\partial j} & \frac{\partial y}{\partial k} \\ \frac{\partial z}{\partial i} & \frac{\partial z}{\partial j} & \frac{\partial z}{\partial k} \end{bmatrix} \mathbf{D_P} \qquad \textbf{(Eq. 5.5)}$$

Equation 5.5 relates the velocity vector for point P in x-y-z coordinates to the direction vector for point P in i-j-k coordinates. The partial derivatives found in Eq. 5.5 are found by

$$\left.\frac{\partial x}{\partial i}\right]_{\text{at P}} = \frac{x_{i+1,j+f_j,k+f_k} - x_{i,j+f_j,k+f_k}}{(i+1)-1} \qquad \textbf{(Eq. 5.6)}$$

which is expanded to

$$\frac{\partial x}{\partial i} = \begin{aligned} & x_{i+1,j,k}(1-f_j)(1-f_k) + x_{i+1,j,k+1}(1-f_j)(f_k) \\ & + x_{i+1,j+1,k}(f_j)(1-f_k) + x_{i+1,j+1,k+1}(f_j)(f_k) \\ & - x_{i,j,k}(1-f_j)(1-f_k) - x_{i,j,k+1}(1-f_j)(f_k) \\ & - x_{i,j+1,k}(f_j)(1-f_k) - x_{i,j+1,k+1}(f_j)(f_k) \end{aligned} \qquad \textbf{(Eq. 5.7)}$$

The remaining partial derivatives, $\partial x/\partial j$, $\partial x/\partial k$, $\partial y/\partial i$, etc., may be found in a similar manner. Equation 5.5 can now be rewritten to solve for $\mathbf{D_P}$.

$$\mathbf{D}_{\mathbf{P}} = \begin{bmatrix} \delta_i \\ \delta_j \\ \delta_k \end{bmatrix} = \begin{bmatrix} \frac{\partial x}{\partial i} & \frac{\partial x}{\partial j} & \frac{\partial x}{\partial k} \\ \frac{\partial y}{\partial i} & \frac{\partial y}{\partial j} & \frac{\partial y}{\partial k} \\ \frac{\partial z}{\partial i} & \frac{\partial z}{\partial j} & \frac{\partial z}{\partial k} \end{bmatrix}^{-1} \mathbf{W}_{\mathbf{P}}\, \delta t \qquad \textbf{(Eq. 5.8)}$$

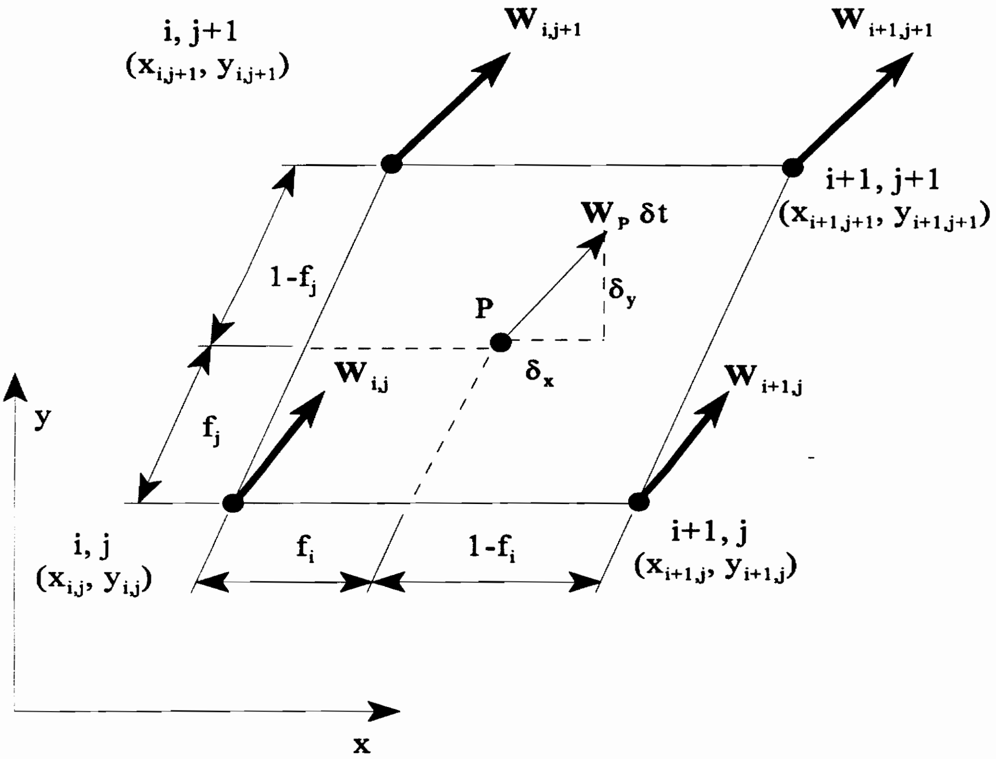

Figure 5.1 Velocity Interpolation for Streakline Point

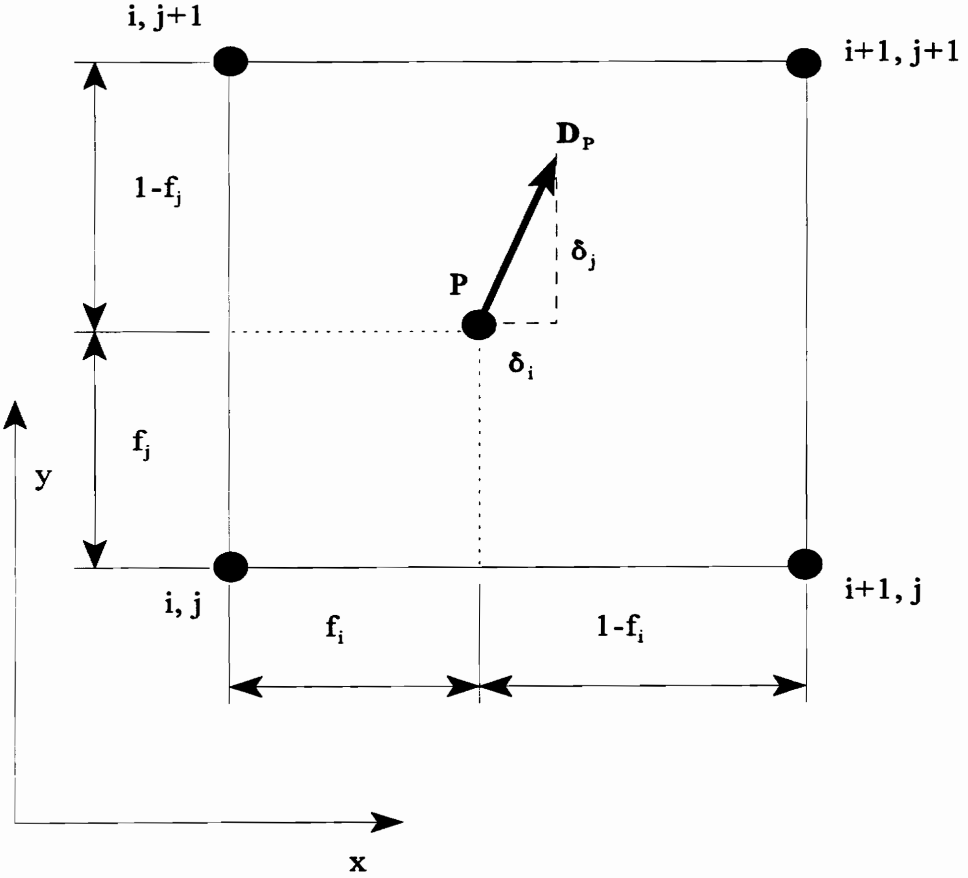

Figure 5.2 Streakline Direction Vector

5.1.3 Moving in the Calculated Direction

Figure 5.3a illustrates the first step in incrementing the streakline. The increment by which the streakline increases is set by the parameter, **Δ**. This is the maximum δ_i, δ_j, and δ_k to be used in the step distance across a grid cell. The corresponding limiting values for the new i, j, k locations are calculated by

$$\begin{aligned} L_i &= i + f_i + \Delta\frac{\delta_i}{|\delta_i|} \\ L_j &= j + f_j + \Delta\frac{\delta_j}{|\delta_j|} \\ L_k &= k + f_k + \Delta\frac{\delta_k}{|\delta_k|} \end{aligned} \qquad \textbf{(Eq. 5.9)}$$

Additional limitations placed on the limiting point are to stop the streakline just inside an adjacent control volume as shown in Figure 5.3b and defined by

$$\begin{aligned} i-0.005 &\le L_i \le i+1.005 \\ j-0.005 &\le L_j \le j+1.005 \\ k-0.005 &\le L_k \le k+1.005 \end{aligned} \qquad \textbf{(Eq. 5.10)}$$

The limiting point is then used to calculate the scaling factor to be applied to the direction vector, $\mathbf{D_P}$, when calculating the next position on the streakline.

$$F_{scale} = \min\left(\frac{L_i - P_i}{\delta_i}, \frac{L_j - P_j}{\delta_j}, \frac{L_k - P_k}{\delta_k}\right) \qquad \textbf{(Eq. 5.11)}$$

The next position on the streakline is found by

$$P_{new} = \begin{matrix} P_i + \delta_i (F_{scale}) \\ P_j + \delta_j (F_{scale}) \\ P_k + \delta_k (F_{scale}) \end{matrix} \qquad \textbf{(Eq. 5.12)}$$

A final check is made here for those points that crossed into a new cell. If the cell surface is a wall, the point is moved back normal to the wall in grid space so it is 1% of cell spacing from the wall. Figure 5.3c shows how this correction is made.

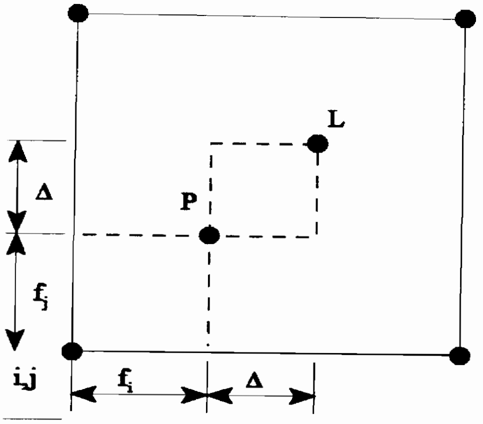

Figure 5.3a Point Location for D_p Scaling

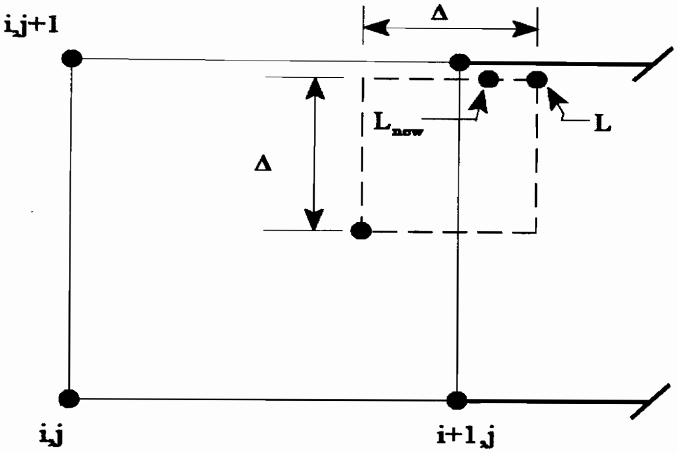

Figure 5.3b Adjustment of Limits for Entering Next Cell

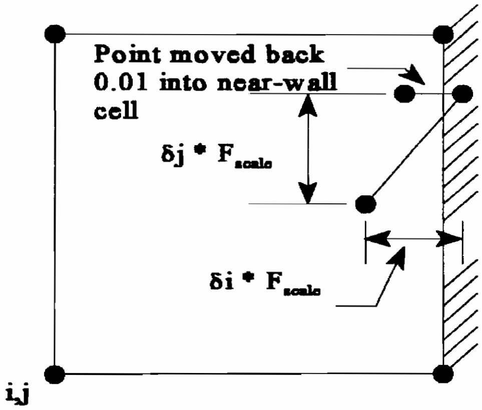

Figure 5.3c Wall Correction

Figure 5.3 Streakline Point Calculations

5.2 Examples/Options

5.2.1 Flow Around a Box

A simple test case of flow around a box was used to verify the streakline program was operating correctly. The grid contained 13 x 7 x 2 points with a rectangular box in the middle (Moore, 1994b). Figure 5.4 shows the grid with the calculated velocity vectors on the grid points. Eight streaklines were started along the inlet of the grid and can be seen in Figure 5.4. Streakline number 5 demonstates the wall check function. It hugs the wall until it reaches the side where it then carries on downstream. The top streakline, number 8, illustrates how streaklines cross the repeating boundaries.

5.2.2 Horseshoe Vortex in Flow around a Rankine Body

A more complex test case of flow around a Rankine half-body can be used to illustrate the streakline program as a three-dimensional viewing aid. A coarse 14x10x7 grid covers one fourth of the flow domain with symmetry planes on the centerline of the body and at mid-height. A horseshoe vortex is generated inviscidly using a velocity distribution at the inlet which follows the outer portion of the turbulent inlet boundary layer (Moore, 1994b). The grid and velocity vectors from this calculation are shown in Figure 5.5 with the formation of a horseshoe vortex visible in the velocity vectors at the endwall plane.

To aid in visualizing streaklines in 3-dimensions, color coded diamond tags are used whenever a streakline crosses an i, j, or k grid plane. The horseshoe vortex seen in Figure 5.5 was used to demonstrate the use of these tags and the use of streaklines for visualizing three-dimensional flow. Figure 5.6 is a three-dimensional view of the grid with five streaklines started at i=4.1 upstream of the horseshoe vortex and j=1.1 next to the symmetry plane. The black streakline was started at k=1.1, the red line at k=2.1, the blue line at k=3.1, the pink line at k=4.1, and the purple line at k=5.1. The color coding for the tags is red for crossing i-planes, blue for crossing j-planes, and green for crossing k-planes. To illustrate further how the colored tags work, two-dimensional views of an i-k plane and i-j plane were created. These two views are also shown in Figure 5.6

The streaklines as shown in these three figures clearly illustrate the horseshoe vortex phenomenon. The lowest or black streakline encounters the separation line preceding the vortex and flows out and around the Rankine body. The next streakline, in red, is pulled down toward the endwall and into the vortex before being swept out and around the body. The third, in blue, streakline is similar to the red streakline. It is pulled down and then out around the body by the vortex. The fourth streakline, in pink, is affected less by the vortex. It is pulled downwards but encounters the leading edge before it can be entrained into the vortex. It is then pulled downward as it is swept around the surface. The fifth streakline, in purple, is no longer influenced by the vortex except for a small downward migration in the leading-edge region. This streakline is seen to flow smoothly around the surface of the body as it continues downstream.

5.2.2.1 Limited Streaklines

Another option that can be used to study complex three-dimensional flows is limited streaklines. A limited streakline is one that is restricted to a particular plane in the flow. A special case of a limited streakline is a limiting streakline. This streakline is also restricted to a plane, but it is a near-wall plane that shows flow on a surface. These are very useful for studying secondary flows along surfaces and in passages. The method used to acquire limited streamlines is simply not to allow the streakline to travel in one of the grid directions by setting $\boldsymbol{\delta}_i$, $\boldsymbol{\delta}_j$, or $\boldsymbol{\delta}_k$ equal to zero. The secondary flow vectors were computed for the Rankine half body calculation to illustrate limited streaklines. Figure 5.7 shows the limited streaklines on the i=9 and 11 planes. The limited streakline on the i=9 plane clearly shows that the horseshoe vortex is dominating the secondary flows just downstream of the leading edge. The streakline is spiraling inward because the flow is accelerating through this region as the passage area decreases. The limited streaklines on the i=11 plane show that the horseshoe vortex is still present.

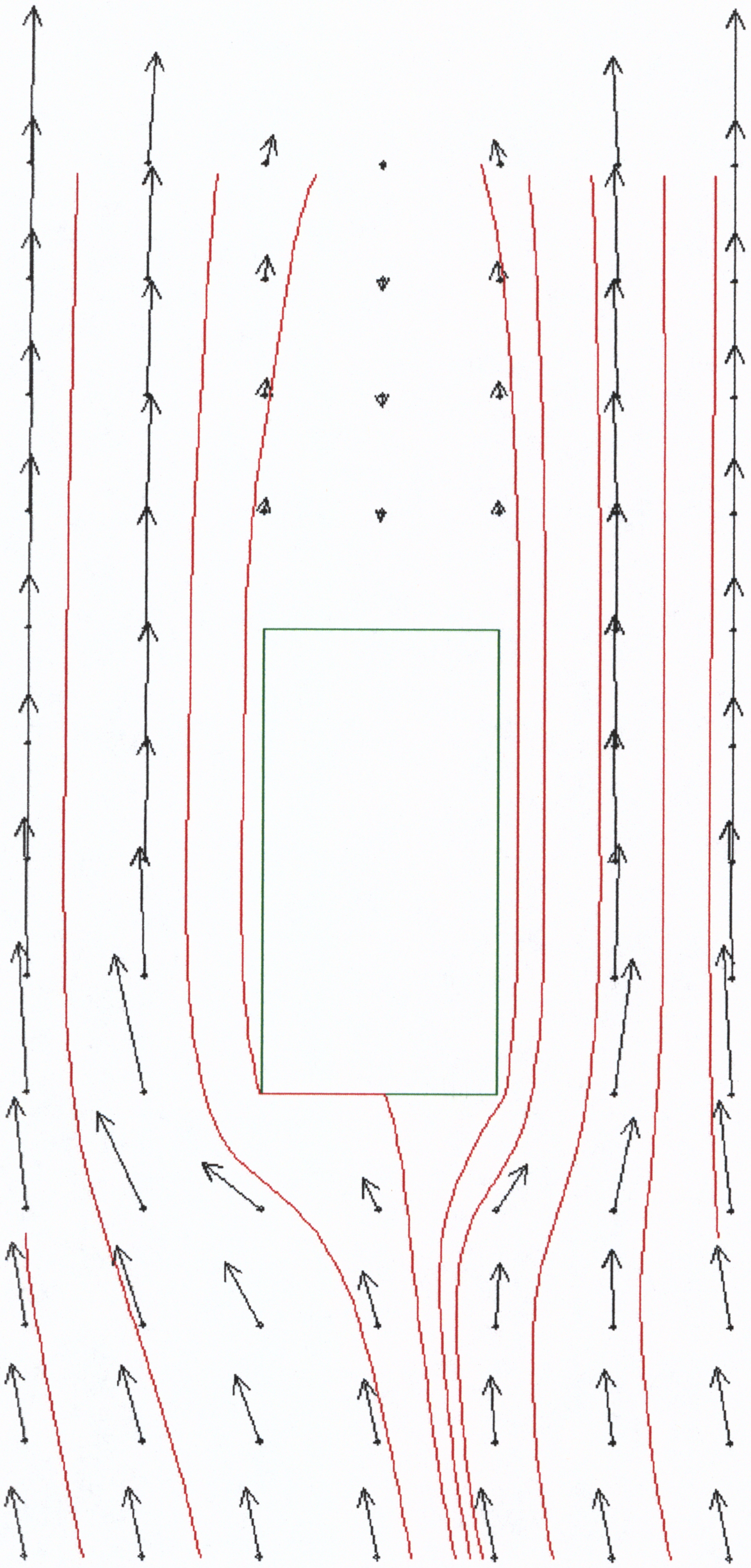

Figure 5.4 Streaklines Showing the Flow around a Box

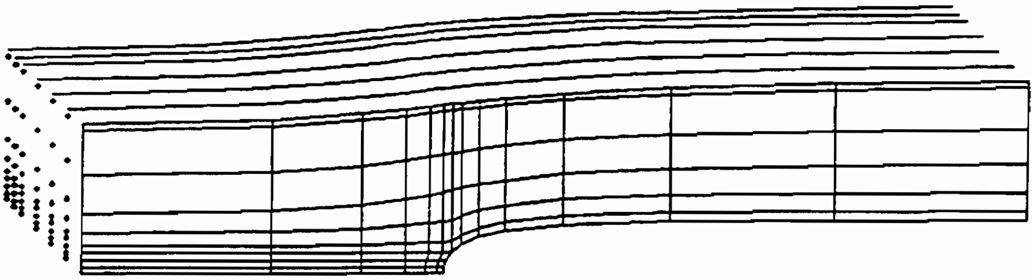

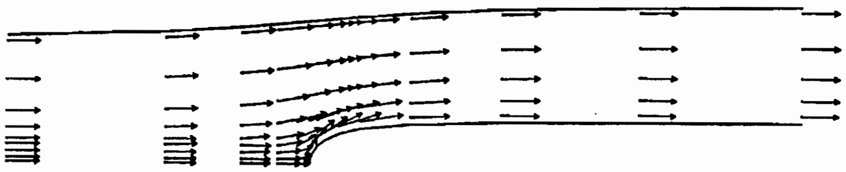

at k = 7, mid-height

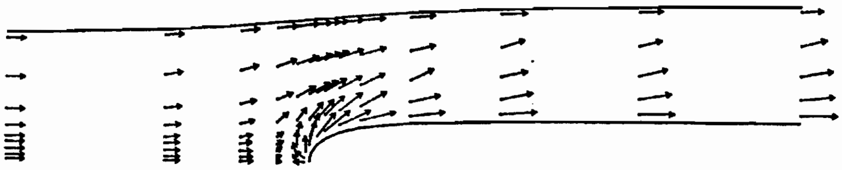

at k = 1, endwall

Figure 5.5 Grid and Velocity Vectors for Flow around a Rankine Half Body

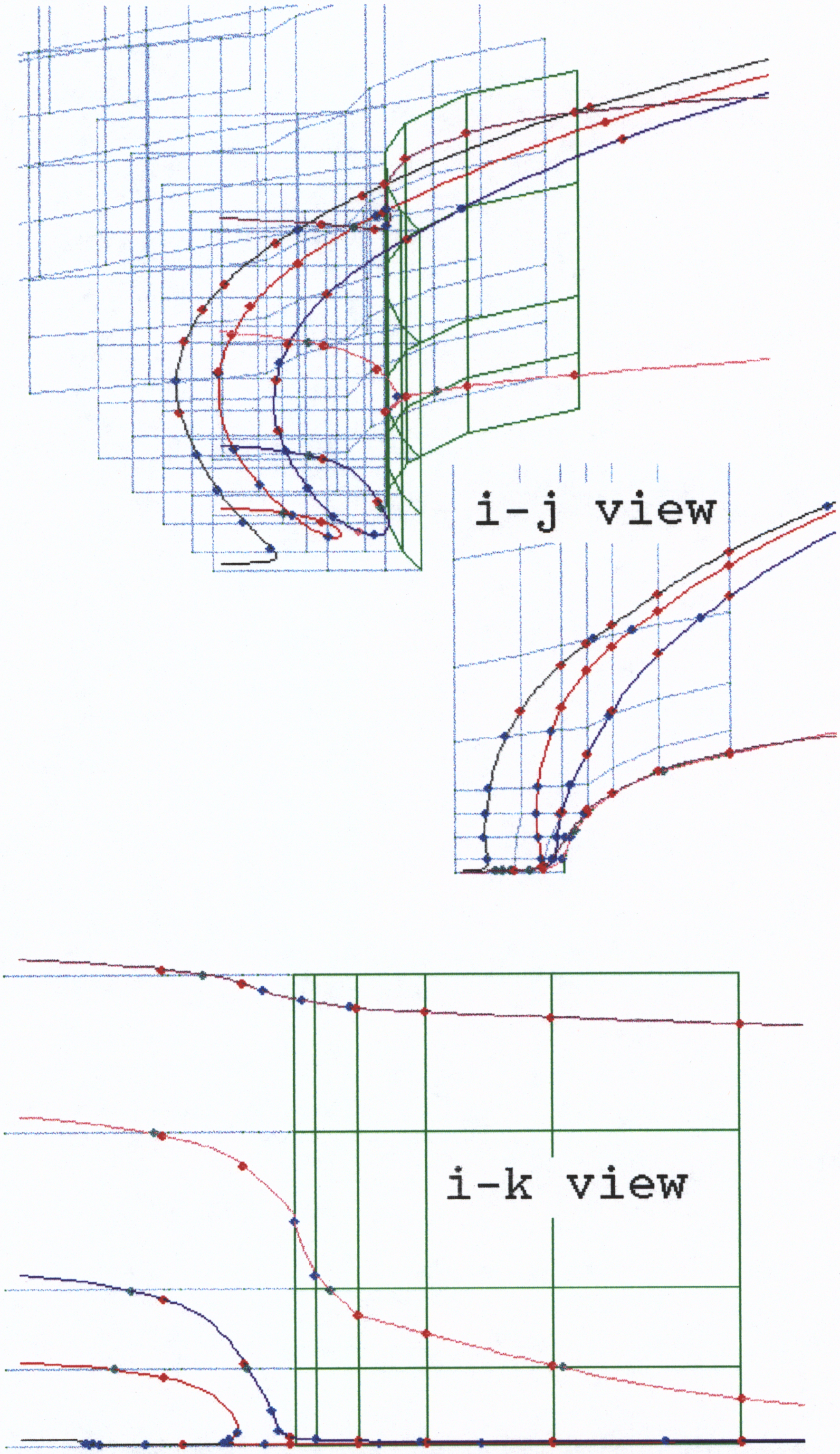

Figure 5.6 3-D Streaklines through Horseshoe Vortex, with i-k and i-j Views

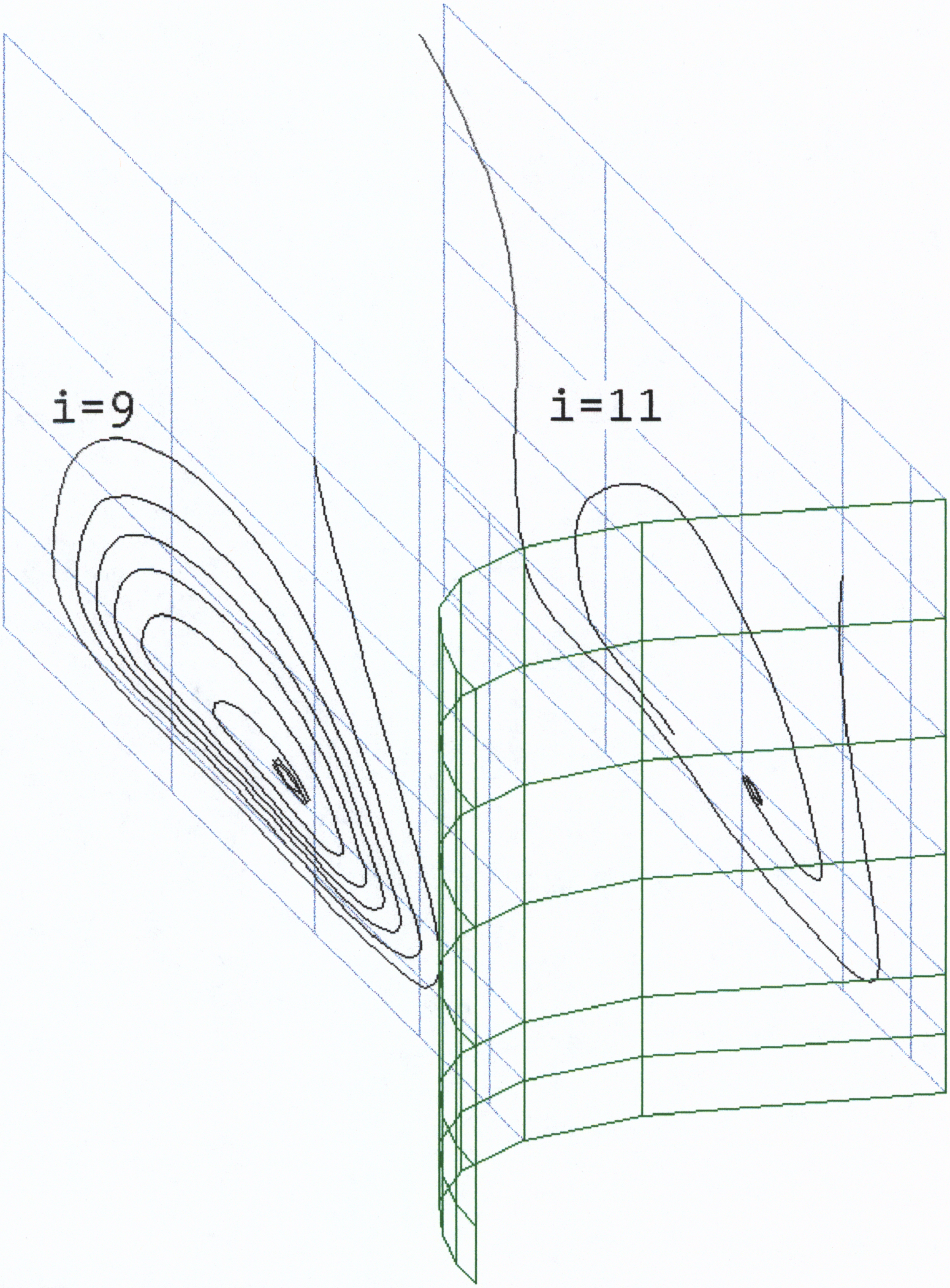

Figure 5.7 Limiting Streaklines Showing Secondary Flows

6.0 2-D Cascade Studies

6.1 NACA Comparison

A 2-D cascade calculation was set up to test the accuracy of the q-L transitional turbulence model with the new grid. The calculation was run on the 2-D grid section with a solidity of one shown in figure 4.8. A comparison is made with the experimental data generated in a cascade study using C4 blades reported in NACA Technical Note 3937 (Felix and Emery, 1959). The flow inlet angle, β_1, is 60 degrees for all the measurements.

The turning angle and section drag coefficient data used for comparisons from NACA Technical Note 3937 are shown in Figure 6.1. The incidence angle was varied by rotating the blades with the data being plotted versus the angle of attack. For the grid and inlet flow angle used in the calculation the angle of attack is approximately 15 degrees. The deviation angle instead of the turning angle will be used for the comparison. The section drag coefficient, c_D, is given by

$$c_D \equiv \frac{D}{\frac{1}{2}\rho V_{inlet}^2 c} \qquad \textbf{(Eq. 6.1)}$$

where c is the blade chord, and the drag, D, is given by

$$D = g(p_o - p_t)\cos\beta_m \qquad \textbf{(Eq. 6.2)}$$

Here g is the spacing and β_m is found by

$$\tan\beta_m = \frac{1}{2}(\tan\beta_1 + \tan\beta_2) \qquad \text{(Eq. 6.3)}$$

p_o is the inlet total pressure, and p_t is the downstream average total pressure. The calculated loss is outputted from MEFP as a total pressure loss, Cp_t, which is defined as

$$Cp_t = \frac{-(p_t - p_0)}{\frac{1}{2}\rho V_i^2} \qquad \text{(Eq. 6.4)}$$

c_D can be found from Cp_t by combining Eqs. 6.1-6.3.

$$\frac{D}{\frac{1}{2}\rho V_{inlet}^2} = g\,\frac{p_0 - p_t}{\frac{1}{2}\rho V_{inlet}^2}\cos\beta_m \qquad \text{(Eq. 6.5)}$$

$$c\,c_D = g\,Cp_t\cos\beta_m \qquad \text{(Eq. 6.6)}$$

$$c_D = Cp_t\,\frac{g}{c}\cos\beta_m \qquad \text{(Eq. 6.7)}$$

The incompressible flow calculation was run at an inlet Reynolds number of 233,000 and an inlet turbulence intensity of 0.4% corresponding to the NACA study. The turbulence intensity is defined as

$$Tu\% = \frac{1}{W}\sqrt{\frac{u^2 + v^2 + w^2}{3}} * 100 \qquad \text{(Eq. 6.8)}$$

Equation 6.8 can be combined with equation 3.13 to give the square root of the inlet turbulence kinetic energy, q

$$q = \frac{Tu\%}{100} W \sqrt{\frac{3}{2}} \qquad \textbf{(Eq. 6.9)}$$

The inlet conditions and the results of the calculation at 65% of an axial chord downstream of the trailing edge are summarized in Table 6.1.

The results are also compared with the experimental data in Figure 6.2. Figure 6.2a shows the calculated section drag coefficient compared with the experimental section drag coefficient. The calculated value as seen in the Figure 6.2a is in excellent agreement with the data. Figure 6.2b compares the calculated and actual deviation angle and it is seen that there is also excellent agreement between the two.

The calculated velocity vectors are shown in Figure 6.3, and the static pressure and total pressure loss contours are shown in Figure 6.4. Transition for this calculation occurs around 40% of chord on the suction surface. The y^+ values for the near-wall grid points range from 14 at the leading edge to a minimum of 2 around the transition region. The average value is approximately 8. The y^+ values are in the range of acceptable values as discussed in Section 4.2.2.

Table 6.1 Summary of NACA Calculation

Geometry:

$\beta_1' = 60.22°$ $\beta_2' = 30.14°$ $g / c = 1.0$

$c = 0.111$ m

Inlet: Re = 233,000

$V_{z1} = 17.51$ m/s $V_{y1} = -30.32$ m/s $\rho = 1.2$ kg/m^3

$V_i = 35.0$ m/s $\beta_1 = 60°$ $q = 0.172$ m/s

$L_{fre} = 0.0044$

Exit: Values calculated at $z/c_{ax} = 1.65$

$\overline{V}_{z2} = \overline{V}_{z1} = 17.51\text{m/s}$ $\overline{\overline{V}}_{y2} = -15.599\text{m/s}$

$p_o - \overline{\overline{p}}_t = 15.37\ \text{N/m}^2$ $Cp_t = 0.0209$

$$\beta_2 = \tan^{-1}\left(\frac{\overline{\overline{V}}_{y2}}{\overline{V}_{z2}}\right) = 41.697°$$ $\beta_m = 52.67°$

$c_D = 0.013$ $\delta = 11.56°$

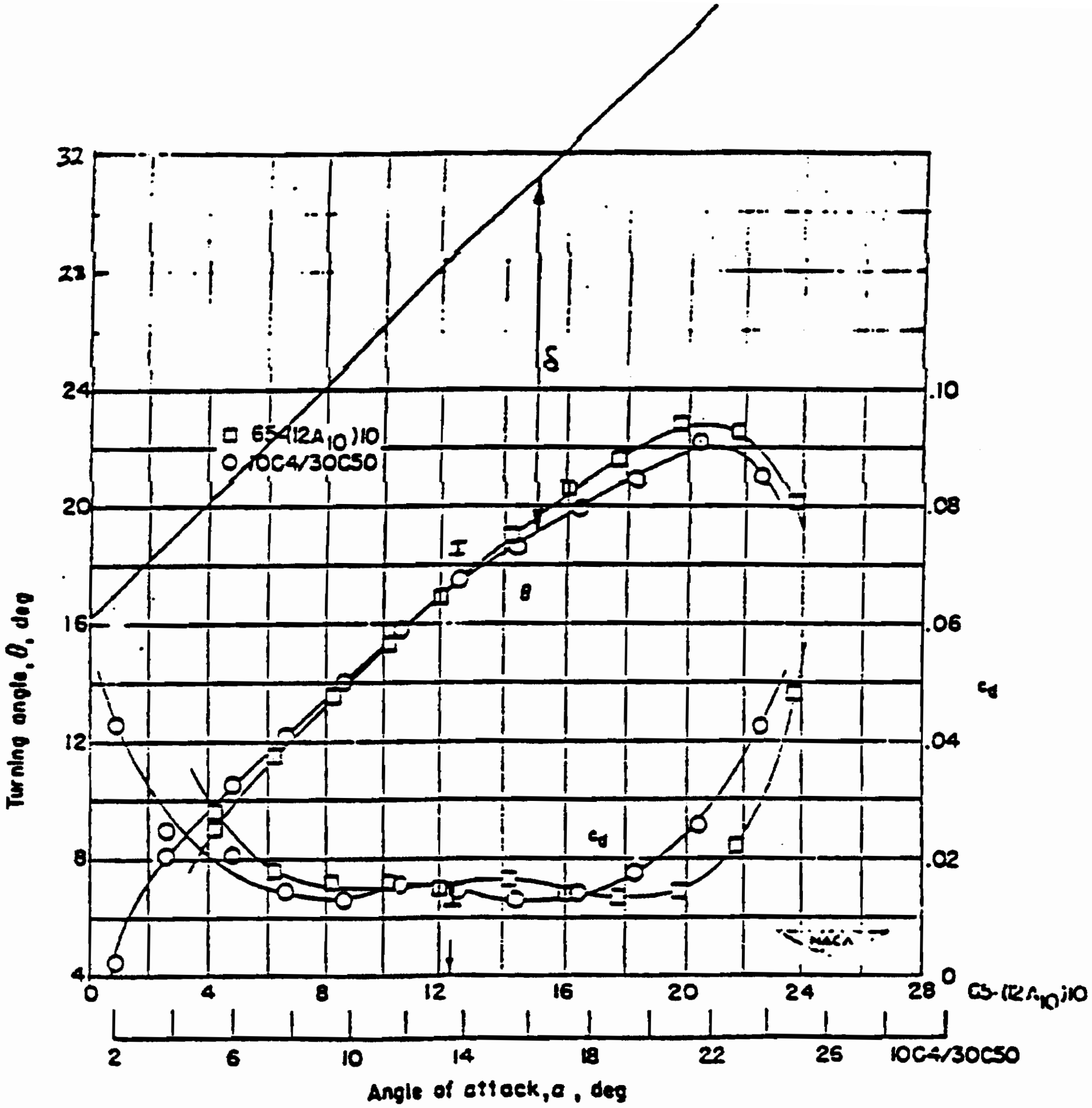

Comparison of the section characteristics of the NGTE 10C4/30C50 sections at $\beta_1 = 60°$. Arrow indicates design angle of attack.

Figure 6.1 NACA Technical Report 3937 Cascade Test Data (Felix and Emery, 1959)

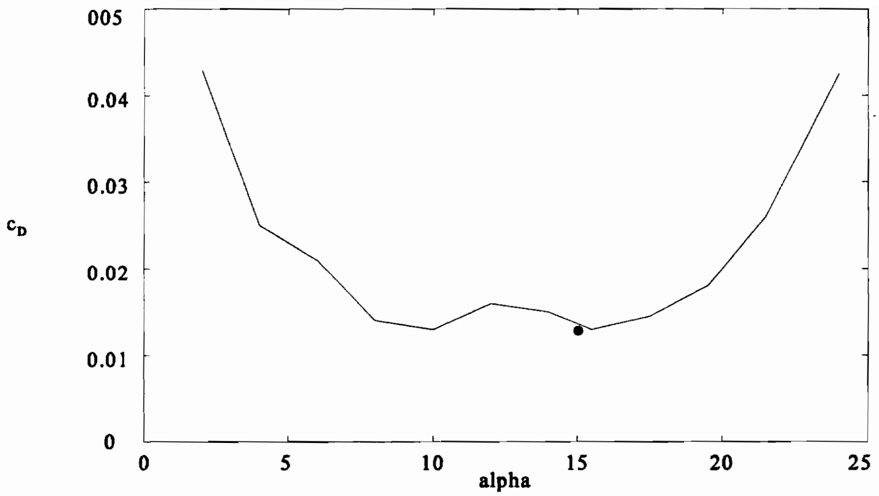

Figure 6.2a Drag Coefficient vs. Angle of Attack

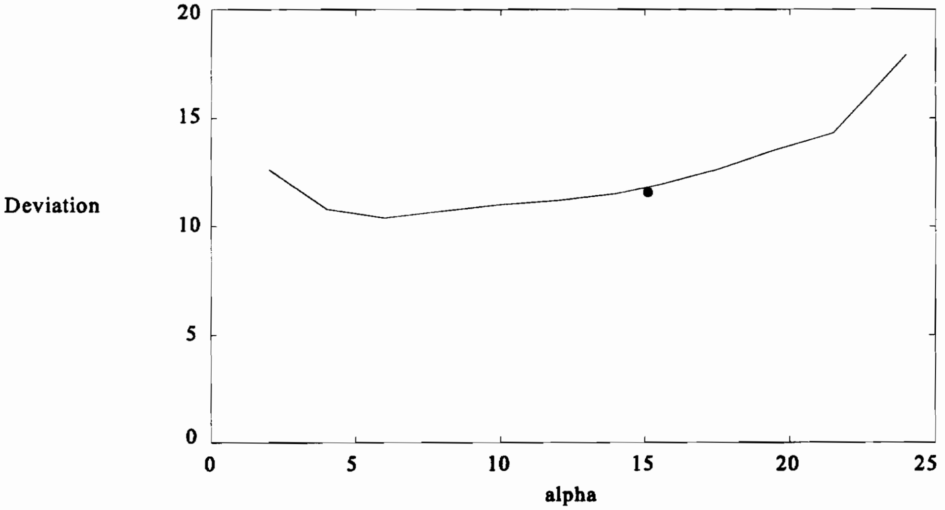

Figure 6.2b Deviation vs. Angle of Attack

Figure 6.2 Comparison with NACA Cascade Data

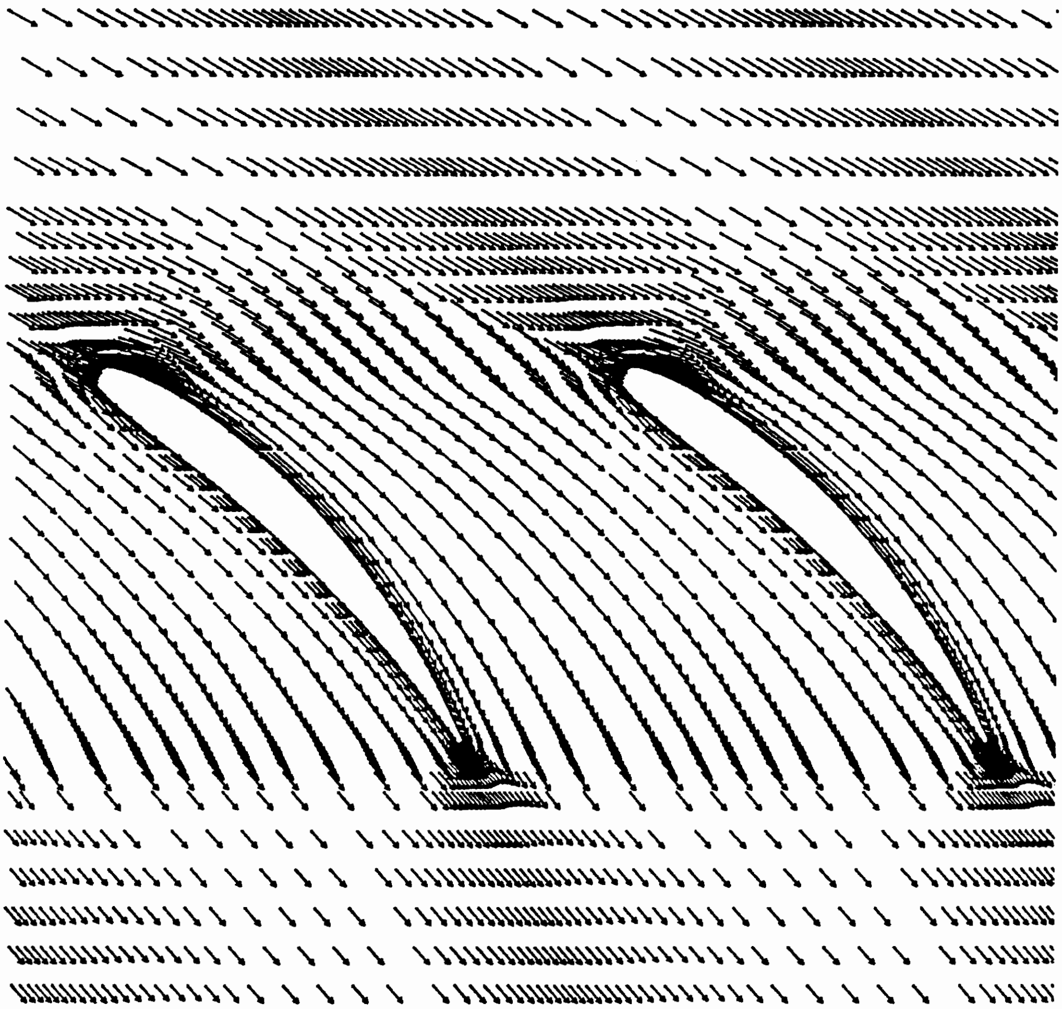

Figure 6.3 Calculated Velocity Vectors for NACA Comparison Calculation

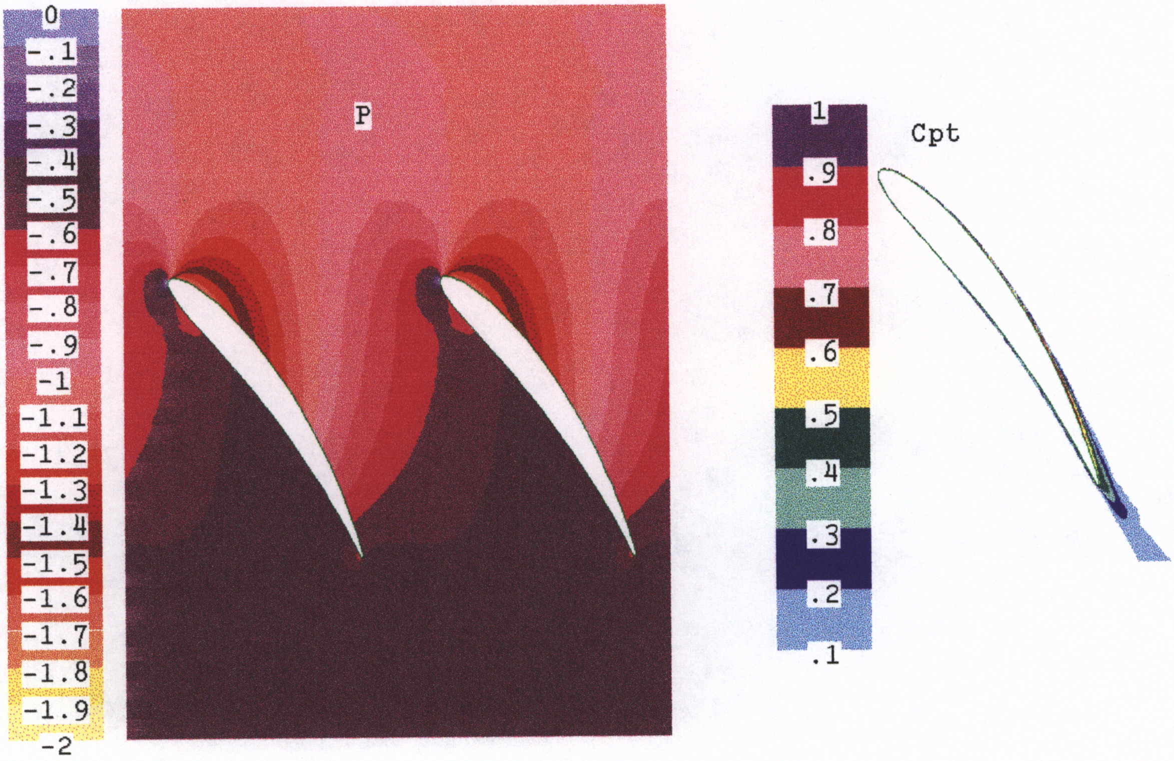

Figure 6.4 Static Pressure and Total Pressure Loss Contours for NACA Comparison Calculation

6.2 Transition Studies

The next two sections describe a series of cascade calculations studying how varying the turbulence intensity and incidence angle affects the location of transition from a laminar to a turbulent boundary layer and then possibly to turbulent separation. All of the calculations used the q-L transitional turbulence model and were run on the 2-D section of the 3-D grid shown in Figure 4.9. The results of the incompressible flow calculations will be compared qualitatively to the turbulence intensity and incidence angle studies described in Sections 2.3.1 and 2.3.2. Quantitative comparisons cannot be made due to the different blade profiles between the studies and the present study.

Transition location data is plotted as start of transition and end of transition based upon the q-L model's method of determining transition, F_{tu}. F_{tu} ranges from 0 where the boundary layer is laminar, to 1 being fully turbulent. A F_{tu} value of 0.1 is considered the start of transition and a value of 0.9 is considered the end of transition. The flow has a laminar separation bubble if backflow exists in the transition region. Similarly, the flow undergoes a turbulent separation if backflow develops in the turbulent boundary layer.

6.2.1 The Effects of Turbulence Level on Transition

To study the effects of free stream turbulence level on transition a series of eight calculations were run at the following turbulence intensity levels: 0.4, 1, 2, 3, 4, 5, 6, and 10%. The inlet flow angle, β_1, is equal to 60 degrees for all of the calculations. This is the same as used for the NACA calculation and corresponds to near zero incidence. The Reynolds number used was 233,000, again the same as for the NACA comparison calculation. The inlet conditions and the results of the calculations are summarized in Table 6.2. The results are plotted in Figure 6.5 which shows the transition data and Figure 6.6 which shows the total pressure loss and turning angle data for the calculations.

The start and end of transition on the suction surface as a function of axial chord is plotted in Figure 6.5 for each turbulence intensity calculation. The most notable difference between this figure and Figure 2.9 is the lack of a critical turbulence intensity after which transition occurs at the leading edge. However, there is a shift in the start of transition toward the leading edge from 50% to 20% of axial chord as the turbulence intensity increases. Laminar separation bubbles exist for flows with turbulence intensity values of 0.4, 1, and 2% that coincide well with the bubbles seen in Figure 2.9. The minimum pressure location for these calculations occurs at 0.054 of axial chord. The freestream velocity ratio, V_{sep}/V_{max}, based on local static and inlet total pressures for the laminar separation bubbles at 0.4, 1, and 2% turbulence intensities are 0.83, 0.66, and 0.62 respectively.

Figure 6.6a shows the total pressure loss data as a function of turbulence intensity. When comparing this with the similar plot in Figure 2.9, there is good agreement in the overall trend of losses. The loss starts at a value of 0.0178 for a turbulence intensity of 0.4%, then declines to around 0.0135 for turbulence intensities of 1 and 2%. It then slowly climbs to a value of 0.0208 at 10% turbulence intensity. While the transition data does not show a critical turbulence intensity, if the loss data is interpreted similarly to that in Figure 2.9, it suggests there is a critical turbulence intensity somewhere between 1 and 2%. Finally, it is not known whether the losses will level off at higher turbulence levels in a similar manner to that seen in Figure 2.9.

Figure 6.6b shows the turning angle data as a function of turbulence intensity. There is no qualitative agreement between the calculations and the experimental data. The angle variation is insignificant in that it varies by only 0.41 degrees and does not level off as seen in Figure 2.9. In conclusion, while a critical turbulence intensity value was not observed, there are qualitative similarities between the two studies. The location of transition moves closer to the leading edge as turbulence intensity is increased and the predicted total pressure losses are qualitatively similar to those seen with the different experimental configuration of Schlichting and Das (1970).

Table 6.2 Summary of Turbulence Intensity Cascade Calculations

Geometry:

$\beta_1' = 60.22°$ $\beta_2' = 30.14°$ $c = .111$

Inlet: Re = 233,000

$V_{z1} = 17.51$ m/s $V_{y1} = -30.32$ m/s $\rho = 1.2$ kg/m^3

$V_i = 35.0$ m/s $\beta_1 = 60°$ $L_{fre} = 0.0044$

Exit: Values calculated at $z/c_{ax} = 1.65$ and Transition Location as a Fraction of c_{ax}

$V_{z2} = V_{z1} = 17.51$ m/s (area averaged)

Tu%	V_{y2} m/s (mass avg.)	β_2°	Start of Transition	End of Transition	C_{pt}
0.04	-14.97	40.48	0.466	0.687	0.01778
1	-14.94	40.43	0.5798	0.6818	0.01354
2	-14.94	40.43	0.4617	0.6631	0.01382
3	-14.79	40.13	0.457	0.6798	0.01467
4	-14.76	40.07	0.429	0.667	0.01579
5	-14.77	40.09	0.3681	0.6659	0.0167
6	-14.80	40.16	0.2963	0.6516	0.01764
10	-14.90	40.33	0.1739	0.6109	0.0208

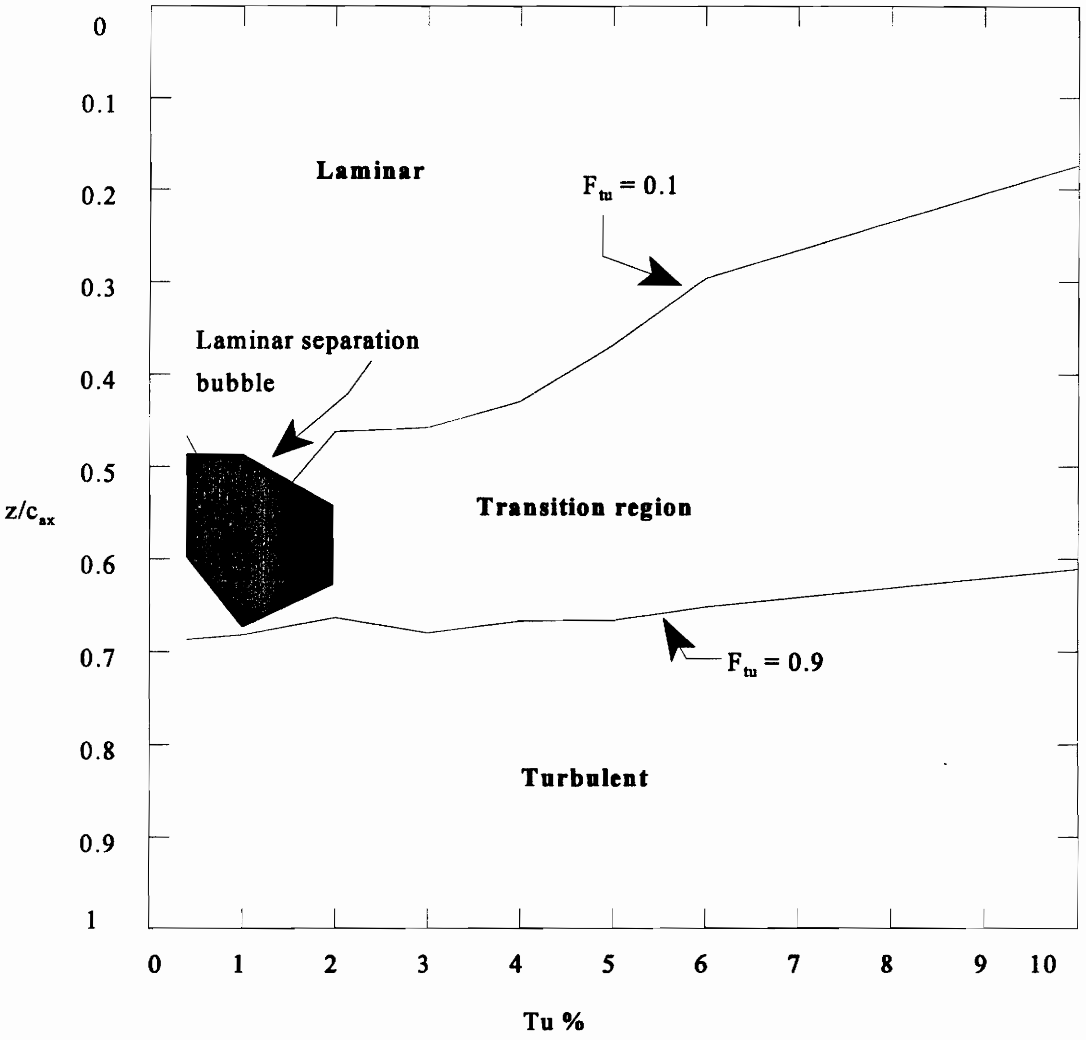

Figure 6.5 Transition vs. Tu %

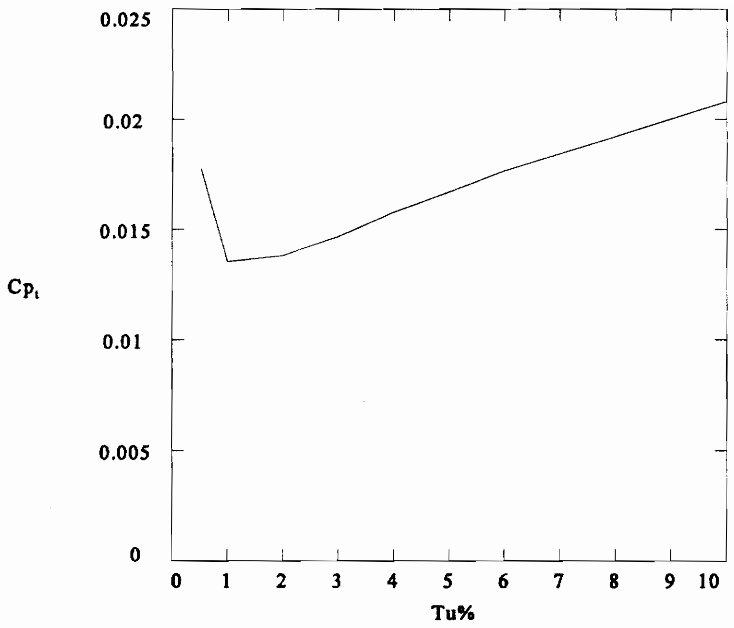

Figure 6.6a Total Pressure Loss vs. Tu%

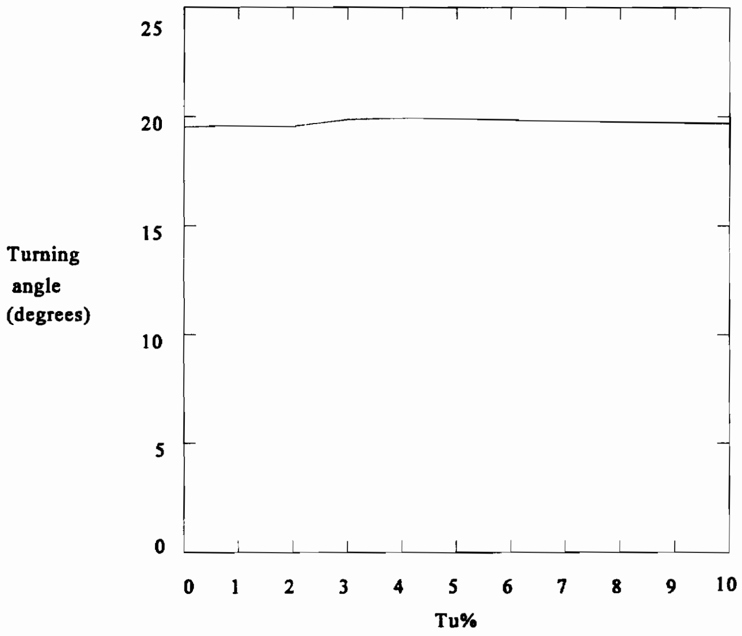

Figure 6.6b Turning Angle vs. Tu%

Figure 6.6 Total Pressure Loss and Turning Angle vs. Tu %

6.2.2 The Effects of Incidence Angle on Transition

Eleven calculations were run to study the effects of incidence angles on the location of transition and turbulent separation. The range of incidence angles was from -15 to 15 degrees in 3 degree increments. The inlet Reynolds number and the turbulence intensity were chosen to correspond to the Deverson rotor. The incidence angle was obtained by adjusting the W_y and W_z components of the inlet velocity keeping the magnitude of the velocity unchanged at 45.05 m/s. The turbulence intensity was set at 2%. The free stream turbulence intensity, Tu, measured in the Deverson rotor was approximately 4% and was found by

$$Tu = \frac{\sqrt{V'^2}}{V_{ax}} \qquad \textbf{(Eq. 6.10)}$$

The Tu value of 2% was obtained by converting Tu to the relative frame,

$$Tu = \frac{\sqrt{V'^2}}{V_{ax}}\left(\frac{V_{ax}}{\sqrt{W_{ax}^2 + W_\theta^2}}\right) \qquad \textbf{(Eq. 6.11)}$$

With an inlet angle of 60 degrees, the turbulence intensity is reduced by a factor of two yielding 2%.

The location of transition was found by the F_{tu} correlation and predicted by Thwaites method for approximating a laminar boundary layer using the computed pressure (Thwaites, 1949). The next section discusses Thwaites method and its implementation followed by a discussion of the results.

6.2.2.1 Thwaites Method

Thwaites method for determining the location of transition uses a correlation between a momentum thickness based Reynolds number and a pressure gradient parameter shown in Figure 6.7. Starting at the stagnation point, the momentum thickness, θ, is found by integrating the local potential flow velocity around the blade surface

$$\theta^2 = 0.45\, W^{-6} \nu \int_0^s W^5 ds \qquad \textbf{(Eq. 6.12)}$$

where s is the distance along the blade surface from the stagnation point. With the calculation being steady and incompressible, the velocity is found by

$$W = \sqrt{\frac{2(p_t - p)}{\rho}} \qquad \textbf{(Eq. 6.13)}$$

The pressure gradient parameter, m, is found by

$$m = -\frac{dW}{ds}\frac{\theta^2}{\nu} \qquad \textbf{(Eq. 6.14)}$$

Using Bernoulli's equation, the change in velocity can be rewritten in terms of the change in pressure.

$$p_t = p + \frac{1}{2}\rho W^2 = \text{constant} \qquad \textbf{(Eq. 6.15)}$$

$$\frac{dp}{ds} + \rho W \frac{dW}{ds} = 0 \qquad \textbf{(Eq. 6.16)}$$

$$m = \frac{\theta^2}{\nu \rho W}\left(\frac{dp}{ds}\right) \qquad \textbf{(Eq. 6.17)}$$

The Reynolds number based on the momentum thickness is then found.

$$Re_\theta = \frac{w\theta}{\nu} \qquad \textbf{(Eq. 6.18)}$$

The pressure gradient parameter, m, and the momentum thickness Reynolds number are then plotted for each blade grid point from the stagnation point and compared with Figure 6.7. If the value of m becomes larger than 0.082 before surpassing the value of Re_θ corresponding to the line of constant turbulence intensity for the flow, it has undergone transition via a laminar separation bubble. If the value of Re_θ crosses the line of constant turbulence intensity corresponding to the flow before m is larger than 0.082, the flow undergoes a simple transition to a turbulent boundary layer.

6.2.2.2 Incidence Angle Calculation Results

The inlet data and the results for the variable incidence angle calculations are summarized in Table 6.3. Figure 6.8 illustrates how Thwaites method was used to determine the transition location and transition method. Plotted is the pressure gradient parameter, m, versus the momentum thickness based Reynolds number, Re_θ, for the incidence angle case of 15 degrees. The values begin with negative values of m as the flow accelerates from stagnation, and move up and to the left. The value of m reaches 0.082 before Re_θ reaches a value of 400 which would indicate transition to a turbulent boundary layer for a 2% free stream turbulence level. Therefore, transition occurs via a laminar separation bubble. The remaining plots for the incidence angle calculations are similar to this plot and the summarized results can be seen in Table 6.3 and Figure 6.10.

The start of transition predicted by the F_{tu} values begins around 0.7 of axial chord for an incidence angle of -15 degrees and moves to around 0.1 for an incidence of 15 degrees as seen in Figure 6.9. Comparing this with the transition plot in Figure 2.9, there is qualitative similarity in the general shape of the curve produced by the F_{tu} data points. The movement of transition toward the leading edge in the positive range of incidences occurs more gradually than seen in Figure 2.9, with the shift toward the leading edge beginning approximately 6 degrees earlier around -6 degrees of incidence. A laminar separation bubble does exist for incidence angles of -15 to -9 degrees, but does not extend through the whole range of negative incidence angles as shown in Figure 2.9.

Turbulent separation begins at 6 degrees of incidence and by 15 degrees it has moved to 50% of the axial chord. This is in good agreement with what is seen in Figure 2.9. The fact that turbulent separation is predicted around 9 degrees of incidence is of particular interest since the hub region of the Deverson rotor experiences an incidence angle up to 9 degrees.

The predictions based on Thwaites method have a similar qualitative agreement. The curve through the Thwaites method results is very similar to that produced by F_{tu} but with transition occurring an average of 15% of chord closer to the leading edge.
A major difference between the predictions based on Thwaites method and the F_{tu} predictions or Figure 2.9 is that transition occurs only by a laminar separation bubble.

The calculated total pressure losses are shown in Figure 6.10a. There is good qualitative agreement with the loss data in Figure 2.9. The lowest losses occur at design incidence, with losses increasing away from this point. The highest calculated loss occurred at 15 degrees incidence. The deviation angle for each calculation is shown in Figure 6.10b. While no comparison can be made with this plot, it is important in understanding the flow for the Deverson rotor. It is seen in Figure 6.10b that the deviation angles increase significantly after an incidence of 6 degrees which coincides with the start of turbulent separation. This behavior is similar to the flow behavior in the hub region of the Deverson rotor.

The normalized static pressures found by

$$P = \frac{p - p_t}{\frac{1}{2}\rho V_{inlet}^{2}} \qquad \textbf{(Eq. 6.19)}$$

are shown in Figure 6.11. The pressure is plotted from the stagnation point on the leading edge to the end of the suction surface. The bottom line corresponds to the calculation of -15 degrees incidence with each successive line above that decreasing in incidence by 3 degrees. Note that the minimum static pressure for an incidence of -15 degrees occurs at approximately 40% of axial chord, with the location of the minimum moving toward the leading edge as the incidence is increased. This corresponds to the location of the boundary layer transition moving toward the leading edge. This plot also illustrates the mechanism for three-dimensional radial relief discussed in Section 2.1.1.1. As the incidence angle is increased, the static pressure in the leading edge region decreases, creating a steep gradient in the radially inward direction. In three-dimensional flow, this induces the radially inward flow which in turn decreases the leading edge loading in the hub region.

Figure 6.12 shows the velocity vectors through the cascade for an incidence of 9 degrees. Transition for this case occurred at 13% of axial chord and turbulent separation occurred at 84%. Figure 6.13a contains the static pressure contours for the same case. It illustrates that the stagnation point on the leading edge has moved around to the pressure side. Figure 6.13b shows the total pressure loss contours, Cp_t. The contours begin to thicken where transition occurs on the suction surface and show the wake extending downstream.

Figure 6.14 shows the streaklines in and around the separated region of flow for the case of 9 degrees incidence. The streakline that closest to the suction surface begins to be convected away before it is entrained in the backflow where it ends at the stagnation point. The next streakline away from the surface is similarly pulled into the backflow where it becomes caught up by the vorticity within the backflow. The third streakline from the suction surface convects around the small region of backflow and is turned through a large angle around the trailing edge before it is forced downstream by the much stronger flow coming from the pressure surface. The remaining streaklines show how the flows from each side of the blade come together. It is quite apparent that the pressure surface side is the dominant flow when they meet.

In conclusion, the results from the incidence angle calculations are qualitatively similar to the experimental cascade incidence studies. The location of transition shifts from around 70% of axial chord and moves toward the leading edge. With high negative incidence angles, the flow undergoes transition via a laminar separation bubble. With incidence angles greater than 6 degrees, turbulent separation of the boundary layer occurs. The total loss profile over the range of incidence angles is also very similar. These results including the deviation angle data show that the q-L transitional turbulence model can predict trends in flow phenomena in the hub region of the Deverson rotor, if the flow were to behave two-dimensionally.

Table 6.3 Summary of 2-D Incidence Angle Cascade Calculations

Geometry:

$\beta_1' = 60.22$ $\beta_2' = 30.14°$ $c = .111$

Inlet:

$\rho = 1.2$ kg/m^3 $V_i = 45.05$ m/s $q = 1.1045$ $L_{fre} = 0.0044$

β_1°	incidence angle°	V_{z1} m/s area avg.	V_{y1} m/s area avg.
45	-15	32.0	-31.76
48	-12	33.62	-30.40
51	-9	35.16	-28.24
54	-6	36.59	-26.36
57	-3	37.92	-24.41
60	0	39.15	-22.39
63	3	40.23	-20.32
66	6	41.25	-18.18
69	9	42.16	-16.0
72	12	42.93	-13.77
75	15	43.59	-11.55

Exit: Values calculated at $z/c_{ax} = 1.65$ and Transition values as a Fraction of c_{ax}

i°	Transition by Thwaites	Start of Transition by F_{tu}	End of Transition by F_{tu}	Turbulent Separation	Cp_t	Deviation
15	0.46	0.6554	0.6916	none	0.03556	8.35
12	0.557	0.6043	0.646	none	0.03008	8.54
9	0.52	0.6042	0.646	none	0.02562	8.8
6	0.45	0.64	0.726	none	0.02206	9.14
3	0.424	0.5479	0.6452	none	0.02118	9.88
0	0.22	0.4913	0.5972	none	0.02024	10.25
-3	0.141	0.4308	0.5363	none	0.02210	10.69
-6	0.0	0.2	0.2519	0.986	0.02691	11.45
-9	0.0	0.1343	0.1875	0.8423	0.03518	12.56
-12	0.0	0.1342	0.1875	0.7512	0.05128	14.4
-15	0.0	0.0813	0.1229	0.4584	0.0948	19.34

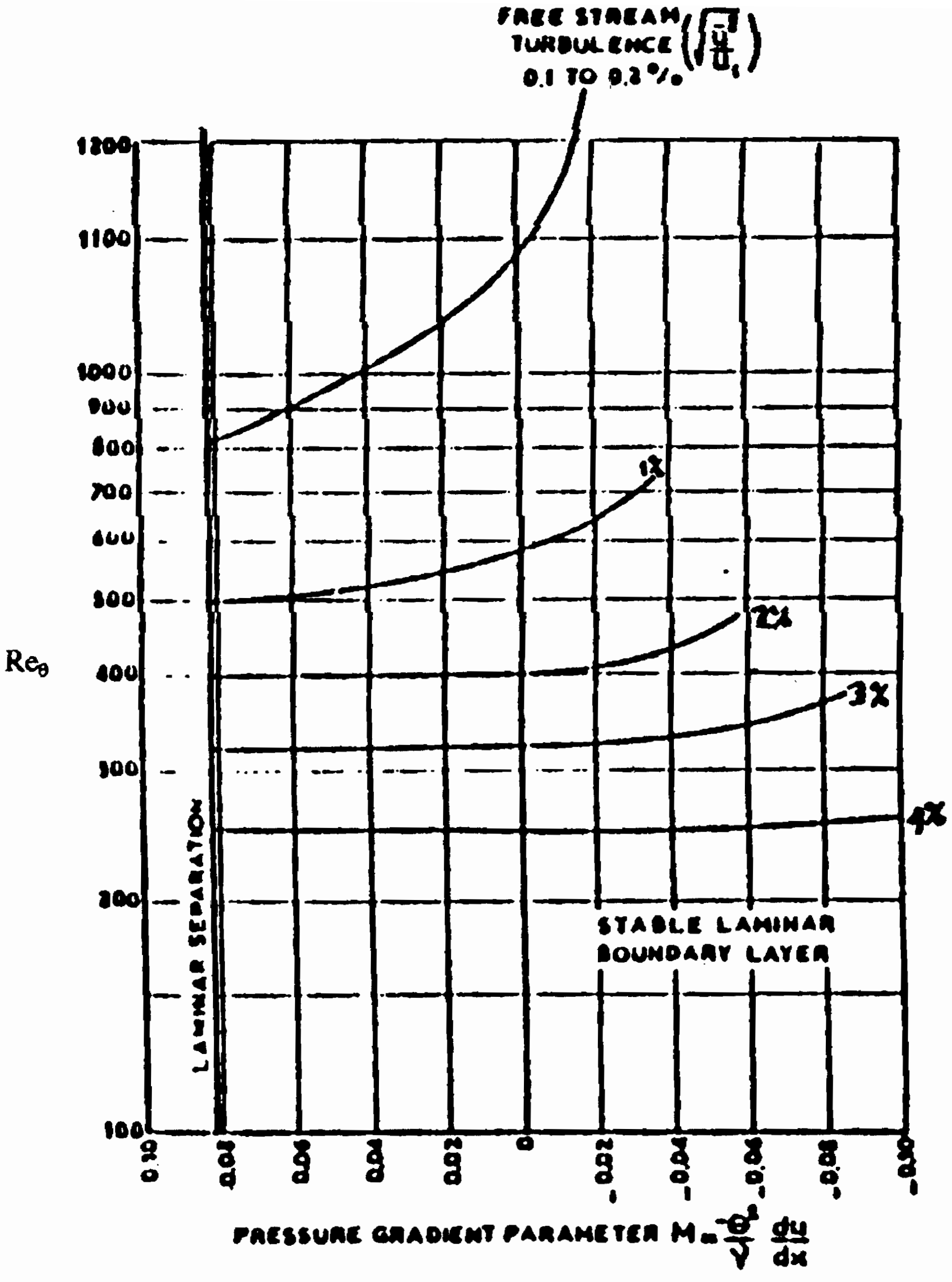

Figure 6.7 Re$_\theta$ vs m: Transition method correlation (Seyb, 1971)

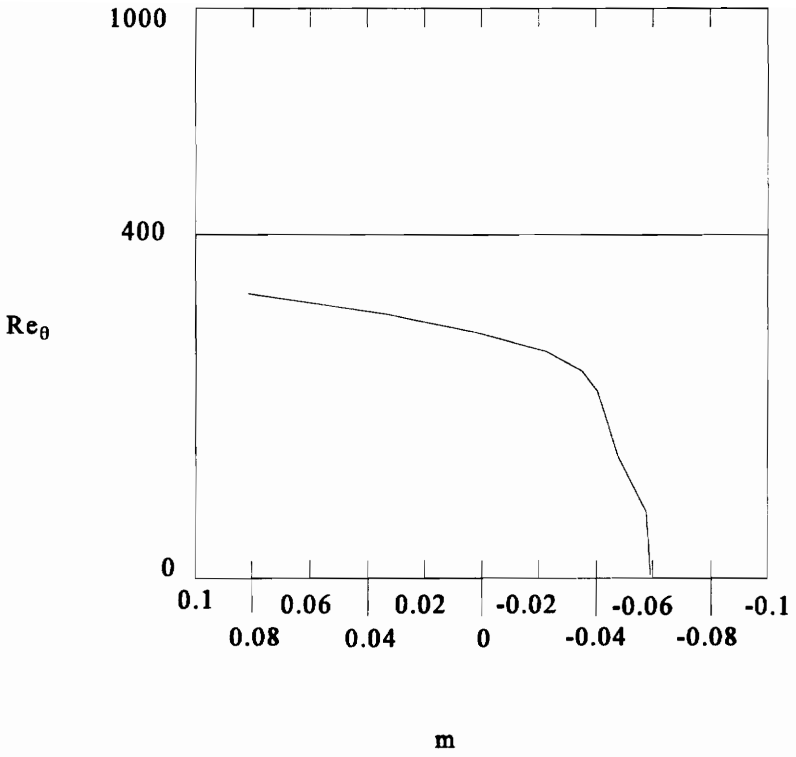

Figure 6.8 m vs Re$_\theta$ for incidence = -15 degrees

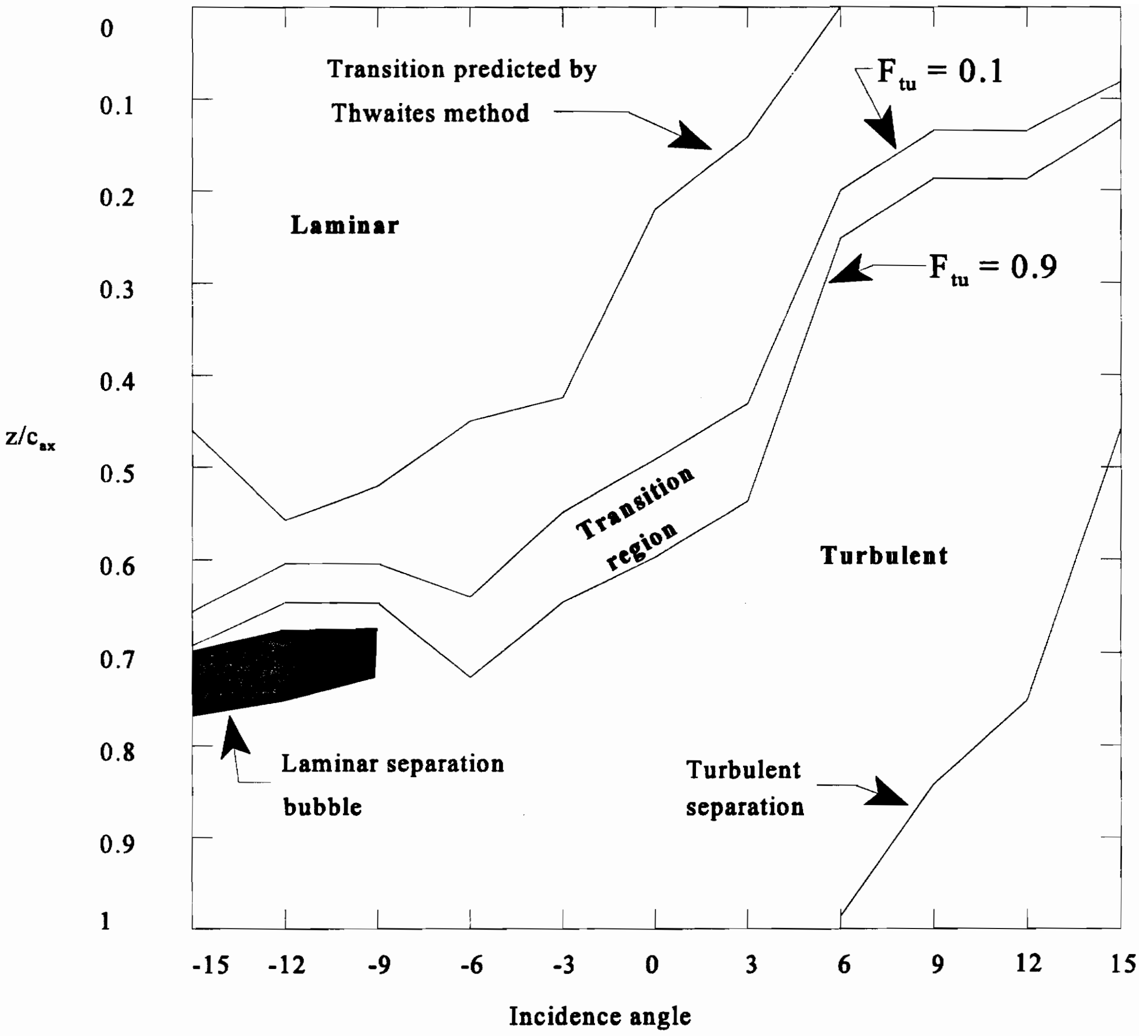

Figure 6.9 Transition and Separation vs. Incidence Angle

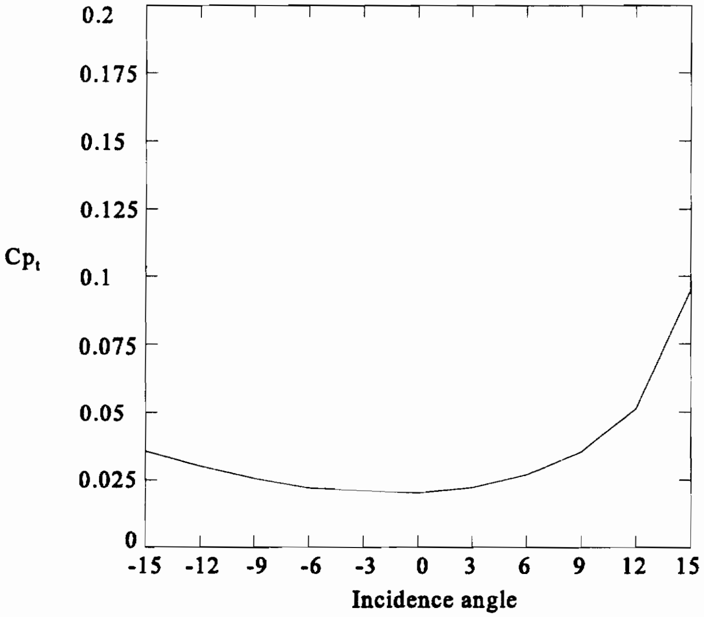

Figure 6.10a Total Pressure Loss vs. Incidence Angle

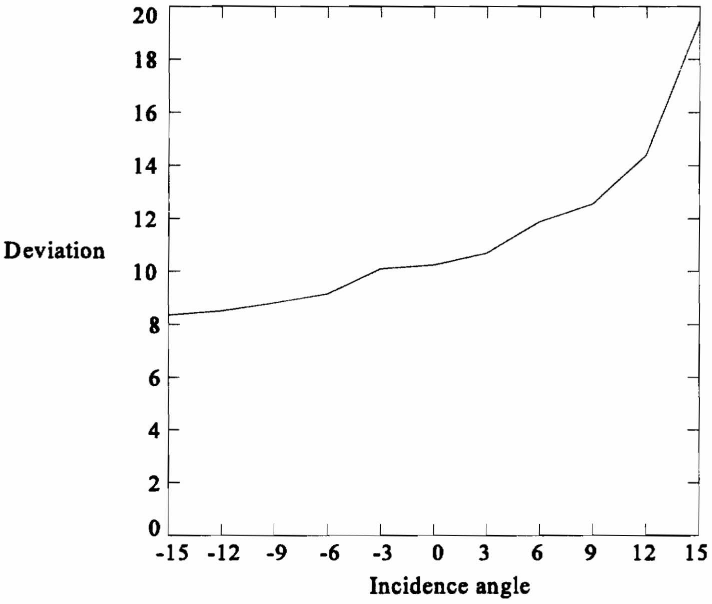

Figure 6.10b Deviation Angle vs. Incidence Angle

Figure 6.10 Total Pressure Loss and Deviation Angle vs. Incidence Angle

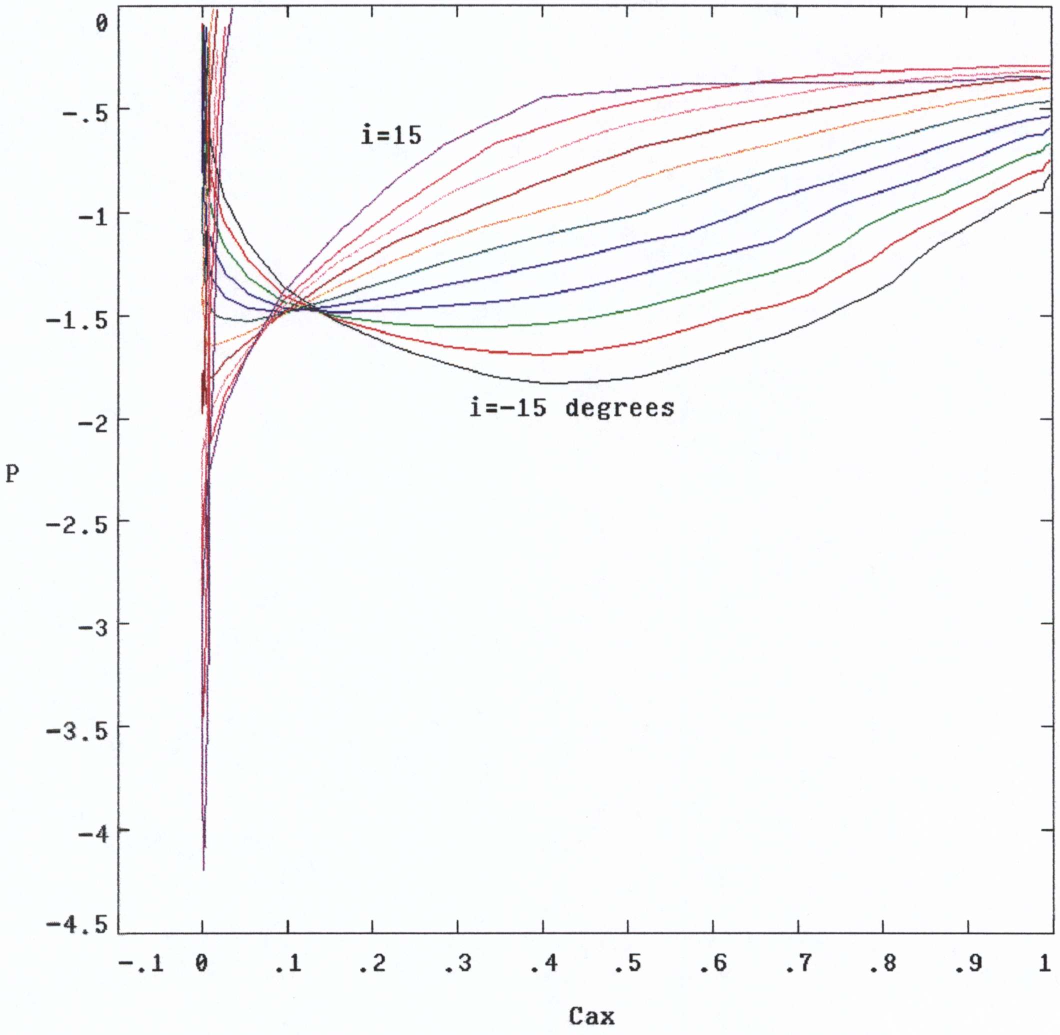

Figure 6.11 Normalized Static Pressure Profiles from Stagnation Point along Suction Surface for Incidence Calculations

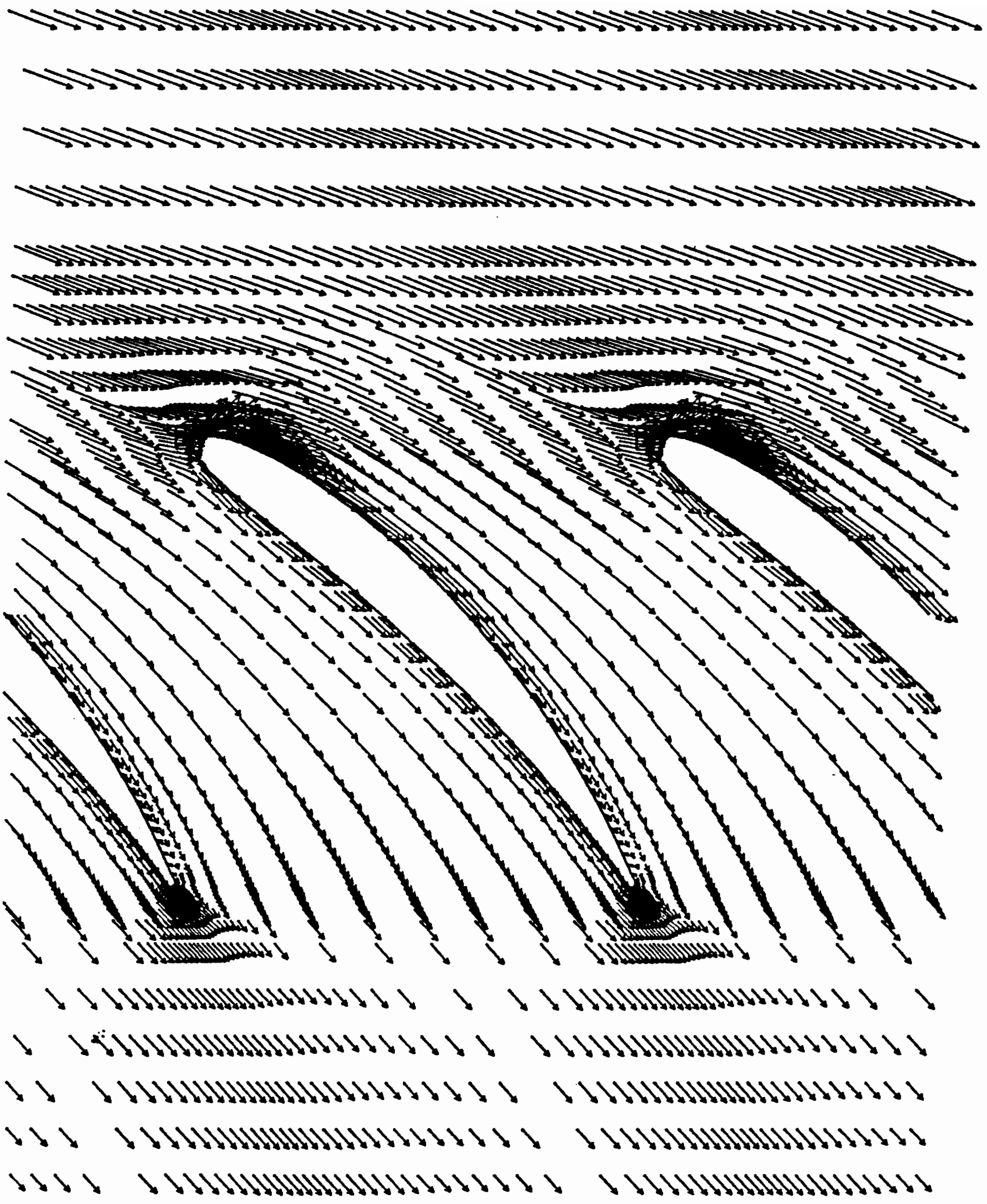

Figure 6.12 Velocity Vectors for 9 Degrees Incidence Calculation

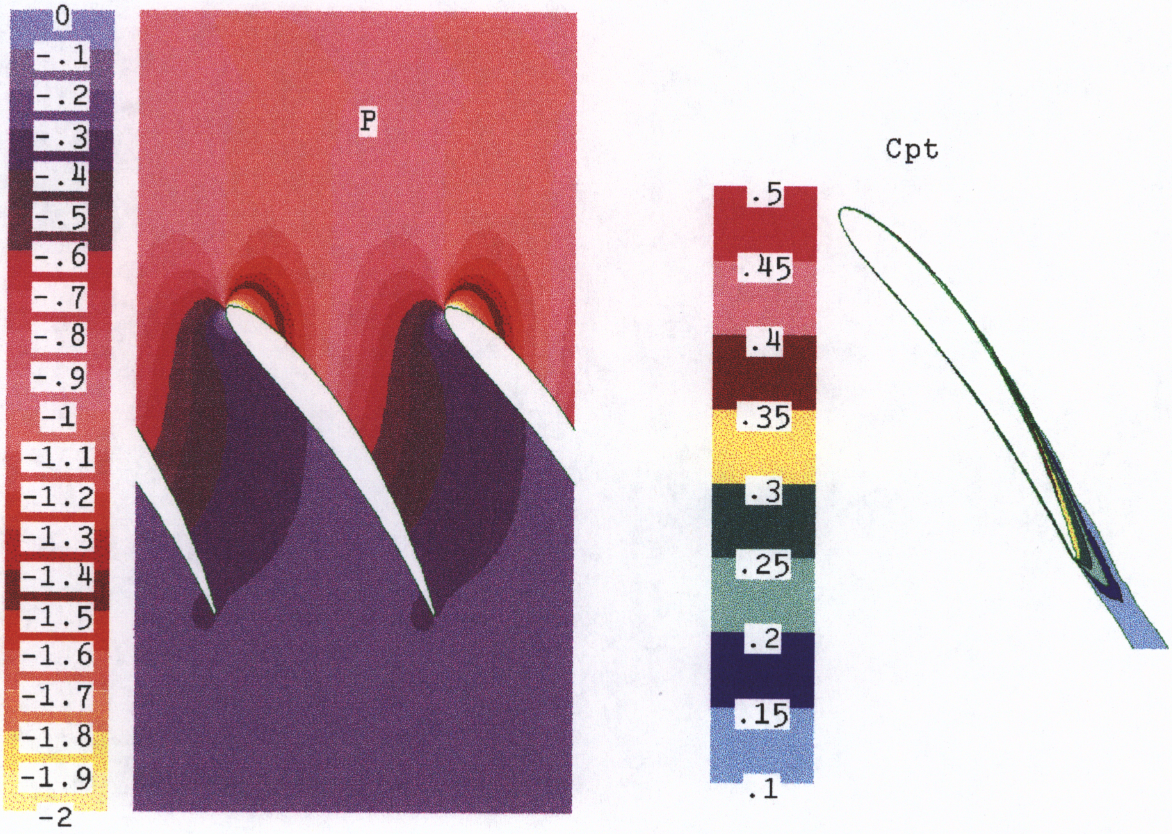

Figure 6.13 Static Pressure and Total Pressure Loss Contours for 9 Degrees Incidence

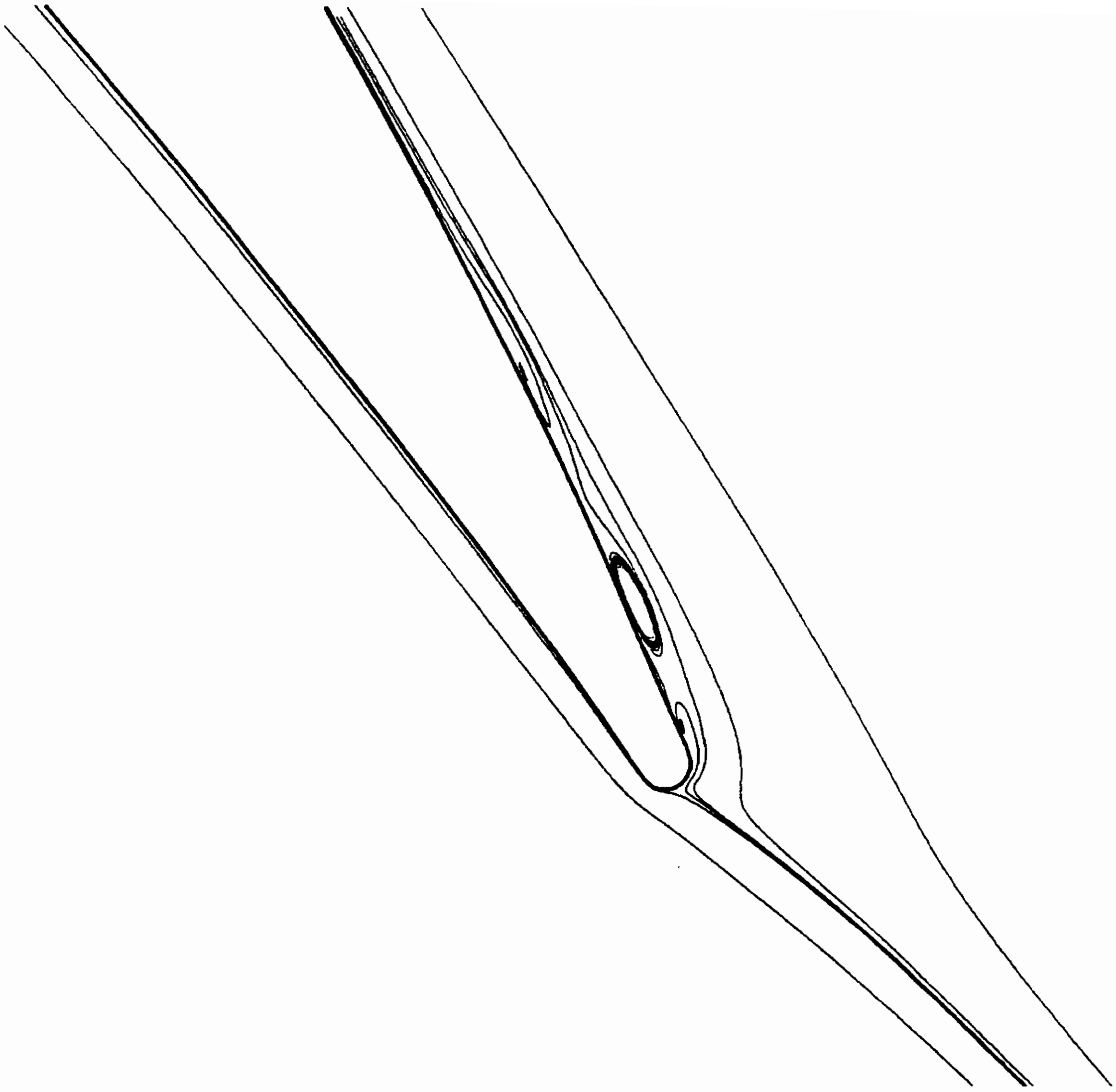

Figure 6.14 Streakline Plot for 9 Degrees Incidence , Separated Region

7.0 3-D Calculations

Chapter 7 describes the 3-D q-L transitional model calculation of the flow through the Deverson rotor. The discussion of the results is focused on the suction surface/hub corner stall as it was in Section 2.4 where the Deverson rig was discussed. The calculation was made for a flow coefficient, ϕ, of 0.51, which is the maximum total pressure rise point. The 3-D calculation grid used is described in Chapter 4.

7.1 Inlet Conditions

Inlet data was not available for ϕ=0.51. To determine the inlet conditions, it was assumed that the normalized velocity profile did not vary with flow rate. The absolute total pressure at the inlet of the Deverson rig is available for a flow coefficient, ϕ, of 0.57. Figure 7.1 is a plot of the radial total pressure profile. The data was taken using a boundary layer Pitot probe at Plane Ele, as depicted in Figure 2.11 (Rolls-Royce, 1994). Table 7.1 lists the inlet, exit, and measurement planes for the Deverson rig and the calculation. Plane Ele is 10% of the rotor chord upstream of the leading edge. This makes it too close to the leading edge to use as a calculation inlet plane. The calculation started 66% of an axial chord upstream of the leading edge. The total pressure profile from Plane Ele was used to set the inlet velocity profile for ϕ=0.51 at the calculation inlet plane. The normalized velocity profile from the calculation at Plane Ele was then compared with the measured profile at Plane Ele for a flow coefficient of 0.57.

Because the measured total pressure profile was for a flow coefficient of 0.57, the velocity profile based on it was scaled down to a flow coefficient of 0.51. This velocity profile can be seen in Figure 7.2 as the dashed line labeled i. The method used to scale the velocity profile down is described in Appendix A. The normalized total pressure profile

$$P_t = \frac{p_t - p_0}{-\rho U^2_{\mathrm{midheight}}} \qquad \textbf{(Eq. 7.1)}$$

based on this scaled down velocity profile is shown in Figure 7.3. The total pressure profile for Plane Ele is shown in the figure to verify that the profile has not changed. Figure 7.2 also shows the calculated velocity profile for Plane Ele. This profile is labeled e in the figure. It is seen that the profile has changed from the inlet and differs from the "measured profile", which is labeled by the circles. This is due to leading edge effects on the static pressure profile. The "measured velocity" profile is based on the measured total pressure profile assuming a uniform static pressure, which is not true.

The inlet relative angles for the calculation are shown in Figure 7.4. This figure shows that in the near-hub region, the incidence angle averages around 9 degrees and that from 25 to 75% of blade span that there is no incidence.

The q-L turbulence model requires initial values for q, the square root of the turbulence kinetic energy, and a free stream value for the mixing length, L_{fre}. The measured turbulence intensity, Tu, profile for a flow coefficient of 0.57 is shown in

Figure 7.5a. Q is obtained from the turbulence intensity by assuming isotropic turbulence

$$q = \sqrt{k} = \sqrt{\frac{u'^2+v'^2+w'^2}{2}} = \sqrt{\frac{3}{2}}\frac{Tu}{100}\overline{V}_{local} \qquad \textbf{(Eq. 7.2)}$$

Using V_{local} corresponding to a flow coefficient of 0.51, the resulting q profile is shown in Figure 7.5b. The remaining turbulence model parameter, L_{fre}, was set at 0.0033m based on a mixing length determined from the blade passage width.

Table 7.1 Axial Locations of Important Planes

STATION	z_{hub}	z_{shroud}	% axial chord
E	-	-	-1.5
calculation inlet plane	0.1957	0.1957	-0.66
start of hub rotation	0.2483		-0.23
ELE	0.256	0.256	-0.1
leading edge	0.2688	0.276	0
trailing edge	0.3563	0.3421	1
end of hub rotation	0.3604		1.05
G	0.364	0.364	1.2 (at casing)
calculation exit plane	0.4041	0.4041	1.43

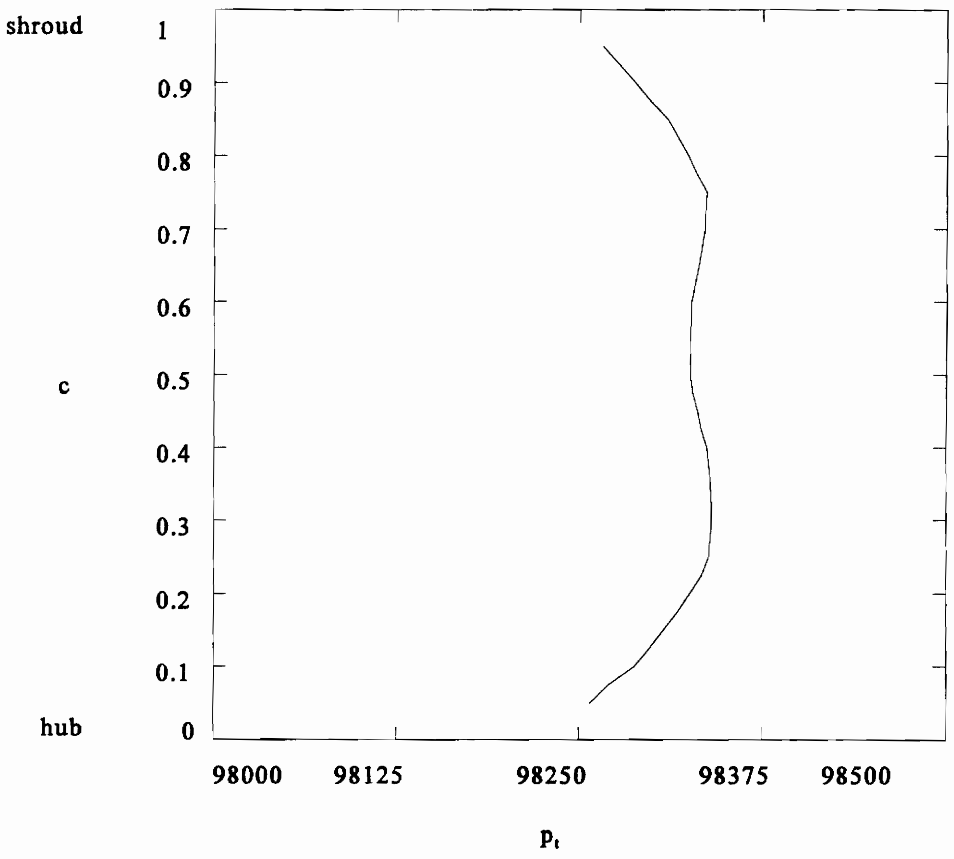

Figure 7.1 Absolute Total Pressure Profile for ϕ=0.57 at Plane Ele (Place, 1993)

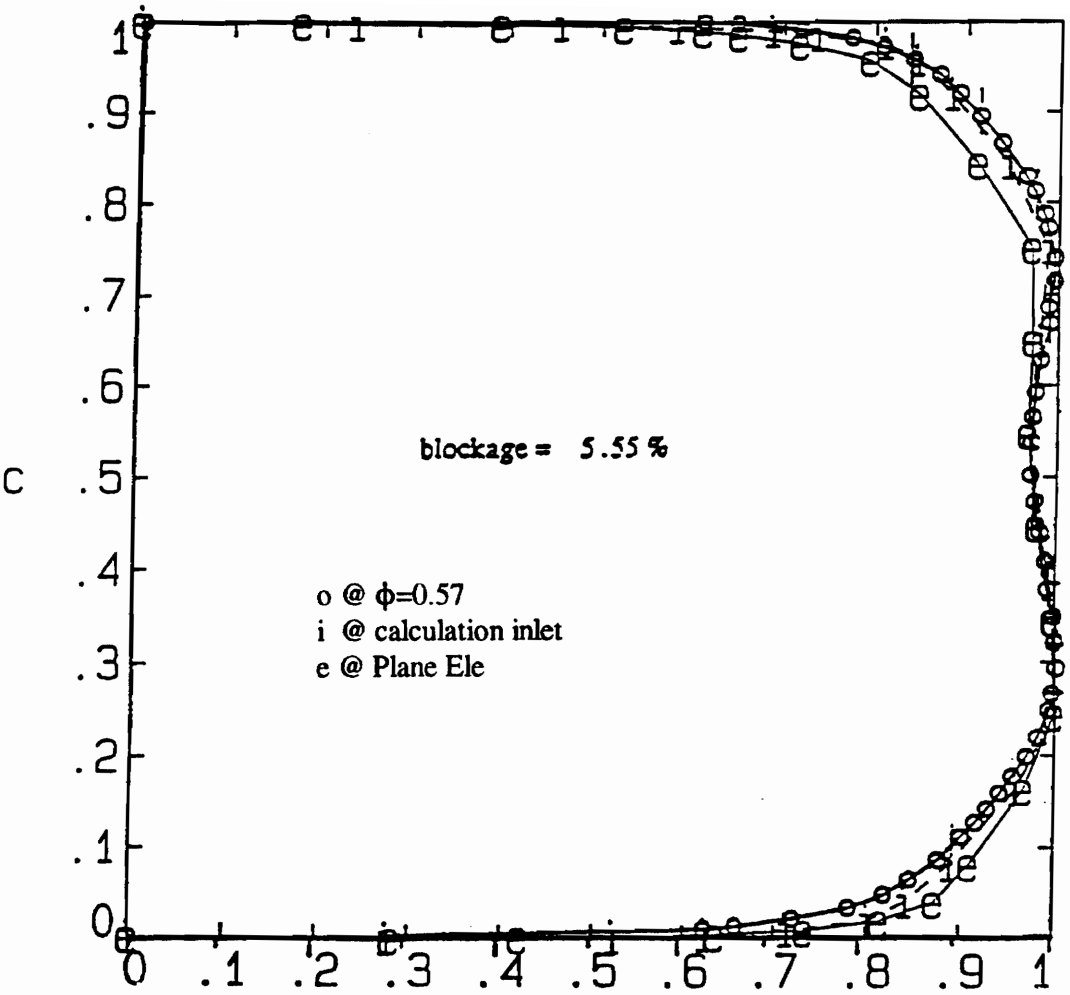

Figure 7.2 Circumferentially Averaged Calculation Inlet Velocity Profiles

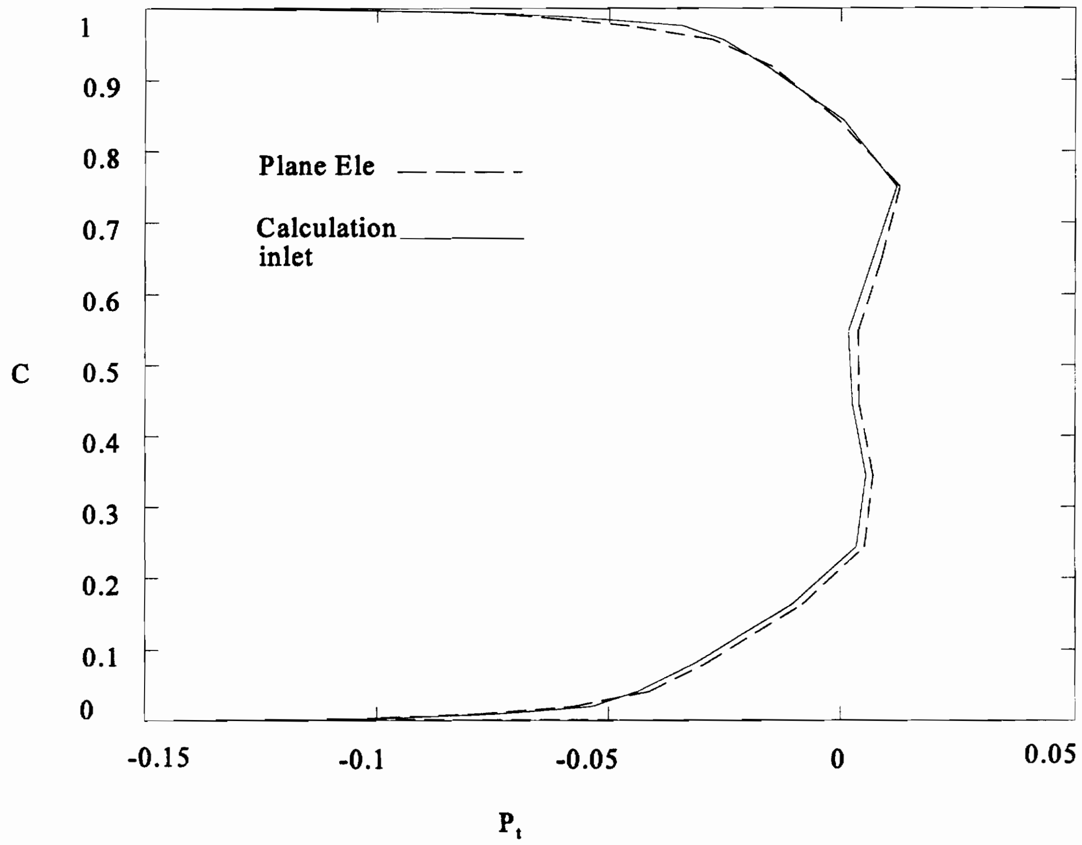

Figure 7.3 Circumferentially Averaged Absolute Total Pressure Profiles at Calculation Inlet

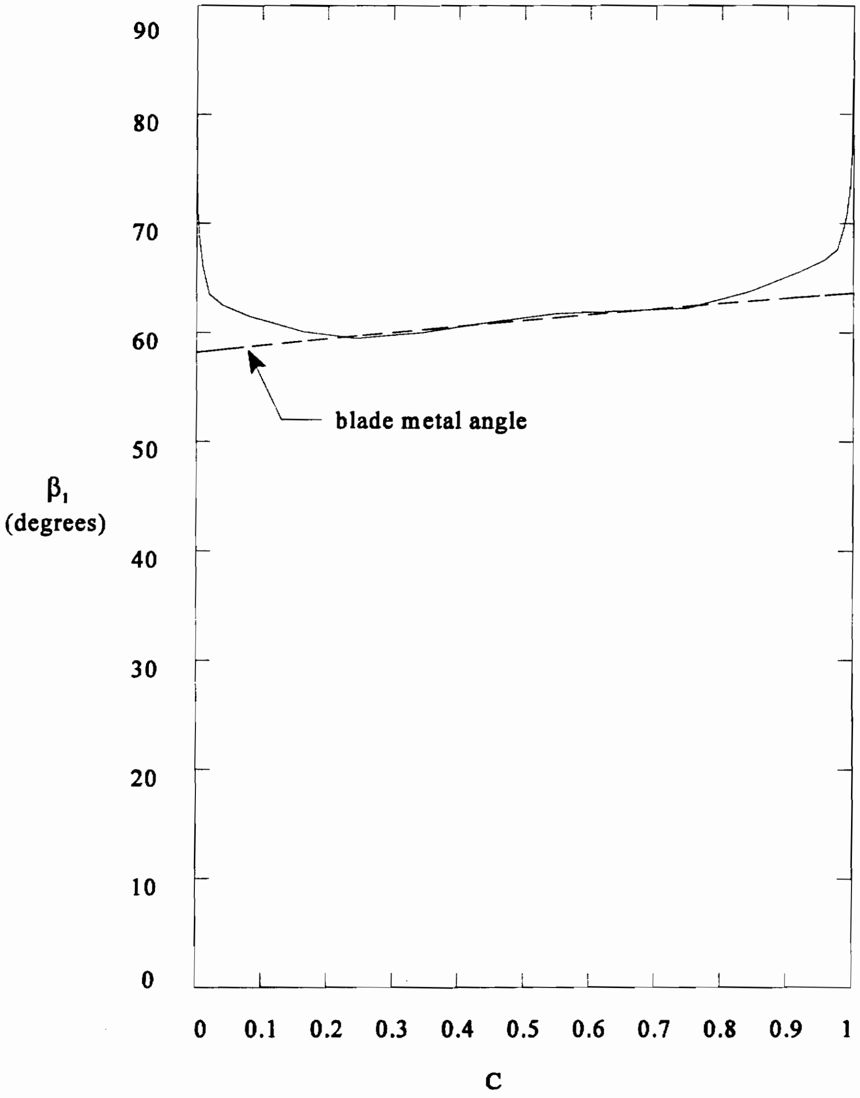

Figure 7.4 Inlet Flow Angles For MEFP q-L Calculation

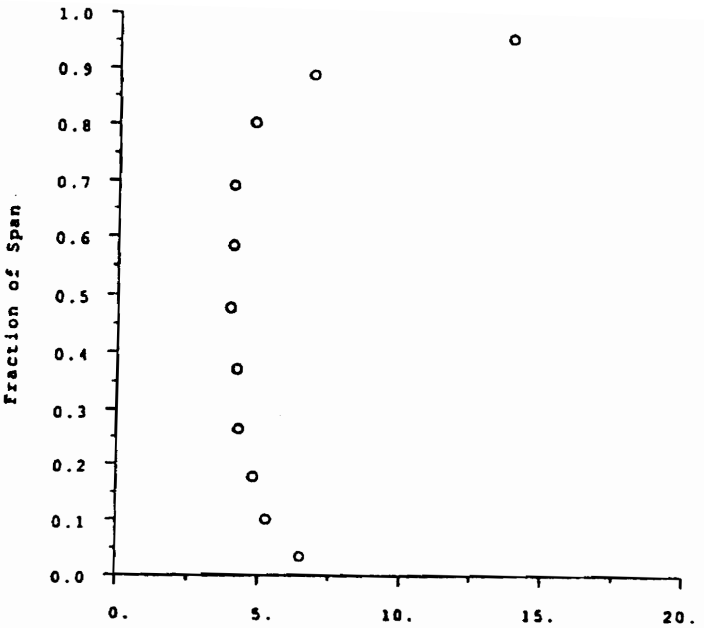

Figure 7.5a Measured Inlet Turbulence Intensity for ϕ=0.57

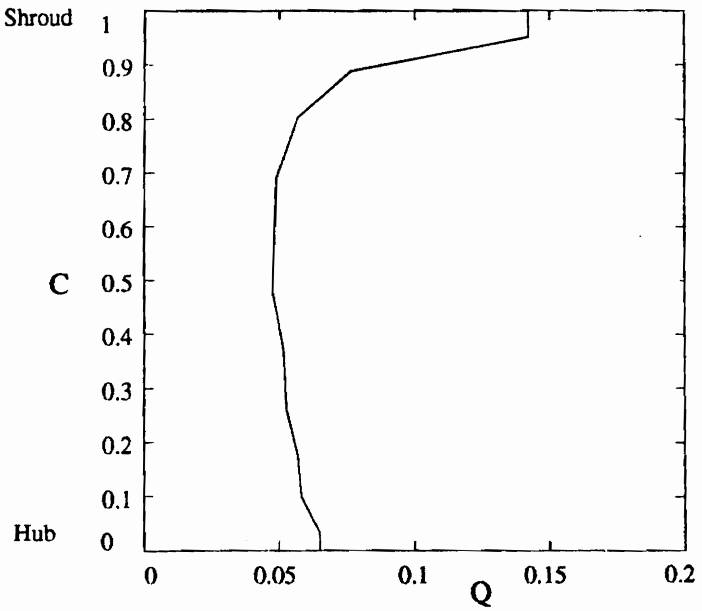

Figure 7.5b Square root of Turbulence Kinetic Energy at Inlet for ϕ=0.51

Figure 7.5 Turbulence Intensity Profile for ϕ=0.57(Place, 1993) and Q for ϕ=0.51 at Inlet

7.2 Comparison of Calculation Results to Data

All of the results presented in this section are from Plane G, 20% of axial chord downstream of the tip trailing edge. They will be compared with the data for the Deverson rig presented in Section 2.4. The normalized axial velocity contours, $V_z/U_{midheight}$, are shown in Figure 7.6. Comparing these with the contours shown in Figure 2.12, it is seen that they are very different in the corner stall region and along the trailing edge region. The calculated blade wake is too small; it is too narrow and the minimum axial velocities are higher than in the measurements. The calculation does predict corner stall at the hub, but the size of it is much smaller than it should be. The radial migration of the loss core seen in the measurements is also not in evidence. The loss core stays attached to the hub, and does not bulge out into the passage. The 0.2 contour barely leaves the hub, whereas the 0.2 contour interval in Figure 2.12 reaches 33% of span. The 0.4 contour in the actual rotor remains unclosed all the way up the blade span while the 0.4 contour from the calculation closes at only 12% of blade span.

Figure 7.7 shows the cicumferentially averaged axial velocity profile from the calculation along with the profile from the data. The under prediction of the width of the corner stall and the lack of radial migration, explains why a local velocity maximum seen at 10% span followed by the local minimum directly above this in the data is not seen in the calculation results. The axial velocity profile also shows that the hub boundary layer is too thin.

Figure 7.8 shows the rotor wake velocity profiles at 23% and 50% span. Comparing this with Figure 2.14, several things can be seen. Starting with the wake velocities at 23% span shown in Figure 7.8a, it is seen that the overall wake width is smaller than it should be. The calculated blade wake is only 23% of pitch compared to 36% for the data.

The free stream axial velocity is under predicted by approximately 5%, and as it approaches the pressure side of the blade wake, the drop in axial velocity is much more rapid than the more gradual decrease in the actual rotor. This was also seen by the lack of contour intervals in the blade wake in Figure 7.6. The axial velocity then drops off to only 0.325, approximately double the velocity in the Deverson rotor. This can be attributed to the loss core staying attached to the hub.

The free stream tangential velocity is under predicted by about 8%. It also remains constant until reaching the wake whereas the actual tangential velocity decreases as it approaches the wake. The tangential velocity within the wake is in good agreement reaching a maximum of just over 0.7. On the suction side of the wake, tangential velocity continues to gradually decrease until mid-passage where it increases slightly before leveling off. This is in contrast to the actual behavior of the velocity where it reaches a local minimum just beyond the wake and then increases until mid-passage where it then begins to decrease.

The radial velocity at 23% span is essentially zero except within the blade wake, with a small positive component within the middle of the wake. The peak radial velocity is 0.01 compared with approximately 0.1 in the actual rotor. This is also evidence showing the lack of radial migration of the loss core away from the hub.

The free stream relative velocity is also under predicted. The minimum relative velocity in the wake is similar to the measurements, 0.38 compared with approximately 0.32.

The wake velocity profiles at 50% span are shown in Figure 7.8b. The most noticeable difference is again that the wake width is too small. Here it is approximately 13% of pitch compared to the measurement of 23%. The free stream axial velocity is in good agreement at this height. As the wake is approached, the decrease in velocity is very sharp on the pressure side. The drop in axial velocity within the wake is under predicted by approximately 30% while the profile as it leaves the suction side of the wake is in good agreement.

The free stream tangential velocity is over predicted by 13%. The tangential velocity also has a minimum around mid-passage that is in contrast to the level profile seen in Figure 2.14. The tangential velocity is also slightly over predicted in the middle of the blade wake.

The free stream radial velocity is zero on the suction side of the passage then becoming positive as it approaches the pressure surface side of the wake. The radial velocity within the wake is unusual. There is a small amount of radial velocity from the pressure surface but on the suction side of the wake it quickly drops to a small negative value. In comparison with the actual radial velocity, there should be a slightly negative radial velocity in the free stream with that becoming more strongly negative as it approaches the pressure side of the wake. The radial velocity within the wake should be positive throughout, which it is not. This probably suggests that the secondary flows on the blade surfaces are not strong enough or nonexistent.

Figure 7.9 shows the deviation angles along with the measured deviation angles. The characteristic local overturning and under turning of the flow is shown clearly between 0 and 20% of span. The deviation angles show the presence of the corner stall where the angle reaches a local maximum of 12 degrees at 5% of span. The loss core that causes this under turning has not migrated off the hub so that the local maximum does not coincide with the data. The deviation angles are overall smaller than the data in the hub half because the corner stall region is to small. The secondary flow in the hub boundary layer which causes the local over turning is to close to the hub. This may correspond with the hub boundary layer being too thin.

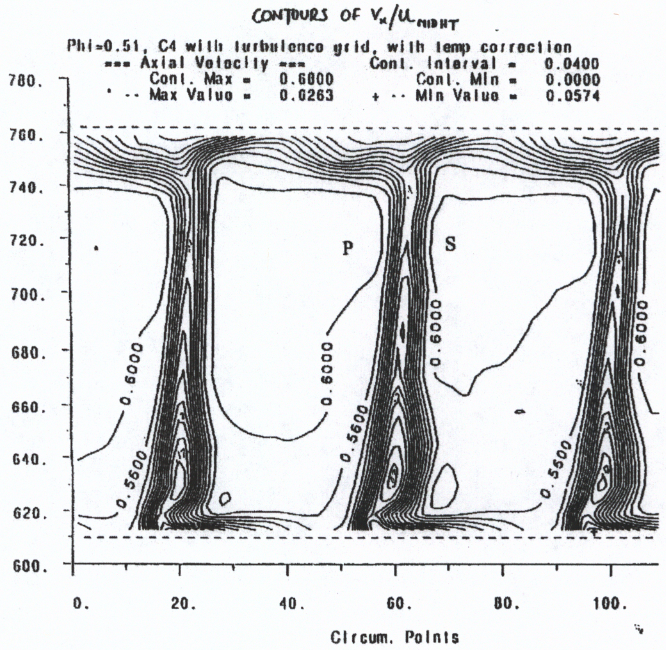

Figure 2.12 Axial Velocity Contours, $V_z/U_{midheight}$, for the Deverson Rig (Place, 1993)

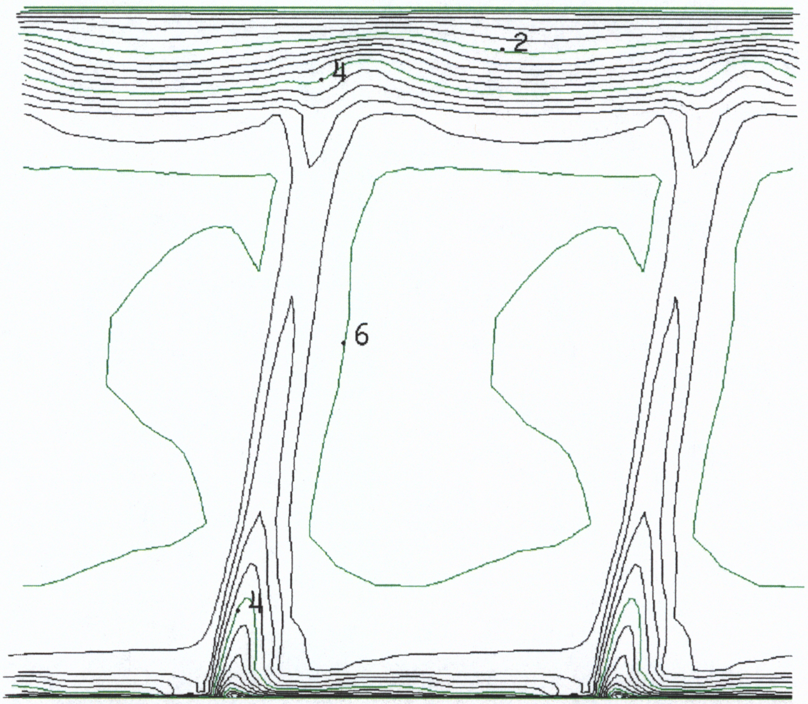

Figure 7.6 Axial Velocity Contours, $V_z/U_{midheight}$, for MEFP q-L Calculation at Plane G (Contour interval = 0.04)

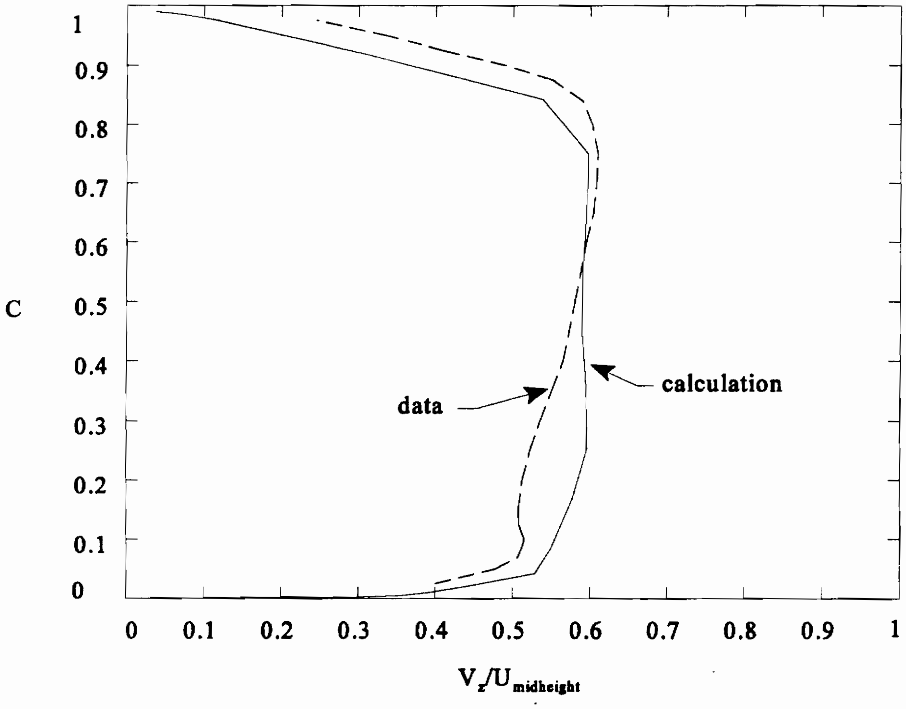

Figure 7.7 Circumferentially Averaged Axial Velocity Profile for MEFP q-L Calculation at Plane G

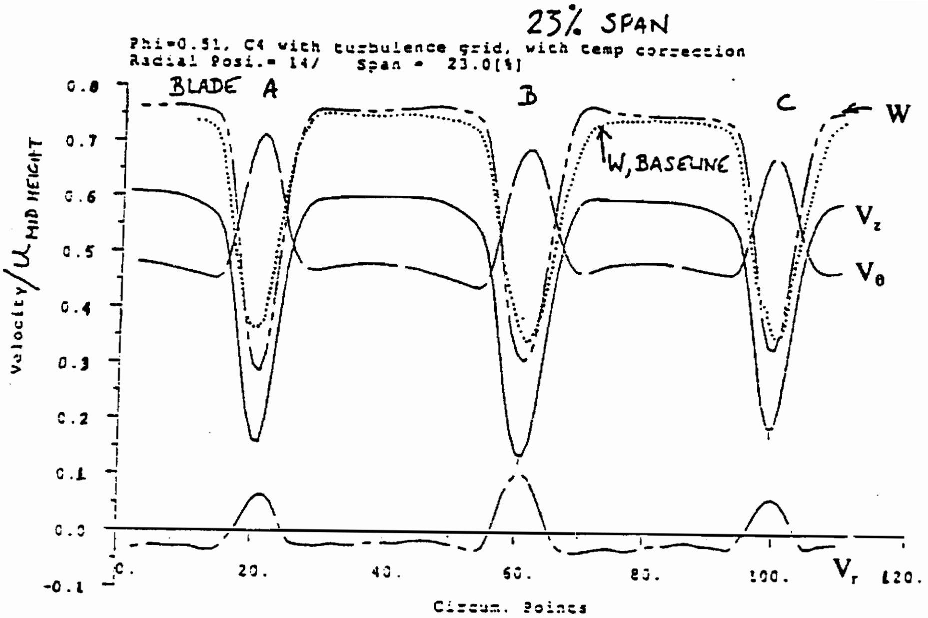

Figure 2.14 Rotor Wake Velocity Profiles at 23% for the Deverson Rig (Place, 1993)

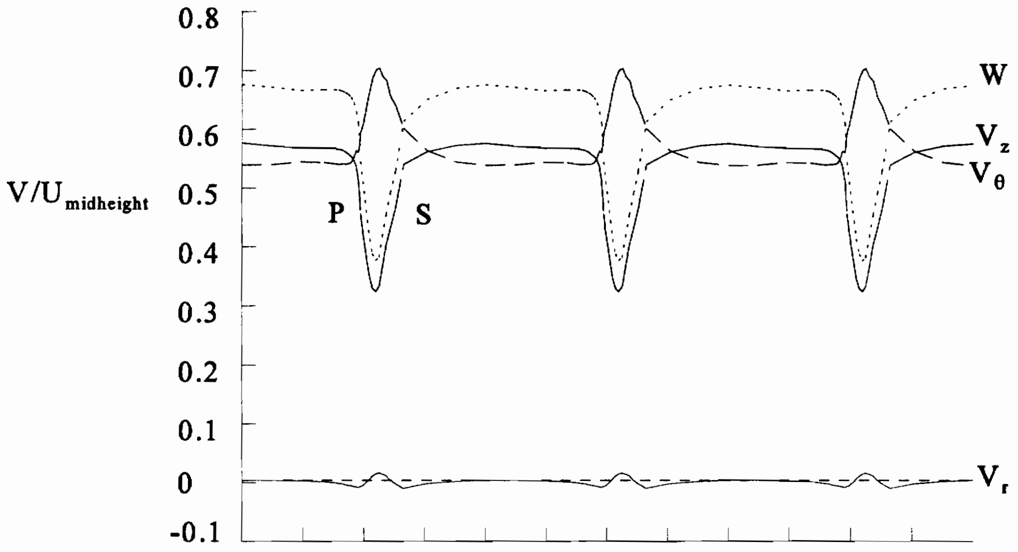

Figure 7.8a Wake Velocities at 23% Span

Figure 7.8 Rotor Wake Velocity Profiles at 23% Span for MEFP q-L Calculation at Plane G

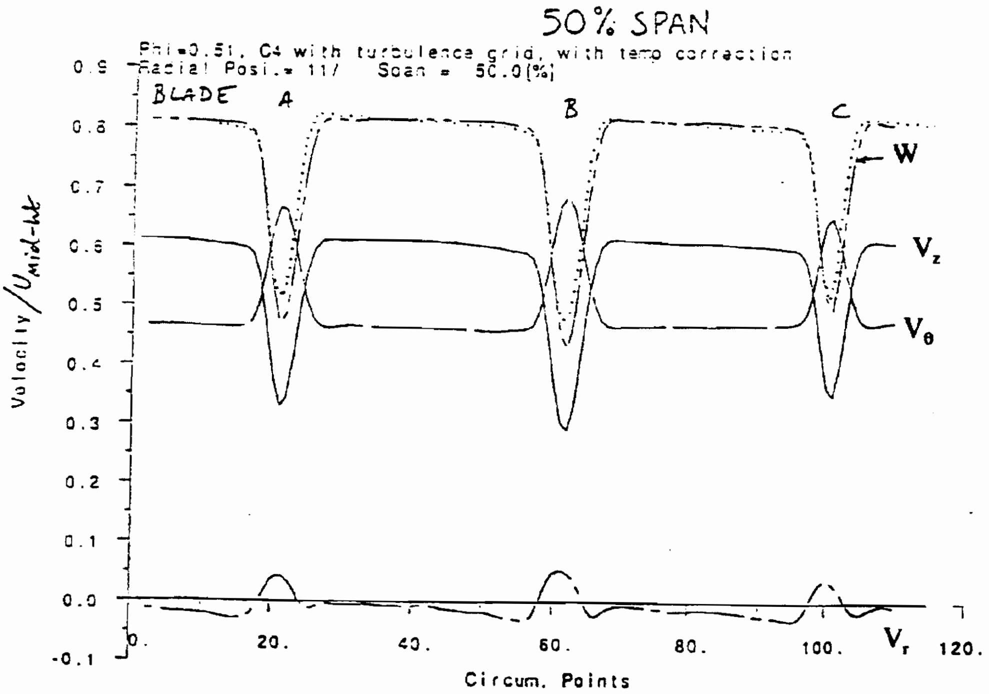

Figure 2.14 Rotor Wake Velocity Profiles at 50% for the Deverson Rig (Place, 1993)

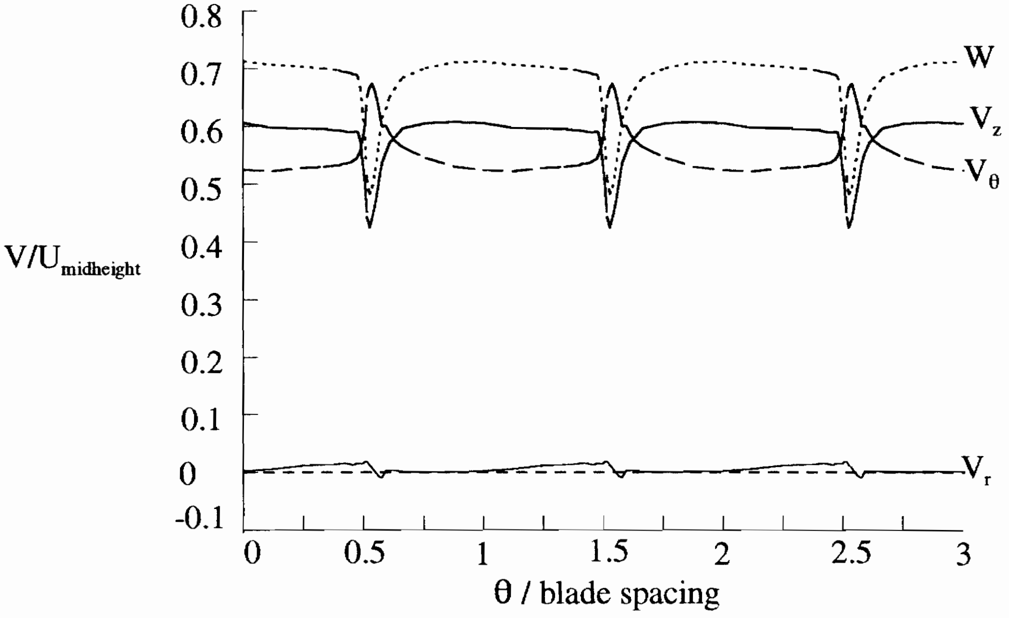

Figure 7.8b Wake Velocities at 50% Span

Figure 7.8 Rotor Wake Velocity Profiles at 50% Span for MEPF q-L Calculation at Plane G

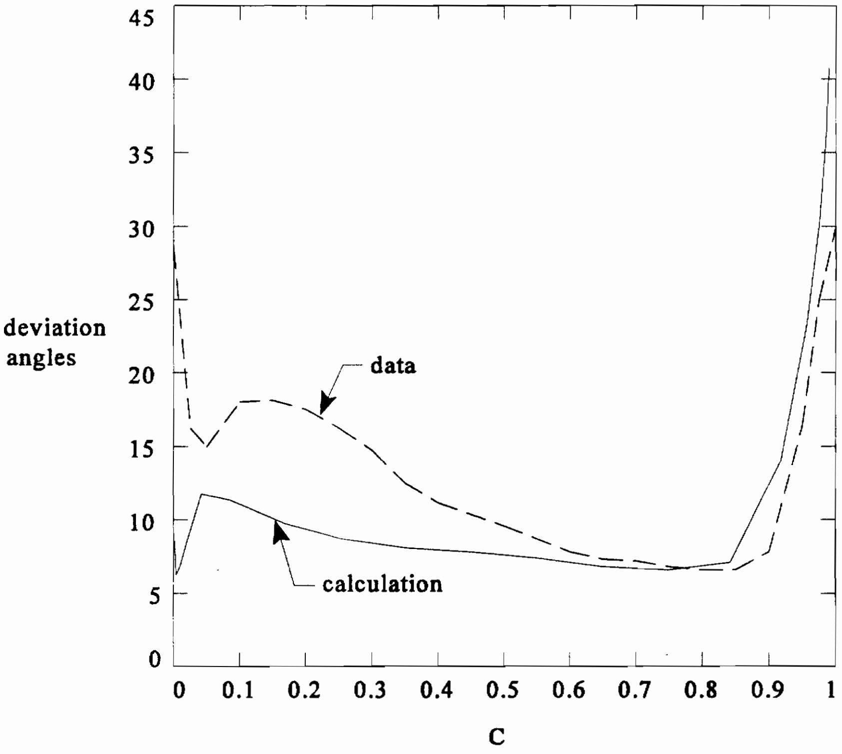

Figure 7.9 Deviation Angles for MEFP q-L Calculation at Plane G

7.3 Transition on the Suction Surface of the Blade

The location of transition on the suction surface of the blade is determined as described in Chapter 6. The transition function from MEFP, F_{tu}, is used to detect when transition occurs. The start of transition is considered 0.1 and the end of transition is 0.9. F_{tu} is only relevant where there is a boundary layer. To produce a contour plot of F_{tu} only where it is relevant, F_{tu} was multiplied by a 0, 1 function at each point to give the variable, DF_{tu}. Zero was used when there was no boundary layer present, and one when there was a boundary layer. The resulting contour plot of DF_{tu} can be seen in Figure 7.10. The plot is of the first grid planes, j=20 and k=2, away from the suction surface and hub respectively. The first contour, from $DF_{tu} = 0.025$ to 0.1, corresponds to laminar flow.

Closest to hub on the suction surface, transition starts at 22% of chord and the flow never becomes fully turbulent in the corner. In the hub region of the rotor, the incidence angle is approximately 9 degrees. In the 2-D cascade study at this incidence, transition occurred at 13% of chord. The difference here is attributable to the radial relief mechanism discussed in section 2.1.1.1. At 50% span, where the incidence angle is zero, the start of transition occurs at 47% of chord and ends at 66% of chord. The start of transition on the rotor suction surface compares well with the result for the incidence angle of zero in the 2-D study where transition occurred at 49% of chord. The DF_{tu} contours on the hub show that the boundary layer is fully turbulent as it enters the rotor passage.

Of particular interest is how F_{tu} behaves within the corner stall region and all along the suction surface / hub intersection. It was noted that F_{tu} did not predict an end to transition in the near hub region. F_{tu} also predicts laminar/transitional flow occurring within the separated region of flow in the suction surface/trailing edge/hub region. These two cases suggest the transitional q-L model is not able to handle backflow accurately.

Figure 7.11 is a contour plot of the turbulence intensity normalized with $U_{midheight}$, Q, on the same plane as Df_{tu} along the suction surface. The Q contours can also be used to give an approximate location to transition. During transition, Q will rapidly increase in value. This can be seen in the figure where Q rapidly increases from 0.025 to 0.125 over much of the span. This region of rapidly increasing Q coincides with F_{tu} as it increases from .1 to .9 during transition.

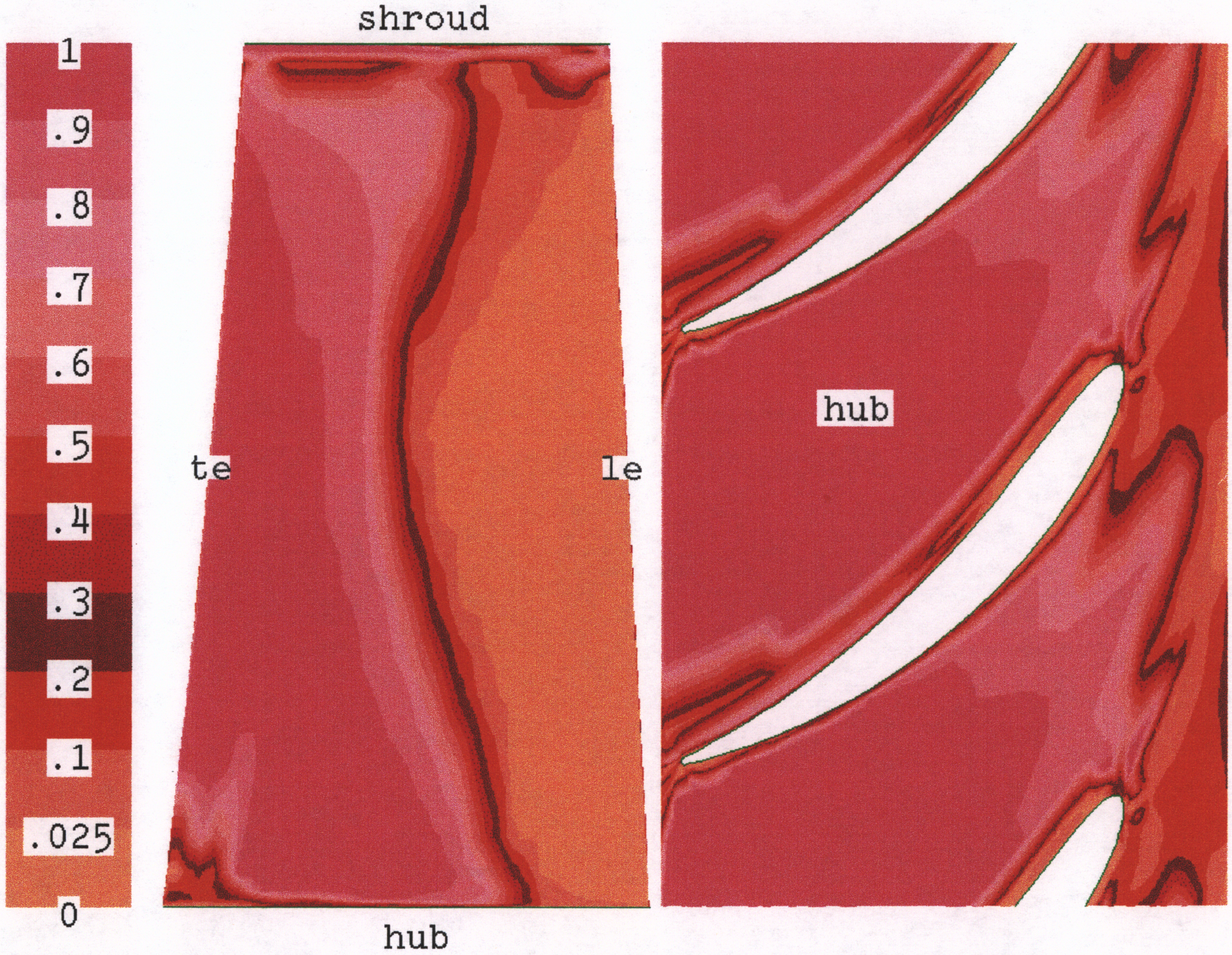

Figure 7.10 DFtu Contours for Near-Wall Suction Surface Plane j=20, and Near-Wall Hub Plane k=2

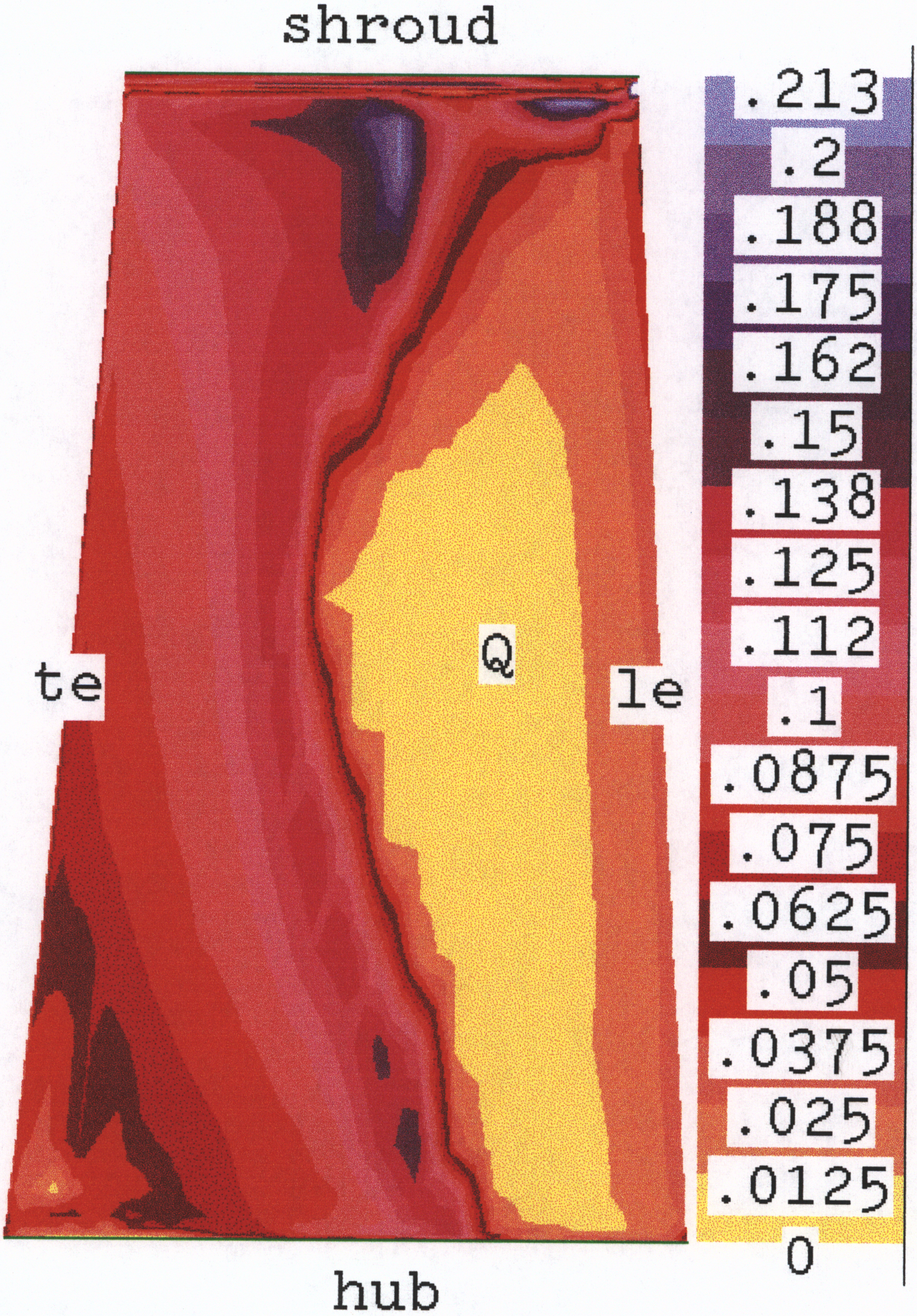

Figure 7.11 Q Contours on Near-Wall Suction Surface Plane j=20

7.4 Secondary Flows

This section will focus on the secondary flows and their interaction with the corner stall. Rotary stagnation pressure, p^*, for compressible flow is

$$p^* = p\left(\frac{C_pT+\frac{W^2}{2}-\frac{U^2}{2}}{C_pT}\right)^{\frac{\gamma}{\gamma-1}} \qquad \textbf{(Eq. 7.3)}$$

p^* as a loss coefficient,

$$P^*_{loss} = \frac{-(p^*-p_0)}{\rho U^2_{midheight}} \qquad \textbf{(Eq. 7.4)}$$

is used as a measure of the losses in the rotor. Gradients of p^* give rise to streamwise vorticity (Eq. 2.1) which can be seen in the secondary flows. These secondary flows then cause the convection and accumulation of high loss fluid.

Figures 7.12 through 7.15 show a progression of rotary stagnation pressure loss contours, in blade to blade planes, at 10, 30, 50, 60, 70, 80, 90, and 98% of axial chord. The secondary flow velocity vectors are also shown. The secondary flow vectors are defined by the grid space. The velocity vector at each grid point is the vector sum of velocities in the i, j, and k grid directions. The primary flow is defined as the i vector component with the j and k vector components being the secondary flow.

Figure 7.12 contains the planes at 10 and 30% of chord. There is very little loss at the 10% plane with the most concentrated on the hub toward the pressure surface and on the suction surface near the hub. The secondary vectors show that there is a strong radially inward velocity on the suction surface that illustrates the radial relief discussed in the previous section. The secondary flow along the hub from the pressure to suction surface is just starting and is very weak. The 30% plane shows the rotary stagnation pressure losses starting to thicken along the hub and suction surface. These increases result in stronger hub secondary flow from the pressure surface to the suction surface and the beginning of a radially outward velocity on the suction surface near the hub.

Figure 7.13 shows the planes at 50 and 60% of chord. The P^* losses continue to build particularly in the suction surface/hub corner region. The hub region of secondary flow coming from the pressure surface increases along the hub in the area where the losses build. The radially outward secondary flow on the suction surface also becomes larger where the losses are building. This is seen by more of the vectors in this region changing from radially negative to radially positive. The losses along the hub at the 60% plane change little with the secondary flow from the pressure to suction sides also remaining relatively the same. However, the losses in the suction surface/ hub region continue to build with the positive radial secondary flow continuing to grow stronger.

Figure 7.14 contains the 70 and 80% planes. The same general trend continues in these planes. The hub losses and secondary flows remain stable while the losses continue to build in the suction surface/hub region with the accompanying increase in positive radial secondary flows. It is between the 60 and 70% planes that the contour lines change character from a boundary layer to a corner stall. This is seen by the loss contours beginning to widen significantly from the 60 to 70 and then to the 80% plane.

Figure 7.15 shows the final two planes at 90 and 98% of chord. The losses have continued to build in the corner stall region with the suction surface radial secondary flow continuing to grow as well. There is very little change in the losses at the 98% plane and the radial secondary flows have begun to decrease in magnitude. The hub secondary flows from the pressure to suction surface have been decreasing slightly from the 70% plane to the 98% plane as P* along the hub changes very little over these planes. The secondary vectors at the 98% plane show that the hub secondary flows have decreased significantly from their former strength. The reason for this is that the curvature term in Eq. 2.1 which drives this secondary flow has begun to decrease as the streamline radius of curvature, R_n, becomes larger.

Figure 7.16 is a plot of the mass averaged losses in the bottom half of the rotor passage. It shows the rapid build up of losses through the first 30% of the blade passage due to the build up of losses along the hub and lower suction surface. The losses continue to grow from 30% to 90% of the blade passage but at a slower pace. These losses are due to the build up in the suction surface/ hub region. The even slower growth of losses from 90% of the blade passage to the trailing edge was shown by the relatively minor changes in the rotary stagnation pressure loss contours at 90 and 98%. The steady build up of losses in the suction surface/hub region to 60% can be partly attributed to the hub secondary flows convecting the high loss fluid generated in the hub boundary layer to this region. The rapid increase in losses in this region for the remainder of the blade passage is credited to the development of the corner stall.

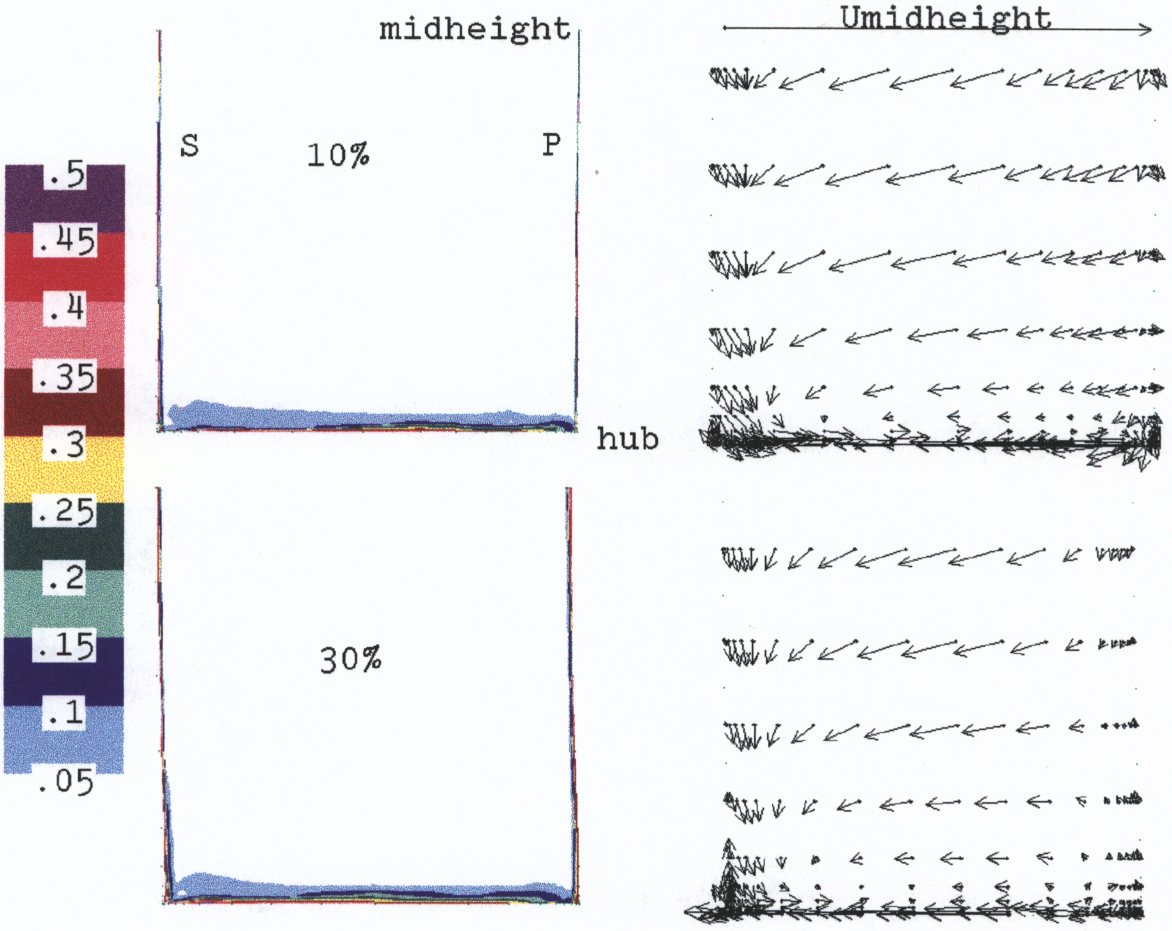

Figure 7.12 P^*_{loss} Contours and Secondary Flow Vectors for Planes at 10 and 30% of Axial Chord

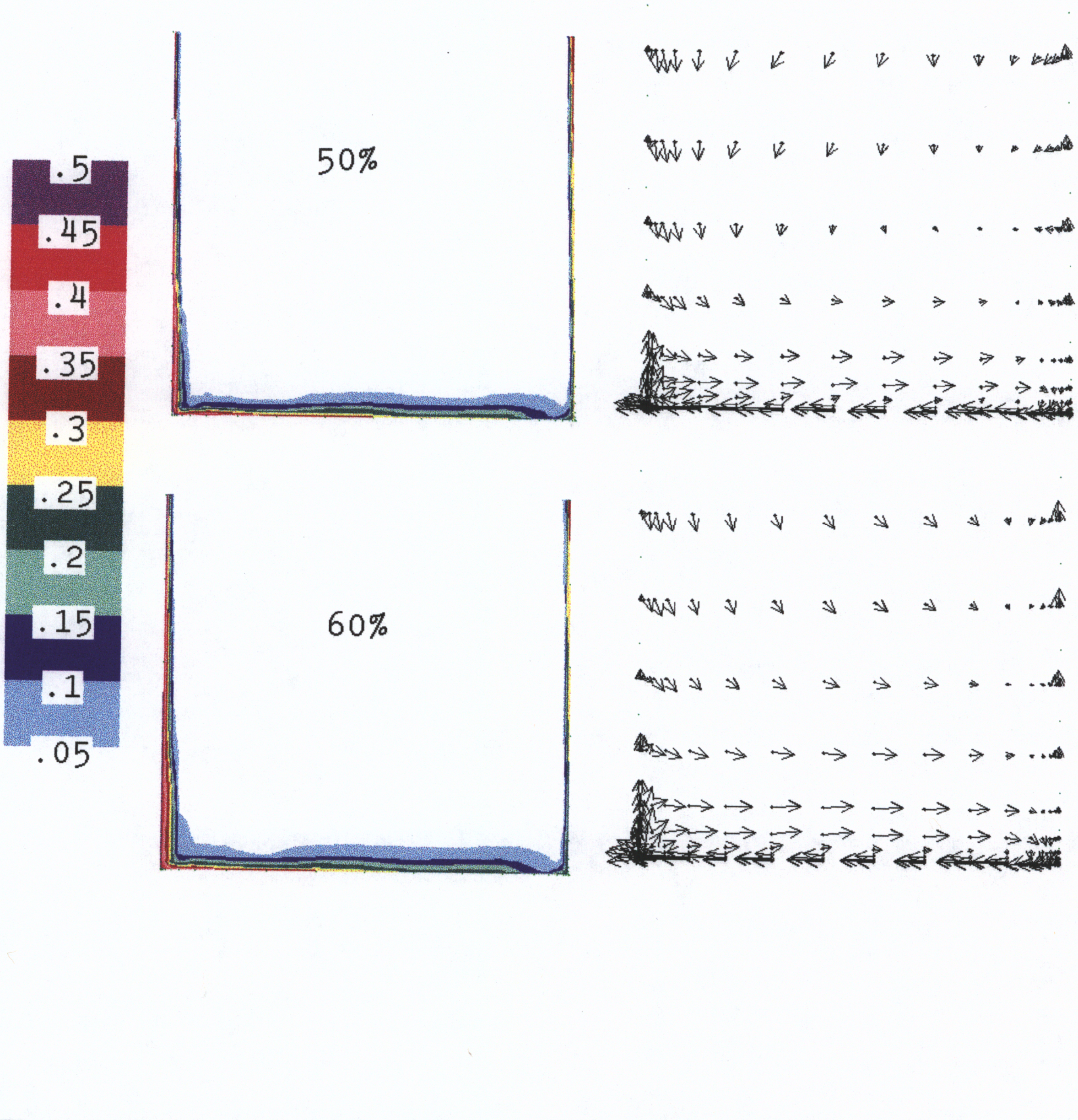

Figure 7.13 P^*_{loss} Contours and Secondary Flow Vectors for Planes at 50 and 60% of Axial Chord

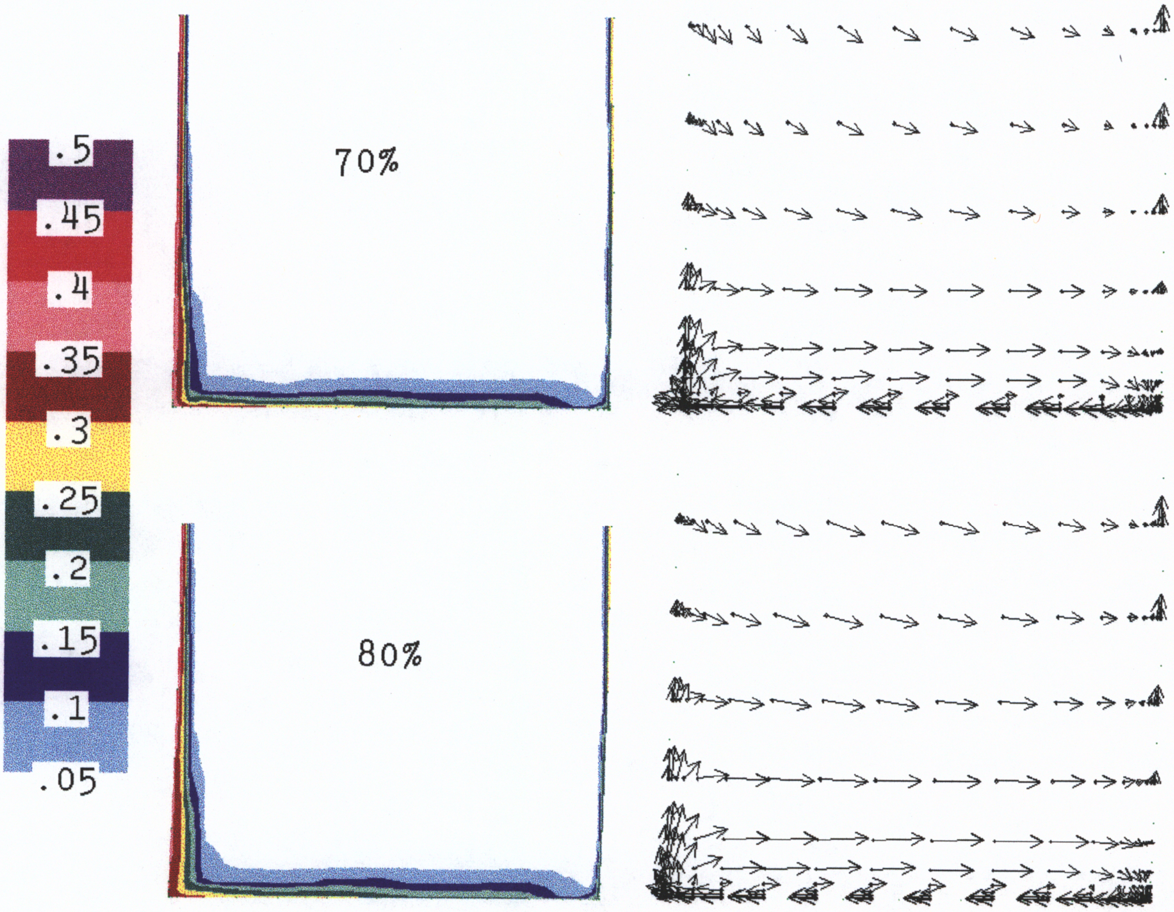

Figure 7.14 P^*_{loss} Contours and Secondary Flow Vectors for Planes at 70 and 80% of Axial Chord

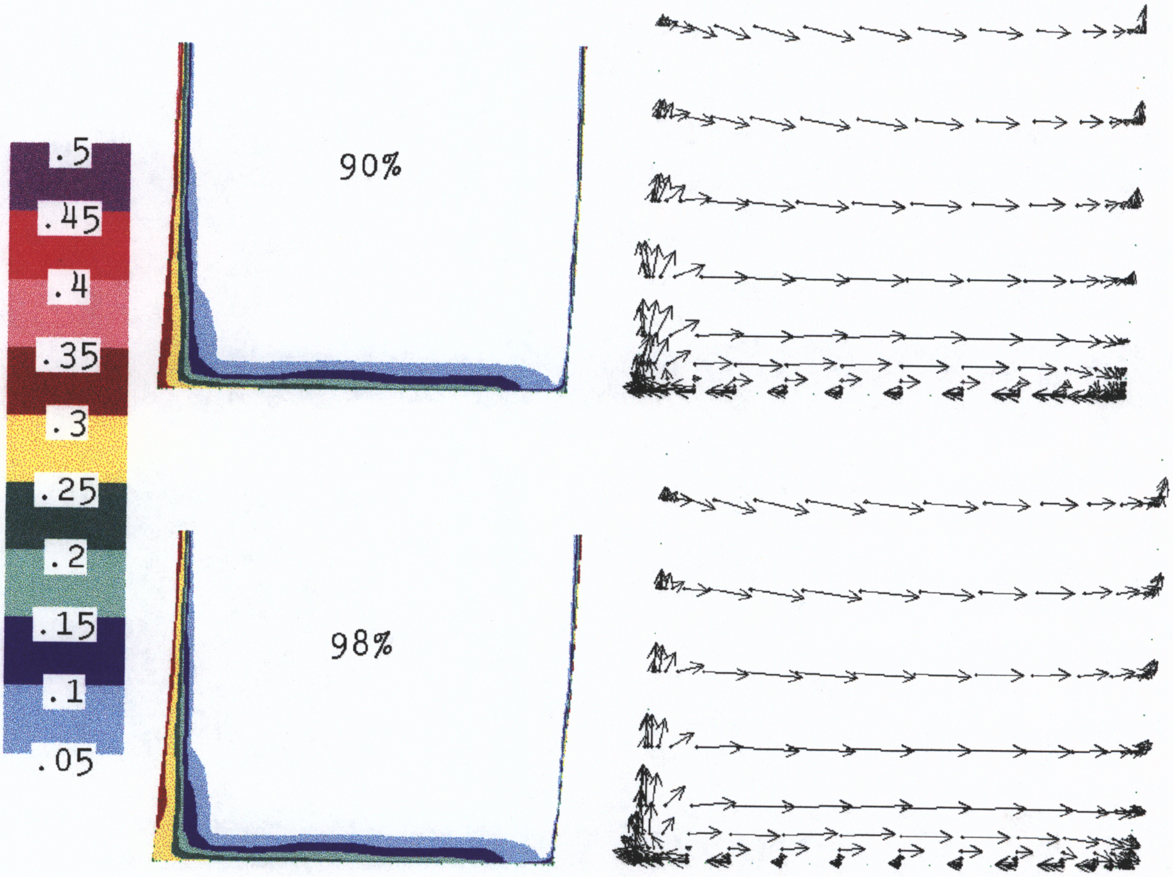

Figure 7.15 P^*_{loss} Contours and Secondary Flow Vectors for Planes at 90 and 98% of Axial Chord

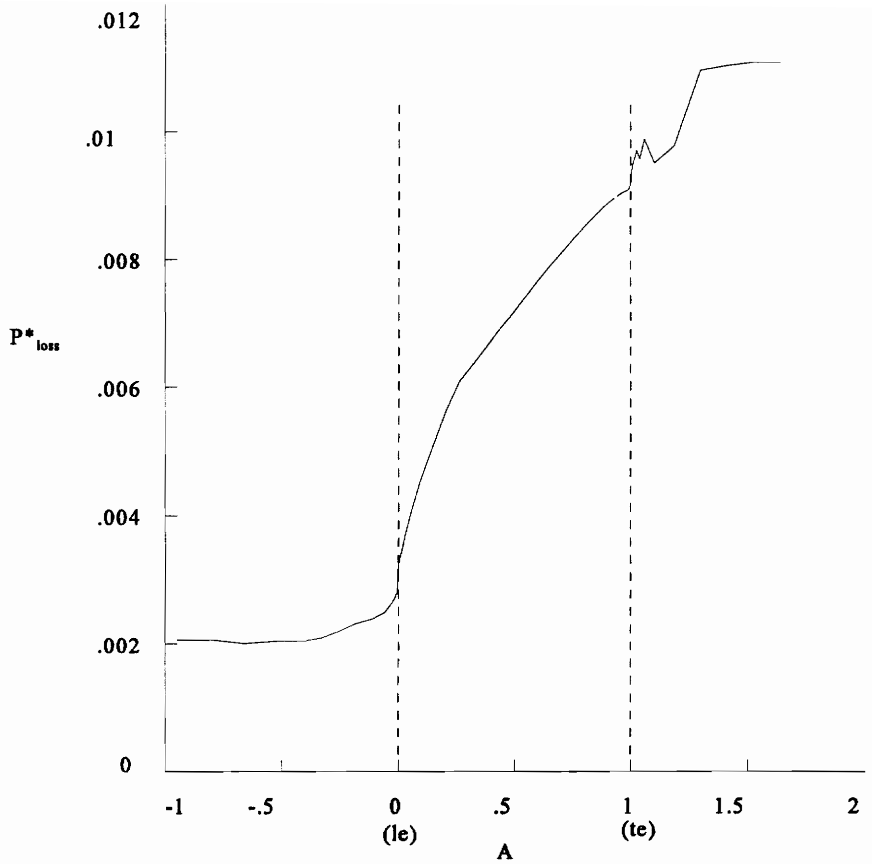

Figure 7.16 Mass Averaged Loss in the Bottom Half of Rotor Passage for MEFP q-L Calculation

7.5 Streakline Analysis

The corner stall region was also investigated using the streakline program described in Chapter 5. The main method of analysis was to limit the streaklines to specific grid planes to provide an understanding of the secondary flows. This was done on six consecutive grid planes starting half way between the suction surface and the near suction surface grid points. This corresponds to a grid coordinate of j=19.5 for the first plane. The remaining planes are: j=20.5, 21.5, 22.5, 23.5, and 24.5. The j=19.5 plane is 0.06% of blade passage width from the suction surface and the j=24.5 plane is 2.4% away.

Figure 7.17 shows the limiting streaklines on plane j=19.5 and the limited steaklines on plane j=20.5. On plane j=19.5, the first separation line starts at the leading edge/ hub corner and then around 20% of chord moves up the surface rapidly to approximately 20% of blade span. This corresponds to the transition from a laminar boundary layer to a laminar separation bubble. This separation line reaches a height of 30% of blade span at the trailing edge. The next two streaklines past the separation line are caught in this bubble as seen by their rapid movement up the suction surface and slightly upstream. The streaklines above the first separation line show a radially outward movement in the region of transition from a laminar to a turbulent boundary layer. This may be from the boundary layer being on the verge of transitioning via a laminar separation bubble.

Small amounts of backflow appear in the hub corner starting at around 50% of chord. These streaklines that first show backflow from the corner stall form the separation line for the stalled region of fluid. This separation line reaches approximately 24% of blade span by the trailing edge. Most of the stalled fluid moves radially upward where it is then turned downstream by the separation line. The largest region of backflow is near the trailing edge. The streaklines on plane j=20.5 show that the laminar separation bubble is only one grid point thick. There is only one separation line on this plane, due to the corner stall. Backflow begins around 60% of chord in the hub corner with most of the stalled fluid moving radially upward before heading off downstream. The radially upward velocity component caused by the corner stall on streaklines above the separation line at the trailing edge seen on the j=19.5 plane has largely disappeared on the j=20.5 plane. Note for the j=20.5 plane the streakline plot extends downstream of the trailing edge, but for j=19.5, the plot ends at the trailing edge.

Figure 7.18 shows the remaining four j planes from the hub to 50% of blade height. The streaklines on plane j=21.5 show that the corner stall has been halved in size from the near suction surface plane but still has a significant effect on the flow. Plane 22.5 shows that backflow has largely disappeared except for a small amount in the hub corner/trailing edge region. The main effect still present from the corner stall is a radially upward velocity component. The remaining two planes show the effects of the corner stall disappearing.

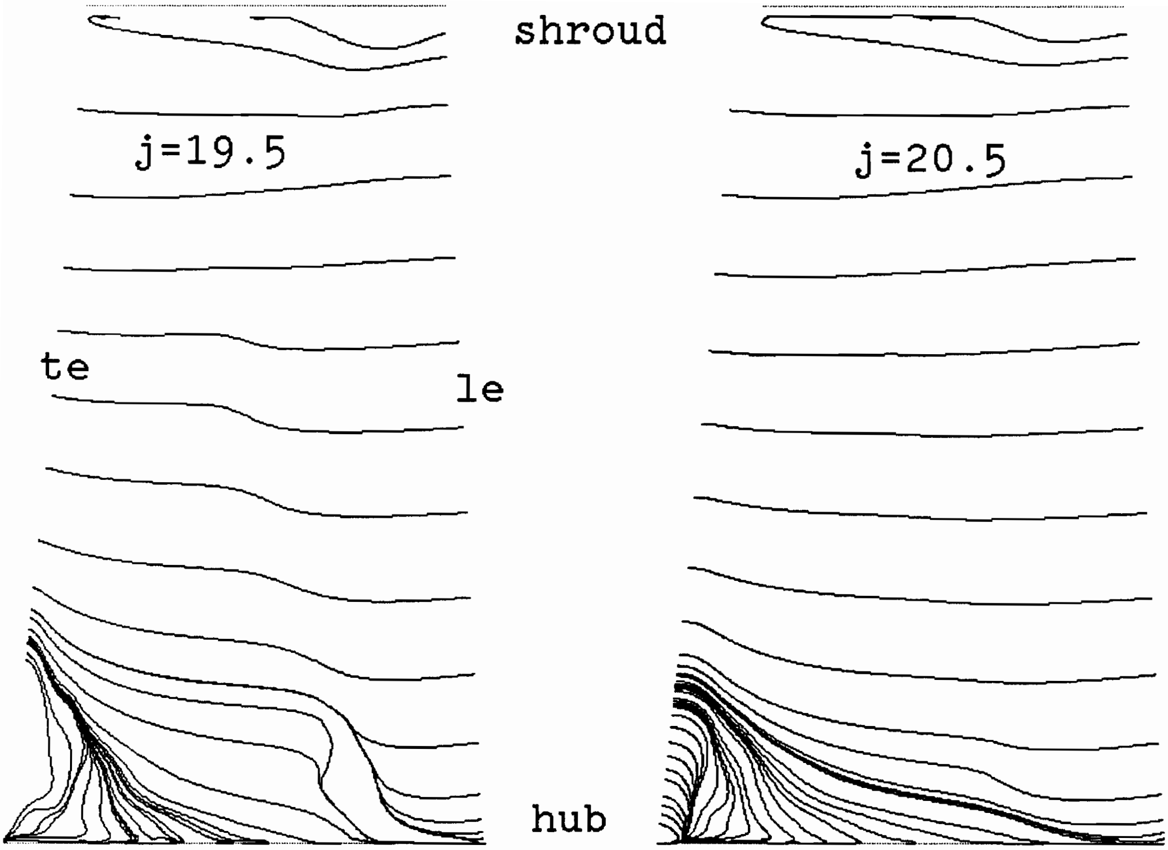

Figure 7.17 Limiting Streaklines on Grid Plane j=19.5 and Limited Streaklines on Plane j=20.5 from MEFP q-L Calculation

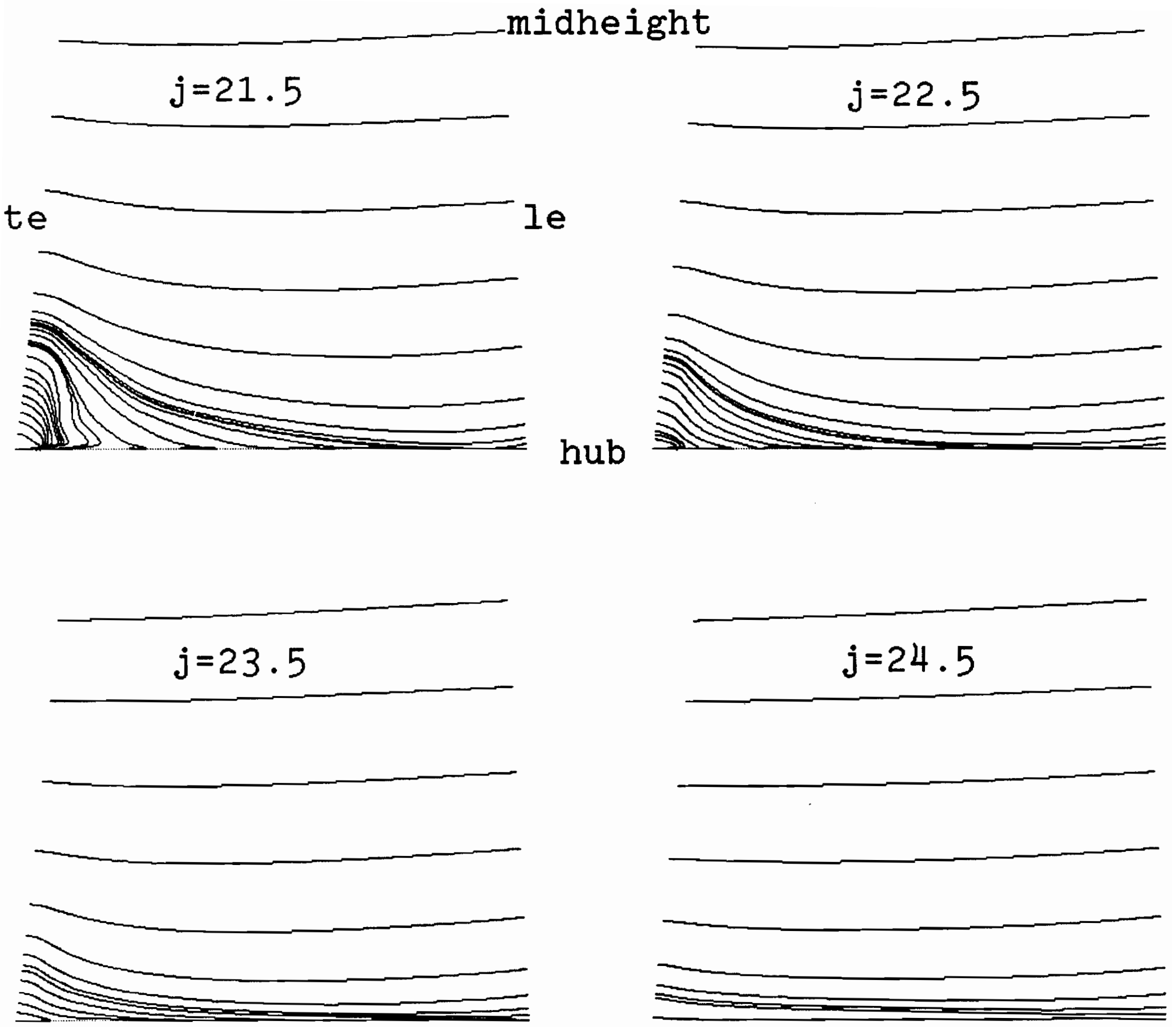

Figure 7.18 Limited Streaklines on Planes j=21.5, 22.5, 23.5, and 24.5 from MEFP q-L Calculation

Streaklines were also plotted on six consecutive planes away from the hub starting at the k=1.5 which is half way between the hub and the near-hub grid points. This gives a grid coordinate of k=1.5 with the remaining planes at: k=2.5, 3.5, 4.5, 5.5, and 6.5. The k=1.5 plane is 0.03% of blade span from the hub and the plane k=6.5 is 3.1% away.

Figure 7.19 shows the limiting streaklines on plane k=1.5 and the limited streaklines on planes k=2.5 and 3.5. The streaklines on plane k=1.5 show several flow phenomena. Starting at the leading edge, the horseshoe vortex is clearly seen. The flow approaching the leading edge breaks apart forming the saddle point and two separation lines characteristic of horseshoe vortices. Just beyond the saddle point, the suction side and pressure side legs of the vortex can be seen flowing back upstream before turning and heading downstream. The suction side leg flows around the leading edge and ends up at the suction surface at approximately 50% of chord. The pressure side leg continues downstream but does not join the corner stall fluid.

The hub secondary flows are shown by the general tendency of the streaklines to move toward the suction surface from the pressure surface. Several of these streaklines are then pulled into the corner stall region and move back upstream. Another phenomenon shown on plane k=1.5 is the streakline coming off the pressure side near the trailing edge. It moves around the trailing edge where it is then entrained in the region of backflow. The final characteristic of the streaklines on plane k=1.5 is the large skew present upstream and downstream of the blade. This skew is where the hub is not rotating.

Plane k=2.5 shows the same characteristics seen on plane k=1.5 but to a smaller degree. The large amounts of skew have nearly disappeared with the downstream flow being affected more. The horseshoe vortex is still shown but is not as well formed, particularly on the pressure side. The secondary flows from the pressure side to the suction side of the passage are not as strong as they were. The streaklines still clearly show the region of backflow and the fluid from the pressure surface being pulled into the corner stall. In plane k=3.5 the horseshoe vortex is no longer present and the secondary flows have decreased in strength again. The amount of fluid being pulled into the corner stall has also decreased. Note that the transition from rotating hub to nonrotating still affects fluid moving downstream of the blade. This may suggest that this region has a significant effect on the corner stall.

Figure 7.20 shows the remaining three k planes. Plane k=4.5 shows that the hub secondary flows have nearly disappeared with the region of backflow being very small now. The effects of the nonrotating hub have also disappeared on this plane. Plane 5.5 shows that the hub secondary flows have disappeared and that the region of backflow has all but disappeared as well. Plane k=6.5 shows that all hub secondary flow has disappeared and the effect of the corner stall is just a thickening of the suction surface boundary layer.

The final streakline plot is shown in Figure 7.21. This is a three-dimensional streakline plot showing the flow in the corner stall region with an i-k plane and an i-j plane. The fluid in the corner stall comes from the hub boundary layer. The streaklines show clearly the development of the hub secondary flow as evidenced by the streaklines curvature. Some of the streaklines show the backflow within the stall and others show the radial secondary flow. There is one streakline from the horseshoe vortex shown. It shows the suction side leg of the vortex being convected over the corner stall.

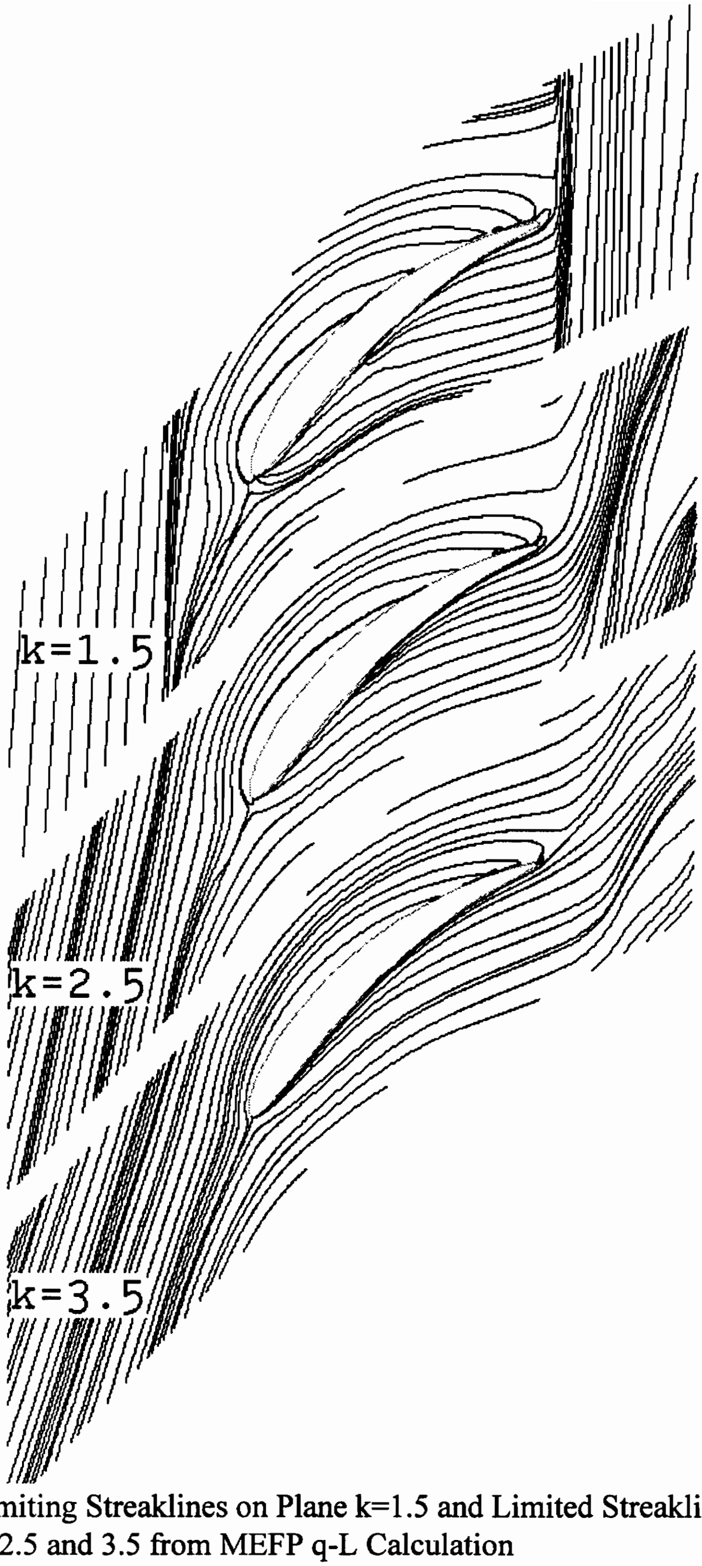

Figure 7.19 Limiting Streaklines on Plane k=1.5 and Limited Streaklines on Planes k=2.5 and 3.5 from MEFP q-L Calculation

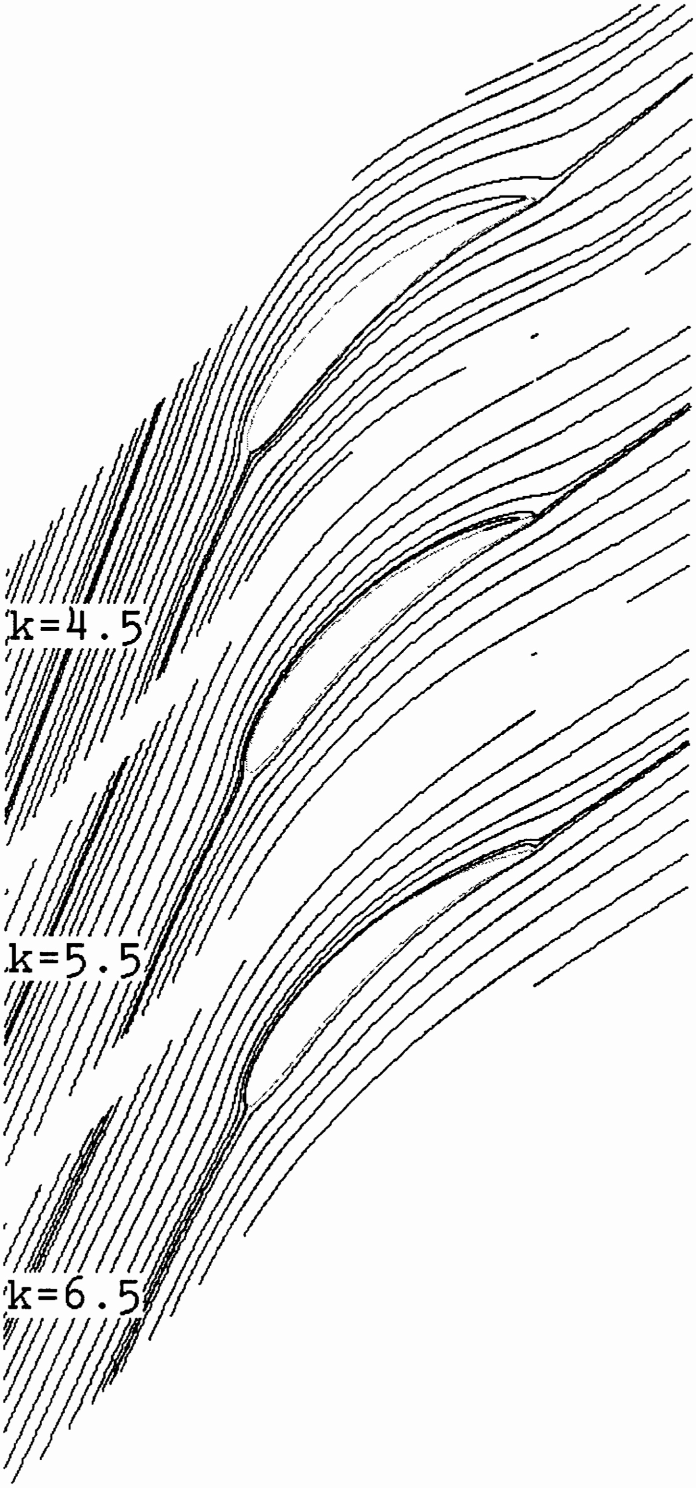

Figure 7.20 Limited Streaklines on Planes k=4.5, 5.5, and 6.5 from MEFP q-L Calculation

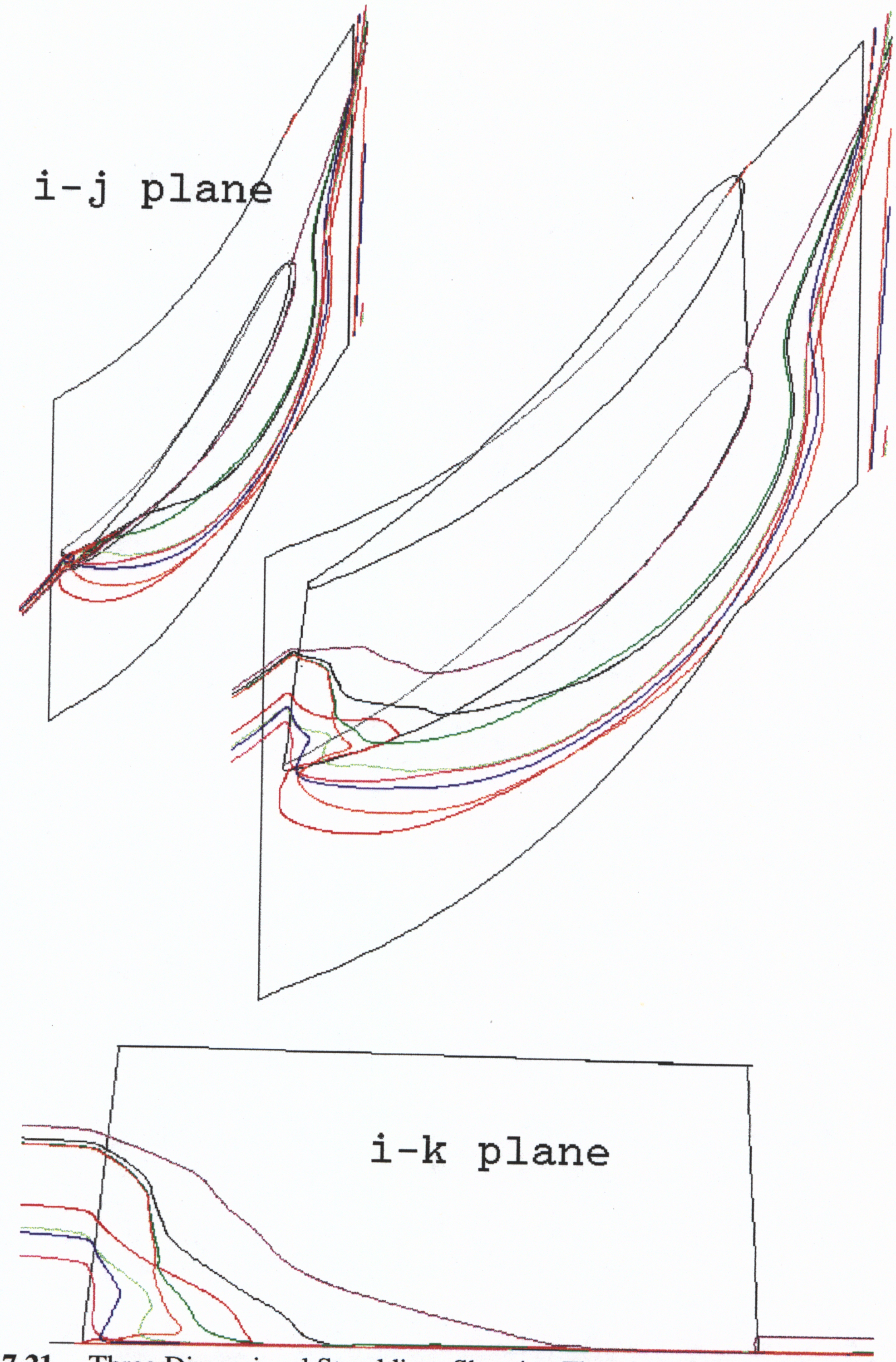

Figure 7.21 Three Dimensional Streaklines Showing Flow in the Corner Stall Region from MEFP q-L Calculation

7.6 q-ω Turbulence Model Preliminary Calculation Results

A second 3-D calculation of the flow through the Deverson rotor was run using a 2-equation q-ω turbulence model currently under development. The model is based upon a model by T. J. Coakley(1985). The relevant equations can be found in Appendix B. The inlet conditions were essentially the same as for the q-L calculation. However, instead of setting L_{fre}, the specific dissipation rate of turbulence kinetic energy, ω, was set. The results of this calculation are very encouraging.

Figure 7.22 shows the axial velocity contours, $V_z/U_{midheight}$, at Plane G. The axial velocity contours are significantly different from the q-L calculation contours seen in Figure 7.6 and the Rolls-Royce mixing length calculation contours seen in Figure 2.17; the q-ω contours are much closer to the measured contours shown in Figure 2.12. In particular, there is agreement between the q-ω calculated and the measured blade wake characteristics that is lacking in the q-L calculation. There is a strong velocity gradient on either side of the wake and the 0.4 contour remains open over the entire span of the blade. A second significant improvement is the presence of radial migration of the loss core away from the hub with flow undercutting the core. This may suggest the existence of stronger secondary flows along the hub. However, the corner stall does not bulge out into the flow, resulting in the corner stall being about half the width it should be.

Figure 7.23 shows the circumferentially averaged axial velocity profile, $V_z/U_{midheight}$. The hub boundary layer is still too thin in this calculation and overall agreement with the actual profile is still poor. However, there appears to be the beginning of a local minimum forming at approximately 7% of span that is similar to the actual velocity profile. That the possible local minimum velocity is nearer the hub than the actual one is due to not enough radial migration of the core. The fact that the velocity above this then increases unlike the actual, is due the narrowness of the loss core. If the corner stall was wider, it would reduce the averaged velocity in that region of the blade span.

Figure 7.24 shows the wake velocity profiles at 23 and 50% of span. Overall, some parts of the rotor wake velocities are in much better agreement with the measured rotor wake velocities and others are worse than what was seen in the q-L calculation. Figure 7.24a shows the rotor wake velocities at 23% span. The wake width has increased slightly to 25% of pitch from 23% for the q-L calculation, but is still less than the measured 36%. This is attributable to the narrowness of the corner stall. The free stream axial velocity at 23% span is correct but the axial velocity in the wake decreases significantly too much, becoming negative. The free stream tangential velocity is slightly high but has the correct behavior as it approaches the pressure side of the wake. However, the tangential velocity approaches the free stream value too slowly as it leaves the suction side of the wake. The free stream radial velocity has the correct behavior on the suction side of the passage but incorrectly becomes slightly positive as it approaches the pressure side of the wake. The radial velocity within the wake peaks very close to the actual value. The free stream relative velocity is slightly under predicted with the relative velocity within the wake being much too small due to the incorrect axial and tangential velocities.

The similarities and differences between the rotor wake velocities at 50% span to the actual wake velocities are comparable to those seen at 23%. The width has increased to 16% of pitch from 13% for the q-L calculation, but is still smaller than the measured 23%. This indicates that the blade surface boundary layers are still too thin. The axial, tangential, and relative velocities within the wake are again over predicted, under predicted, and under predicted, respectively. The free stream axial and tangential velocities are slightly over predicted with the relative velocity again being under predicted. The radial velocity is in good overall agreement with the actual radial velocity except for it not becoming negative enough as it approaches the pressure side of the wake and strange spike downward in the middle of the wake.

The final figure is Figure 7.25 which shows the deviation angles for the calculation. It can be seen by the deviation angles between 5 and 10% span that the size of the separated region is slightly larger than that predicted by the q-L calculation shown in Figure 7.9. Here the deviation reaches 14 degrees compared with only 12 degrees in the q-L calculation. In addition, the deviation angles remain higher as one goes up the blade crossing the data line at 50% instead of 80% span. It can also be seen by the location of the local maximum between 5 and 10% span that although radial migration of the loss core is present as seen in the axial velocity contours in Figure 7.22, it was not strong enough.

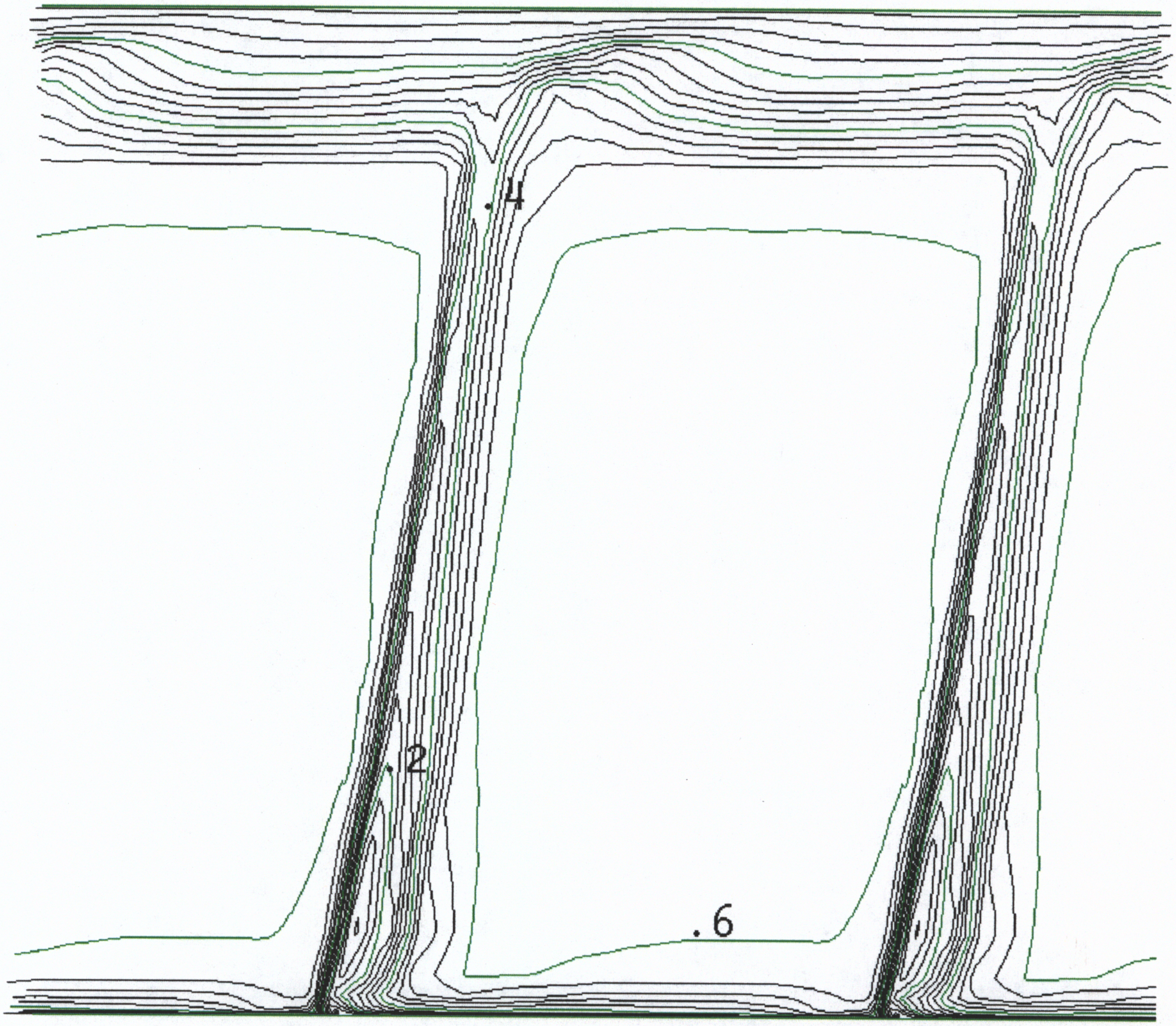

Figure 7.22 Axial Velocity Contours, $V_z/U_{mideight}$, at Plane G for MEFP q-ω Calculation

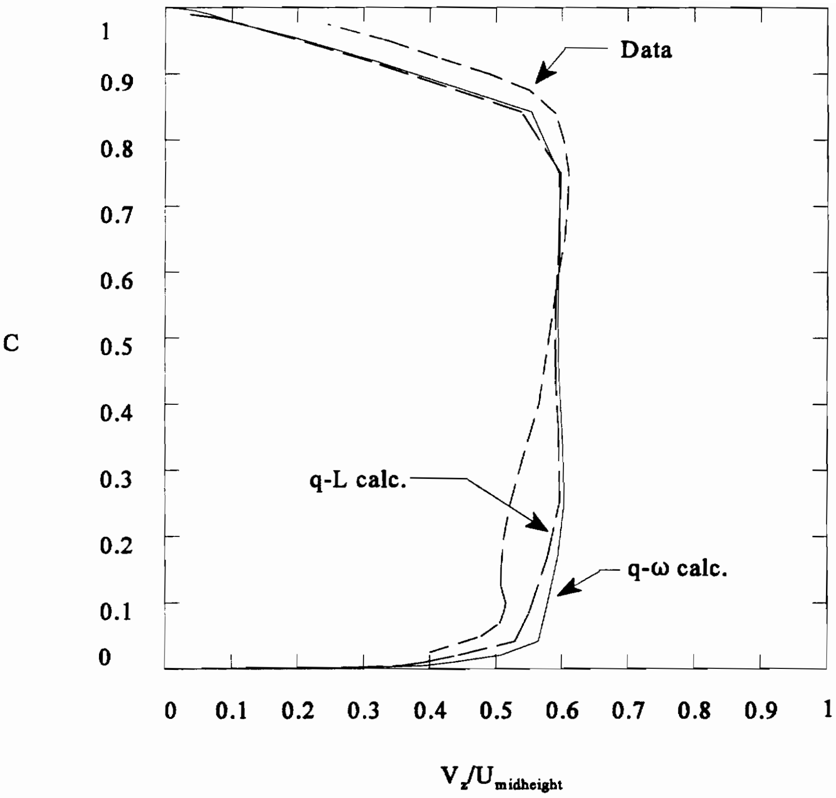

Figure 7.23 Circumferentially Averaged Axial Velocity Profile at Plane G for MEFP q-ω Calculation

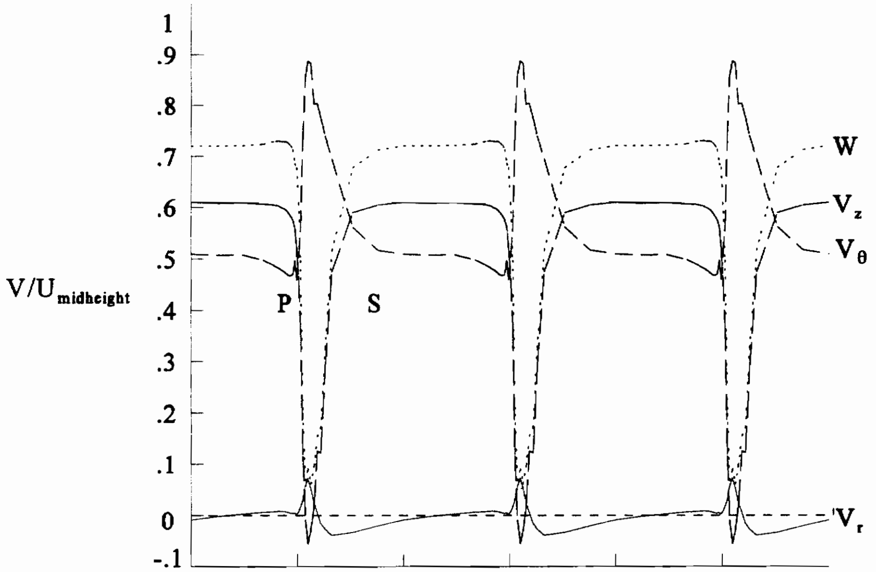

Figure 7.23a Rotor Wake Velocities at 23% Span

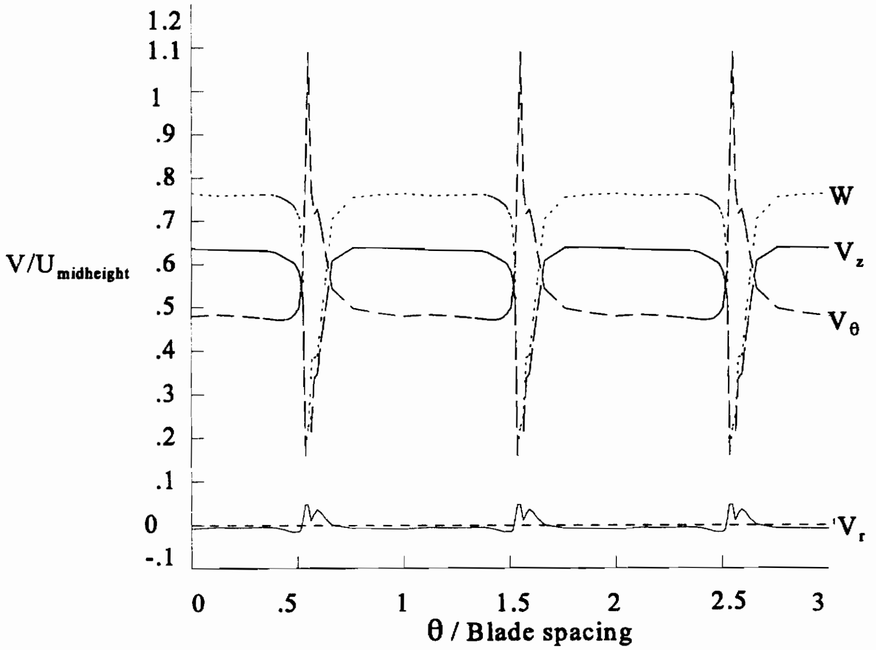

Figure 7.23b Rotor Wake Velocities at 50% Span

Figure 7.24 Wake Velocity Profiles at 23 and 50% at Plane G for q-ω MEFP Calculation

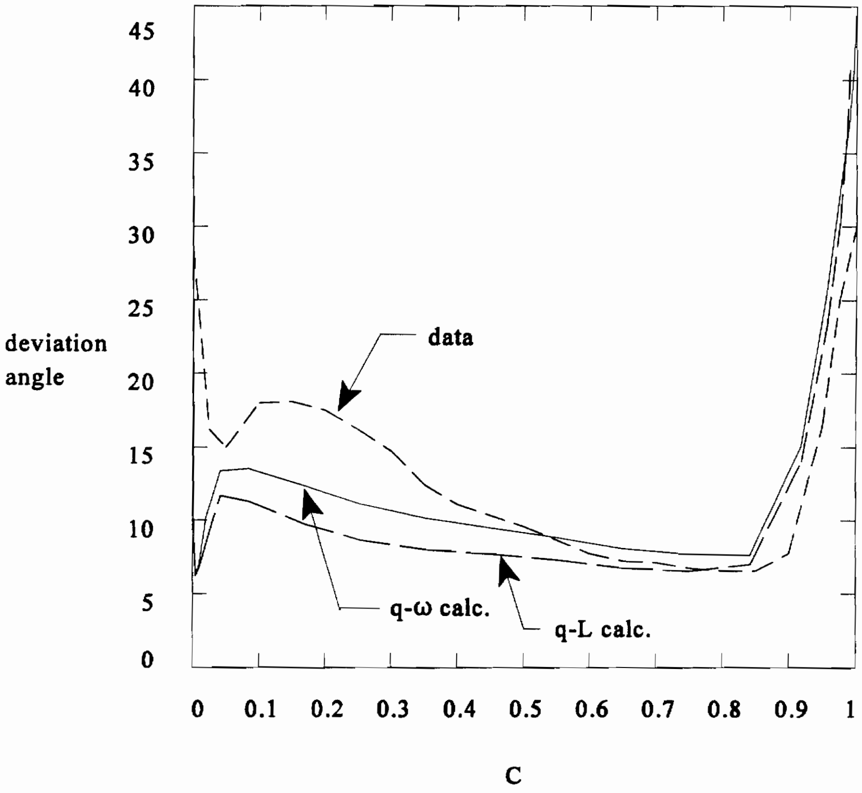

Figure 7.25 Deviation Angles at Plane G for q-ω MEFP Calculation

8.0 Conclusions

The Moore Elliptic Flow Program was used for 2-D cascade studies and 3-D flow calculations through a compressor rotor. The first 2-D calculation was done to validate the q-L transitional turbulence model by comparing the results with experimental data from a NACA study. The other 2-D calculations were cascade studies on the effects of free stream turbulence intensity and incidence angle on suction surface boundary layer development. The 3-D calculations were attempts to predict hub corner stall in the Deverson rotor, a single stage axial compressor, accurately.

8.1 2-D Calculations

8.1.1 NACA Comparison

A zero incidence calculation was made for a NACA cascade of C4 compressor blades with a solidity of one. The calculated skin friction drag coefficient and flow turning angle agreed with the experimental data to within experimental error.

8.1.2 Turbulence Intensity Study

A series of 2-D calculations was performed for the same blading but with a solidity of 1.31 corresponding to the 30 percent radius section of the Deverson rotor. Free stream turbulence intensities ranging from 0.4 to 10 percent were used to enable qualitative comparisons with experimental data from Schlichting and Das. The q-L model predicts the correct trend of transition; the location moves toward the leading edge of the blade as turbulence intensity is increased. Transition was caused by a laminar separation bubble for turbulence intensities less than two percent. The model also correctly predicts the variation of loss over the range of turbulence intensities. However, for the particular geometry considered, the model did not predict a variation in flow turning angle as turbulence intensity is increased, or the presence of a critical turbulence intensity after which transition shifts to the leading edge of the blade.

8.1.3 Incidence Angle Study

A series of 2-D calculations with incidence angles ranging from -15 to 15 degrees was performed for the cascade with a solidity of 1.31. The results were used for a qualitative comparison with the data of Seyb. The model correctly predicts the movement of the transition location toward the leading edge as the incidence angle varies from -15 to 15 degrees. Transition via laminar separation bubble was predicted for incidence angles less than minus nine degrees.

The results show the onset of turbulent separation at an incidence of 6 degrees and the subsequent increase in size of the separated region as incidence is increased. The turbulence model also predicted a variation of loss with incidence angles similarly to that shown by Seyb.

8.2 3-D q-L Calculation

Comparisons of the flow through the axial compressor rotor, predicted using MEFP and a q-L transitional turbulence model, with experimental data have been presented. Additional analyses of the development of the three-dimensional flows and the hub corner stall were also presented. While the model was able to predict corner stall, the size of the stall was under predicted by approximately one half. The model did not predict the radial migration of the loss core in the corner stall seen in the data.

The velocity deficit of the rotor blade wake was severely under predicted. The minimum axial velocity was a factor of two higher than measured. The wake also lacked the radial component of velocity seen in the data. The under prediction of the thickness and velocity deficit of the blade wake may be due to the blade boundary layers being too thin.

The calculation showed hub secondary flows increasing with axial chord and the convection of high loss fluid from the hub boundary layer to the corner stall region.

Radially inward flow along the suction surface is predicted to begin at the leading edge. This is due to radial relief caused by the radial gradient of static pressures. This radial inward flow appears to hinder the development of the radial outflows associated with the corner stall. Radially outward secondary flows on the suction surface began to develop at twenty percent of axial chord. These secondary flows continued to increase in magnitude but did not become strong enough or occupy a large enough area of the blade to give the expected radial migration of the corner stall.

The q-L turbulence model predicts laminar/transitional flow in the corner stall region. This may be unrealistic.

8.3 Preliminary 3-D q-ω Calculaiton

Comparisons of the results of a preliminary 3-D calculation using a two-equation q-ω turbulence model with the experimental evidence and the q-L model calculation were also presented. The q-ω turbulence model is able to predict the blade wake and corner stall more accurately. The model predicts the radial migration of the loss core and correspondingly the radially outward velocity found within the rotor blade wake agrees well with the data. However, it still underpredicts the pitchwise extent of the stall.

The q-ω model predicts backflow on the hub through the region where hub rotation ends. The exit measurement plane is downstream of where the hub stops rotating. If there is a cavity in the hub here, it may significantly modify the flow. This may be the cause of the larger radial migration seen in the axial velocity profile and deviation angle data compared with this model.

8.4 Influences on Hub Corner Stall in Axial flow Compressors

This study suggests that there are many influences on the formation and details of hub corner stall. These include:

1. The suction surface boundary layer growth including transition and separation.
2. Hub endwall secondary flows and the resulting convection of high loss fluid from the hub boundary layer to the corner stall region.
3. The suction surface secondary flows, especially radial relief which is a damping influence on corner stall development.
4. The hub endwall rotor/stator gap flows.
5. The convection of fluid around the trailing edge from the pressure surface boundary layer.

The actual process in a multistage compressor probably involves all of these mechanisms.

8.5 Suggestions for Further Work

The q-ω turbulence model looks very promising for predicting three-dimensional flows through compressors. Validation studies of this new turbulence model are necessary to understand this model better.

The effects of the downstream hub endwall rotor/stator interface and gap on the 3-D flow should also be investigated.

References

Coakley, T. J., 1983, “Turbulence Modeling Methods for the Compressible Navier-Stokes Equations”, Presented @ AIAA 16th Fluid and Plasma Dynamics Conference, July 12-14

Cyrus, Vaclav, 1986, “Experimental Study of Three-Dimensional Flow in an Axial Compressor Stage”, ASME paper no. 86-GT-118

Dong, Y., Gallimore, S. J., and Hodson, H. P., 1986, “Three-Dimensional Flows and Loss Reduction in Axial Compressors”, ASME paper no. 86-GT-193

Felix, R., and Emery, J. C., 1959, “A Comparison of Typical National Gas Turbine Establishment and NACA Axial-Flow Compressor Blade Section in Cascade at Low Speed”, National Advisory Committee for Aeronautics Technical Note 3937

Hawthorne, W. R., 1974, “Secondary Vorticity in Stratified Compressible Fluids in Rotating Systems”, C.U.E.D./A-Turbo/TR63

Hirsch, Ch., and Kang, S., 1993, “Three Dimensional Flow Phenomena in Axial Compressors”, Notes, Vrije Universiteit Brussel, Dept. Fluid Mechanics

Howard, M. A., Ivey, P. C., Barton, J. P., and Young, K. F, 1983, “Endwall Effects at Two Tip Clearances in a Multistage Axial Flow Compressor with Controlled Diffusion Blading”, ASME paper no. 93-GT-299

Janikiraman, S. V., 1993, “Fluid Flow and Heat Transfer in Transonic Turbine Cascades”, MS Thesis, Virginia Polytechnic Institute and State University

Lakshminarayana, B., Sitaram, N., and Zhang, J., 1985, “End-Wall and Profile Losses in a Low-Speed Axial Flow Compressor Rotor”, ASME paper no. 85-GT-174

Leylek, J. H., and Wisler, D. C., 1990, “Mixing in Axial-Flow Compressors: Conclusions Drawn from Three-Dimensional Navier-Stokes Analyses and Experiments”, ASME paper no. 90-GT-352

Moore, J. G., and Moore, J., 1990, “Development of a One-Equation(q-L) Transitional Turbulence Model”, Turbomachinery Research Group Report No. JM/90-8, Mechanical Engineering Department,Virginia Polytechnic Institute and State University

Moore, J., 1994a, "3-D Flows in Turbomachinery Blade Rows", Lecture Notes, Virginia Polytechnic Institute and State University, Mechanical Engineering Department

Moore, J. G., 1994b, "The Moore Elliptic Flow Program for Turbomachinery Flow Calculations 1994 User's Guide", Turbomachinery Research Group Report No JM/94-7, Mechanical Engineering Department, Virginia Polytechnic Institute and State University

Moore, R. W., Jr., and Richardson, D. L., "Skewed Boundary Layer Flow Near the End Walls of a Compressor Cascade", Trans. ASME, November 1957, pp. 1789-1800

Place, J. M., and Howard, J. P., 1993, "Simulating the Multi-Stage Environment in the Cambridge Deverson Rig: C4 Stage Performance and Flow Field Measurements", Rolls-Royce Private Report

Rolls-Royce, 1994, "Comparison of 3D Flow Calculations of the C4 Rotor in the Cambridge University Deverson Rig", Rolls-Royce private communication

Schlichting, H., and Das, A., 1970, "On the Influence of Turbulence Level on the Aerodynamic Losses of Axial Turbomachines", Flow Research on Blading, Elsevier Publishing Company, New York, pp. 243-274

Schlichting, H., 1979, Boundary Layer Theory, 7th edition, McGraw Hill, New York

Seyb, N. J., 1972, "The Role of Boundary Layers in Axial Flow Turbomachines and the Prediction of their Effects", AGARDograph AG 164; 241-259

Thwaites, B., 1949, "Approximate Calculation of Laminar Boundary Layer", Aeronautical Quarterly, Vol. I, November, p. 245

Wadia, A. R., and Beacher, B. F., 1989, "Three-Dimensional Relief in Turbomachinery Blading", ASME paper no. 89-GT-151

White, F. M., 1986, Fluid Mechanics, McGraw Hill, New York

Wisler, D. C., 1987, "Advanced Compressor and Fan Systems", Lecture Notes, General Electric Aircraft Engine Business Group

Appendix A: Method for Scaling Velocity Profile

The absolute total pressure profile for ϕ=0.57 shown in Figure 7.1 was used as the basis for determining the inlet velocity profile for the 3-D calculations. The total pressure values between 5 and 95% span were used to determine the velocity profile for ϕ=0.57. The maximum axial velocity, V_{zmax}, is 22.4 m/s. This occurs at the maximum total pressure of 98,341.2 Pa which is at 30% of span as seen in Figure 7.1. The inlet total temperature is 292.6 K.

For the air flow, isentropic relationships can be used to determine the static temperature at 30% span and then the static pressure.

$$T = T_o - \frac{V_z^2}{2C_p} \qquad \textbf{(Eq. A.1)}$$

$$\frac{p}{p_t} = \left(\frac{T}{T_o}\right)^{3.5} \qquad \textbf{(Eq. A.2)}$$

where C_p is 1004.038 J/kgK. Assuming the static pressure profile is uniform, it is then possible to determine the axial velocity for each total pressure point. To verify the flow coefficient for this velocity profile, the area under the profile is integrated according to

$$\phi = \int_{r_{hub}}^{r_{shroud}} \frac{rV_z dr}{\omega r_{midheight}} \qquad \textbf{(Eq. A.3)}$$

Using linear profiles of V_z from 5% and 95% to the wall to complete the profile gave a

Using linear profiles of V_z from 5% and 95% to the wall to complete the profile gave a flow coefficient of 0.57. The resulting velocity profile is shown in Figure A.1

Assuming that the velocity profile is unchanged from a flow coefficient of 0.57 to 0.51, the velocity profile was then scaled down to a flow coefficient of 0.51 by multiplying each velocity point by the ratio of the two flow coefficients.

$$V_{z\,\phi=0.51} = V_{z\,\phi=0.57}\frac{\phi=0.51}{\phi=0.57} \qquad \textbf{(Eq. A.4)}$$

The new velocity profile can also be seen in Figure A.1. Figure A.2 shows the relative flow inlet angles for both flow coefficients.

The missing parts of the final velocity profile from 5% and 95% to the wall are in the turbulent endwall boundary layers. These segments were generated using a MEFP subroutine, BLAYER, based on uniform shear layers in the near-wall regions.

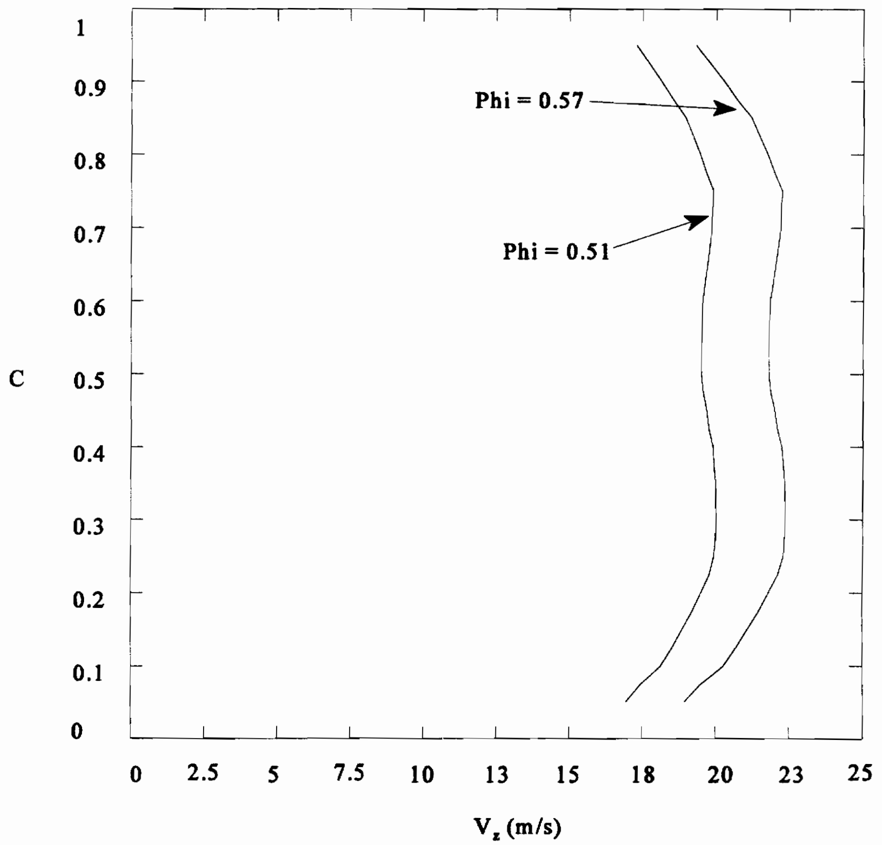

Figure A.1 Velocity Profiles

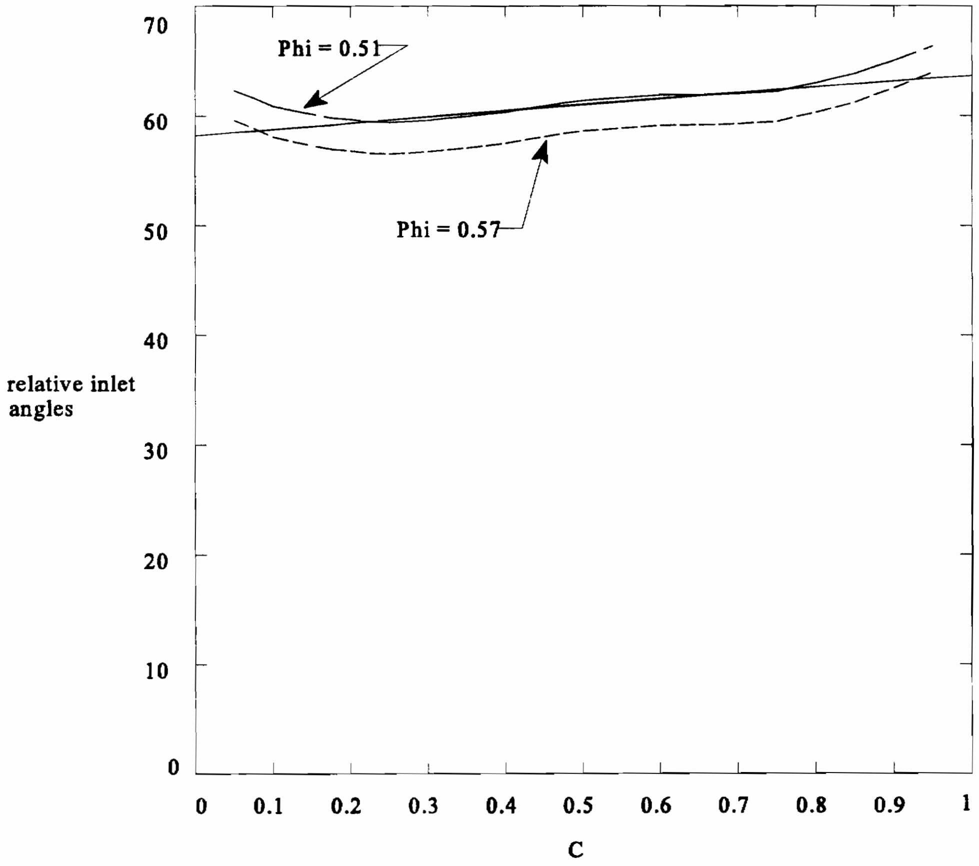

Figure A.2 Relative Inlet Angles

Appendix B: q-ω Turbulence Model

The two equation turbulence model under development in conjunction with this study is based on T. J. Coakley's q-ω model presented in 1983. The turbulence kinetic energy, q, is defined as in equation 3.13 and the specific dissipation rate of kinetic energy is defined as

$$\omega = \frac{\epsilon}{k} \qquad \textbf{(Eq. B.1)}$$

The turbulent viscosity is given by

$$\mu_T = C_\mu \rho F_{vd} \frac{q^2}{\omega} \qquad \textbf{(Eq. B.2)}$$

The differential equation governing q is

$$\rho u \cdot \nabla q - \nabla \cdot \left(\mu_l + \frac{\mu_t}{Pr_q} \right) q = P_q - D_q \qquad \textbf{(Eq. B.3)}$$

where the production term is

$$P_q = \frac{1}{2} C_\mu F_{vd} \frac{\rho q}{\omega} \left(\frac{\text{"du"}}{dy} \right)^2 = \frac{1}{2} \frac{\mu_t}{q} \left(\frac{\text{"du"}}{dy} \right)^2 \qquad \textbf{(Eq. B.4)}$$

and the dissipation term is

$$D_q = \frac{1}{2}\rho\omega q$$

The governing differential equation for ω is

$$\rho u \cdot \nabla\omega - \nabla\cdot\left(\mu_l + \frac{\mu_t}{Pr_\omega}\right)\omega = P_\omega - D_\omega \qquad \textbf{(Eq. B.6)}$$

where the production term is

$$P_\omega = C_\mu\left(C_{10} + C_{11}F_{vd}\right)\rho\left(\frac{"du"}{dy}\right)^2 \qquad \textbf{(Eq. B.7)}$$

and the dissipation term is

$$D_\omega = C_2\rho\omega^2 \quad . \qquad \textbf{(Eq. B.8)}$$

The "van Driest" term is

$$F_{vd} = \left(1 - e^{\left(\frac{-\alpha q \rho y}{\mu}\right)}\right) \quad . \qquad \textbf{(Eq. B.9)}$$

The constants are $Pr_q = Pr_\omega = 2.0$, $C_\mu = 0.09$, $C_{10} = 0.55$, $C_{11} = 0.555$, $C_2 = .833$, and $\alpha = 0.02$.

Vita

John A. Gailliot was born on April, 3 1969 in Alexandria, Virginia. He did his undergraduate work at Virginia Tech. After completion of his B.S. in Mechanical Engineering in May of 1993, he enrolled in the Mechanical Engineering Graduate Program at Virginia Tech. Upon completion of his graduate studies, he plans to work in industry.

His wife, Angelique, and he have a beautiful daughter, Taylor.

John a Gailliot